

1

AFIT/GE/ENG/91D-09

DTIC  
ELECTE  
DEC 27 1991  
S C D

**AD-A243 691**



**A RIGOROUS UTD ANALYSIS OF  
ELECTROMAGNETIC SCATTERING  
FROM RESISTIVE STRIPS AND  
RESISTIVE-LOADED CONDUCTING STRIPS**

**THESIS**

**Douglas H. Casanova, Captain, USAF**

**AFIT/GE/ENG/91D-09**

**UNCLASSIFIED**

**Approved for public release;  
Distribution Unlimited**

**91-18989**



**91 12 24 03 0**

December 1991

Master's Thesis

A Rigorous UTD Analysis of Electromagnetic  
Scattering from Resistive Strips and  
Resistive-Loaded Conducting Strips

Douglas H. Casanova, Captain, USAF

Air Force Institute of Technology, WPAFB OH 45433-6583

AFIT/GE/ENG/91D-09

Approved for public release; distribution unlimited

*method of moments*

→ This thesis investigates electromagnetic scattering from resistive strips and resistive-loaded conducting strips using a rigorous UTD formulation. The UTD diffraction coefficients are based on the Wiener-Hopf technique and Jones' method. Scattering predictions are performed for constant resistive strips, constant resistive-loaded conducting strips, tapered resistive strips, and tapered resistive-loaded conducting strips. All strip geometries have a total width of 4 lambda. Predictions are compared to ~~MM~~ and measurements to determine the validity of the UTD prediction. Overall, there is good agreement. For TMz polarization the only deviations that occur with MM are near edge-on when the degree of the taper increases. For TEz polarization deviations with MM occur near edge-on for all strip geometries except constant resistive strips. Comparisons with measurement are better for TMz except for constant resistive strips. Limitations are explored for tapered resistive strips and tapered resistive-loaded conducting strips based on edge-on scattering levels for TMz polarization. From these limitations scattering characteristics of resistive-loaded conducting strips are explored. ←

Electromagnetic Scattering, Uniform Theory of Diffraction (UTD),  
Strip Scattering, Impedance Loading, Ray Methods

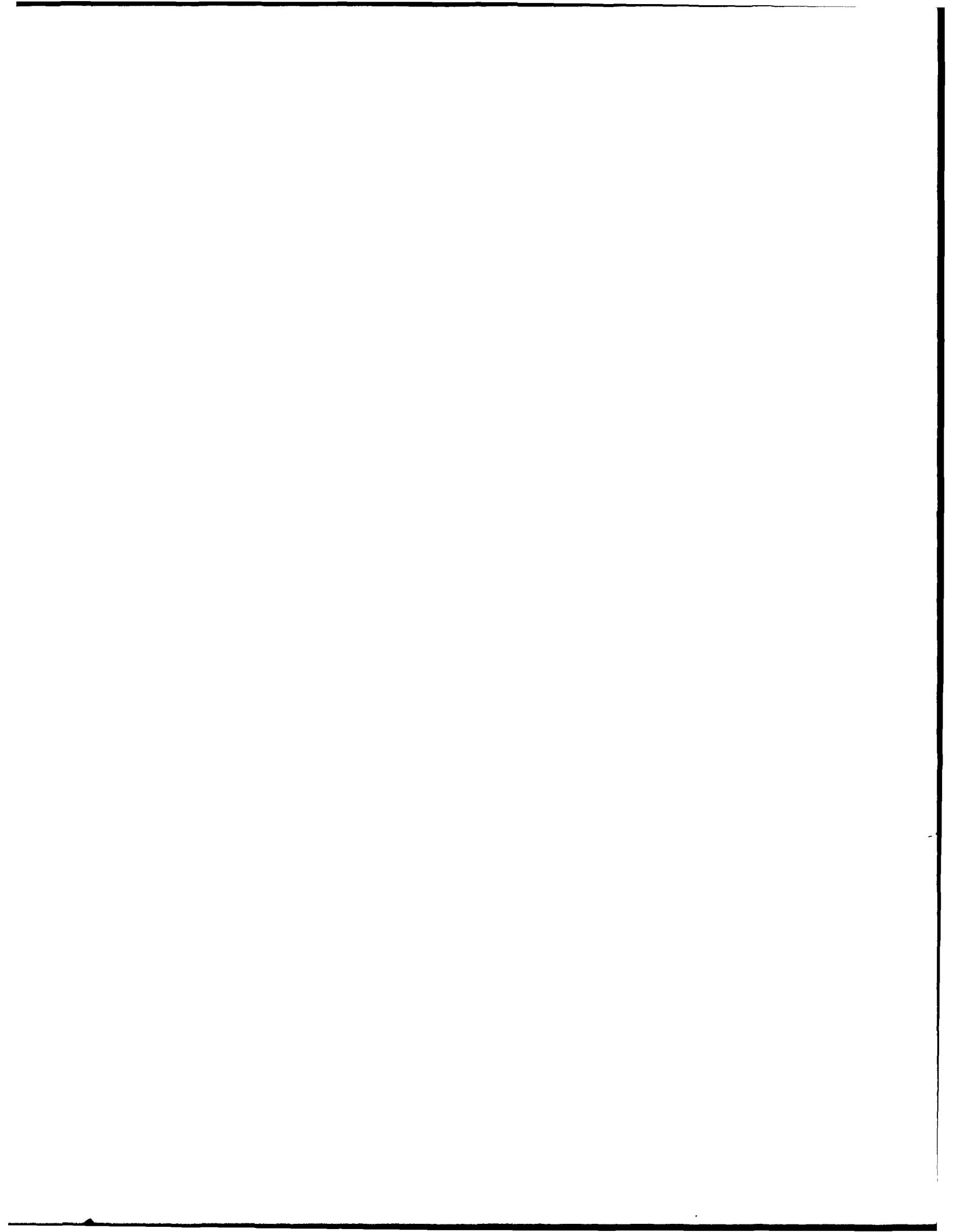
105

Unclassified

Unclassified

Unclassified

UL



A RIGOROUS UTD ANALYSIS OF ELECTROMAGNETIC SCATTERING  
FROM RESISTIVE STRIPS AND RESISTIVE-LOADED  
CONDUCTING STRIPS

THESIS

Presented to the Faculty of the School of Engineering  
of the Air Force Institute of Technology

Air University

In Partial Fulfillment of the  
Requirement for the Degree of  
Master of Science in Electrical Engineering

Douglas H. Casanova, B.S.  
Captain, USAF

December 1991

Accession No.	
DTIC Number	
Distribution	
Availability	
Justification	
By	
Distribution	
Availability	
Availability	
Dist	Special
A-1	



Approved for public release; distribution unlimited

### Acknowledgements

I would like to acknowledge and thank my advisor, Captain Philip Joseph, for his support and direction during this thesis effort. Without his expert technical assistance this thesis would have been a much more trying endeavor. Also, thanks to my thesis committee, Captain Byron Welsh and Dr Vittal Pyati, for their comments and support.

Dr Roberto Rojas and Mike Otero of Ohio State University graciously provided the computer code that I modified for this thesis. They made themselves available for my many questions and requests for help. My heartfelt thanks.

I would like to thank Captain Dan Mullinix and Mr Bob Lindsay for their assistance in RCS and waveguide measurements. Also, thanks to Emerson and Cuming for providing the constant resistive material and Sheldahl for providing the resistive taper.

Finally, I would like to thank my wife, Tina, and son, Joe. Without their patience, support, and understanding this thesis would not have been possible.

## Table of Contents

	Page
Acknowledgements .....	ii
List of Figures .....	v
List of Tables.....	x
Abstract .....	xi
 I. Introduction.....	 1.1
Background .....	1.1
Radar Cross Section .....	1.1
RCS Reduction.....	1.2
Resistive-Loaded Conducting Strips.....	1.3
Prediction Models .....	1.3
Previous Research .....	1.4
Problem Statement .....	1.5
Approach .....	1.5
 II. Theory .....	 2.1
Scattering from the Junction of Dissimilar Dielectric Half-Plane Slabs.....	2.1
Generalized Impedance Boundary Conditions.....	2.2
Wiener-Hopf Technique.....	2.3
Scattering from the Junction of Resistive Half-Planes.....	2.6
Multiple Diffractions.....	2.10
 III. Resistive Strips and Resistive-Loaded Conducting Strips.....	 3.1
Geometry .....	3.1
Application of Theory .....	3.3
Verification.....	3.5
MM Comparison .....	3.5
Constant Resistive Strips.....	3.6
Constant Resistive-Loaded Conducting Strips.....	3.12
Tapered Resistive Strips.....	3.15
Tapered Resistive-Loaded Conducting Strips.....	3.19
Measurements.....	3.24
Resistive Materials .....	3.24
Target Preparation .....	3.26
Constant Resistive Strips.....	3.33
Constant Resistive-Loaded Conducting Strips.....	3.39
Tapered Resistive Strips.....	3.42

Tapered Resistive-Loaded Conducting Strips.....	3.45
Limitations .....	3.48
Tapered Resistive Strip Edge-On Scattering.....	3.49
Tapered Resistive-Loaded Conducting Strip Edge-On Scattering .....	3.51
IV. Scattering Characteristics of Resistive-Loaded Conducting Strips .....	4.1
Constant Resistive-Loaded Conducting Strips.....	4.1
Tapered Resistive-Loaded Conducting Strips, $\text{Eta} = a( x  - 1)^b$ .....	4.3
Constant b, Varying a.....	4.4
Constant a, Varying b.....	4.9
Tradeoffs .....	4.13
V. Conclusions.....	5.1
Summary and Findings.....	5.1
Recommendations .....	5.3
Bibliography.....	Bib.1

## List of Figures

Figure	Page
2.1. Two-Part Dielectric/Ferrite Plane Geometry .....	2.2
2.2. Three-Part Resistive Plane Geometry .....	2.10
2.3. Four-Part Resistive Plane Geometry .....	2.13
3.1. Strip Geometry .....	3.1
3.2. Normalized Resistances of Different Strip Geometries .....	3.2
3.3. Scattering Prediction for a PEC Half-Plane and Loaded PEC Half-Plane, 0.354 $\lambda$ Loads, $R_1 = 121\Omega$ , $R_2 = 624\Omega$ , $TM_z$ , Multiple Diffractions .....	3.4
3.4. Scattering Prediction for a $2\lambda$ Conducting Strip with $1\lambda$ Constant Resistive Loads, $\eta = 2$ , $TM_z$ , Multiple Diffractions.....	3.4
3.5. Resistive Taper, $\eta = x^2$ , Modeled With Discrete Resistive Strips, Ten Segments Per Wavelength .....	3.5
3.6. Scattering Prediction for a $4\lambda$ Conducting Strip, $TM_z$ .....	3.7
3.7. Scattering Prediction for a $4\lambda$ Conducting Strip, $TE_z$ .....	3.7
3.8. Scattering Prediction for a $4\lambda$ Constant Resistive Strip, $\eta = 0.5$ , $TM_z$ .....	3.8
3.9. Scattering Prediction for a $4\lambda$ Constant Resistive Strip, $\eta = 1$ , $TM_z$ .....	3.8
3.10. Scattering Prediction for a $4\lambda$ Constant Resistive Strip, $\eta = 3$ , $TM_z$ .....	3.9
3.11. Scattering Prediction for a $4\lambda$ Constant Resistive Strip, $\eta = 4$ , $TM_z$ .....	3.9
3.12. Scattering Prediction for a $4\lambda$ Constant Resistive Strip, $\eta = 1$ , $TE_z$ .....	3.10
3.13. Scattering Prediction for a $4\lambda$ Constant Resistive Strip, $\eta = 3$ , $TE_z$ .....	3.10
3.14. Scattering Prediction for a $2\lambda$ Conducting Strip with $1\lambda$ Constant Resistive Loads, $\eta = 0.5$ , $TM_z$ .....	3.12
3.15. Scattering Prediction for a $2\lambda$ Conducting Strip with $1\lambda$ Constant Resistive Loads, $\eta = 1.5$ , $TM_z$ .....	3.13
3.16. Scattering Prediction for a $2\lambda$ Conducting Strip with $1\lambda$ Constant Resistive Loads, $\eta = 2$ , $TM_z$ .....	3.13
3.17. Scattering Prediction for a $2\lambda$ Conducting Strip with $1\lambda$ Constant Resistive Loads, $\eta = 4$ , $TM_z$ .....	3.14



3.18. Scattering Prediction for a $2\lambda$ Conducting Strip with $1\lambda$ Constant Resistive Loads, $\eta = 0.5$ , $TE_z$ .....	3.14
3.19. Scattering Prediction for a $2\lambda$ Conducting Strip with $1\lambda$ Constant Resistive Loads, $\eta = 2$ , $TE_z$ .....	3.15
3.20. Scattering Prediction for a $4\lambda$ Tapered Resistive Strip, $\eta =  x $ , $TM_z$ .....	3.16
3.21. Scattering Prediction for a $4\lambda$ Tapered Resistive Strip, $\eta = x^2$ , $TM_z$ .....	3.16
3.22. Scattering Prediction for a $4\lambda$ Tapered Resistive Strip, $\eta =  x ^3$ , $TM_z$ .....	3.17
3.23. Scattering Prediction for a $4\lambda$ Tapered Resistive Strip, $\eta = x^4$ , $TM_z$ .....	3.17
3.24. Scattering Prediction for a $4\lambda$ Tapered Resistive Strip, $\eta = x^2$ , $TE_z$ .....	3.18
3.25. Scattering Prediction for a $4\lambda$ Tapered Resistive Strip, $\eta = x^4$ , $TE_z$ .....	3.18
3.26. Scattering Prediction for a $2\lambda$ Conducting Strip with $1\lambda$ Tapered Resistive Loads, $\eta =  x  - 1$ , $TM_z$ .....	3.20
3.27. Scattering Prediction for a $2\lambda$ Conducting Strip with $1\lambda$ Tapered Resistive Loads, $\eta = ( x  - 1)^2$ , $TM_z$ .....	3.20
3.28. Scattering Prediction for a $2\lambda$ Conducting Strip with $1\lambda$ Tapered Resistive Loads, $\eta = ( x  - 1)^3$ , $TM_z$ .....	3.21
3.29. Scattering Prediction for a $2\lambda$ Conducting Strip with $1\lambda$ Tapered Resistive Loads, $\eta = ( x  - 1)^4$ , $TM_z$ .....	3.21
3.30. Scattering Prediction for a $2\lambda$ Conducting Strip with $1\lambda$ Tapered Resistive Loads, $\eta = ( x  - 1)^2$ , $TE_z$ .....	3.22
3.31. Scattering Prediction for a $2\lambda$ Conducting Strip with $1\lambda$ Tapered Resistive Loads, $\eta = ( x  - 1)^4$ , $TE_z$ .....	3.22
3.32. Tapered Resistive-Loaded Conducting Strip Comparison, $b = 1, 2, 3, 4$ .....	3.23
3.33. Constant Resistive-Loaded Strip Constructed of SC 100 or VF 10.....	3.27
3.34. Tapered Resistive Strip Constructed with VF 10 and VF 20.....	3.27
3.35. Tapered Resistive Strip Constructed with VF 10, VF 20, and VF 30.....	3.28
3.36. Tapered Resistive-Loaded Conducting Strip Constructed with VF 10 and VF 20 .....	3.28
3.37. Tapered Resistive-Loaded Conducting Strip Constructed with VF 10, VF 20, and VF 30.....	3.29
3.38. Tapered Resistive-Loaded Conducting Strip Constructed with a Sheldahl Taper .....	3.29

3.39. Styrofoam Mount Construction.....	3.30
3.40. Scattering Measurement and Prediction for a $4\lambda$ Conducting Strip, $TM_z$ .....	3.33
3.41. Scattering Measurement and Prediction for a $4\lambda$ Conducting Strip, $TE_z$ .....	3.34
3.42. Scattering Measurement and Prediction for a $4\lambda$ Constant Resistive Strip, SC 100, $TM_z$ .....	3.34
3.43. Scattering Measurement and Prediction for a $4\lambda$ Constant Resistive Strip, SC 100, $TE_z$ .....	3.35
3.44. Scattering Measurement and Prediction for a $4\lambda$ Constant Resistive Strip, VF 10, $TM_z$ .....	3.35
3.45. Scattering Measurement and Prediction for a $4\lambda$ Constant Resistive Strip, VF 10, $TE_z$ .....	3.36
3.46. Scattering Measurement and Prediction for a $4\lambda$ Constant Resistive Strip, VF 20, $TM_z$ .....	3.36
3.47. Scattering Measurement and Prediction for a $4\lambda$ Constant Resistive Strip, VF 20, $TE_z$ .....	3.37
3.48. Scattering Measurement and Prediction for a $4\lambda$ Constant Resistive Strip, VF 30, $TM_z$ .....	3.37
3.49. Scattering Measurement and Prediction for a $4\lambda$ Constant Resistive Strip, VF 30, $TE_z$ .....	3.38
3.50. Scattering Measurement and Prediction for a $2\lambda$ Conducting Strip with $1\lambda$ Constant Resistive Loads, SC 100, $TM_z$ .....	3.40
3.51. Scattering Measurement and Prediction for a $2\lambda$ Conducting Strip with $1\lambda$ Constant Resistive Loads, SC 100, $TE_z$ .....	3.40
3.52. Scattering Measurement and Prediction for a $2\lambda$ Conducting Strip with $1\lambda$ Constant Resistive Loads, VF 10, $TM_z$ .....	3.41
3.53. Scattering Measurement and Prediction for a $2\lambda$ Conducting Strip with $1\lambda$ Constant Resistive Loads, VF 10, $TE_z$ .....	3.41
3.54. Scattering Measurement and Prediction for a $4\lambda$ Tapered Resistive Strip, VF 10 and VF 20, $TM_z$ .....	3.43
3.55. Scattering Measurement and Prediction for a $4\lambda$ Tapered Resistive Strip, VF 10 and VF 20, $TE_z$ .....	3.43
3.56. Scattering Measurement and Prediction for a $4\lambda$ Tapered Resistive Strip, VF 10, VF 20, and VF 30, $TM_z$ .....	3.44

3.57. Scattering Measurement and Prediction for a $4\lambda$ Tapered Resistive Strip, VF 10, VF 20, and VF 30, $TE_z$ .....	3.44
3.58. Scattering Measurement and Prediction for a $2\lambda$ Conducting Strip with $1\lambda$ Tapered Resistive Loads, VF 10 and VF 20, $TM_z$ .....	3.45
3.59. Scattering Measurement and Prediction for a $2\lambda$ Conducting Strip with $1\lambda$ Tapered Resistive Loads, VF 10 and VF 20, $TE_z$ .....	3.46
3.60. Scattering Measurement and Prediction for a $2\lambda$ Conducting Strip with $1\lambda$ Tapered Resistive Loads, VF 10, VF 20, and VF 30, $TM_z$ .....	3.46
3.61. Scattering Measurement and Prediction for a $2\lambda$ Conducting Strip with $1\lambda$ Tapered Resistive Loads, VF 10, VF 20, and VF 30, $TE_z$ .....	3.47
3.62. Scattering Measurement and Prediction for a $2\lambda$ Conducting Strip with $1\lambda$ Tapered Resistive Loads, Sheldahl, $TM_z$ .....	3.47
3.63. Edge-On Scattering Difference Between UTD and MM for an $a x ^b$ Tapered Resistive Strip versus b.....	3.49
3.64. Edge-On Scattering Difference Between UTD and MM for an $a x ^b$ Tapered Resistive Strip versus a.....	3.50
3.65. Scattering Prediction for a $4\lambda$ Tapered Resistive Strip, $\eta =  x ^5$ , $TM_z$ .....	3.50
3.66. Edge-On Scattering Difference Between UTD and MM for an $a( x  - 1)^b$ Tapered Resistive-Loaded Conducting Strip versus b.....	3.51
3.67. Edge-On Scattering Difference Between UTD and MM for an $a( x  - 1)^b$ Tapered Resistive-Loaded Conducting Strip versus a.....	3.52
4.1. Scattering Predictions for $2\lambda$ Conducting Strips with $1\lambda$ Constant Resistive Loads and Conducting Strip Reference, $\eta = 0.5$ and $1.5$ .....	4.2
4.2. Scattering Predictions for $2\lambda$ Conducting Strips with $1\lambda$ Constant Resistive Loads and Conducting Strip Reference, $\eta = 2$ and $4$ .....	4.2
4.3. Scattering Predictions for $2\lambda$ Conducting Strips with $1\lambda$ Constant Resistive Loads and Conducting Strip References, $\eta = 4$ .....	4.3
4.4. Scattering Predictions for $2\lambda$ Conducting Strips with $1\lambda$ Tapered Resistive Loads and Conducting Strip Reference, $\eta = 1/4 ( x  - 1)$ and $1/2 ( x  - 1)$ .....	4.5
4.5. Scattering Predictions for $2\lambda$ Conducting Strips with $1\lambda$ Tapered Resistive Loads and Conducting Strip Reference, $\eta =  x  - 1$ and $2( x  - 1)$ .....	4.5
4.6. Scattering Predictions for $2\lambda$ Conducting Strips with $1\lambda$ Tapered Resistive Loads and Conducting Strip Reference, $\eta = 1/4 ( x  - 1)^2$ and $1/2 ( x  - 1)^2$ .....	4.6
4.7. Scattering Predictions for $2\lambda$ Conducting Strips with $1\lambda$ Tapered Resistive Loads and Conducting Strip Reference, $\eta = ( x  - 1)^2$ and $2( x  - 1)^2$ .....	4.6

4.8. Scattering Predictions for $2\lambda$ Conducting Strips with $1\lambda$ Tapered Resistive Loads and Conducting Strip Reference, $\eta = 1/4 ( x  - 1)^3$ and $1/2 ( x  - 1)^3$ .....	4.7
4.9. Scattering Predictions for $2\lambda$ Conducting Strips with $1\lambda$ Tapered Resistive Loads and Conducting Strip Reference, $\eta = ( x  - 1)^3$ and $2( x  - 1)^3$ .....	4.7
4.10. Scattering Predictions for $2\lambda$ Conducting Strips with $1\lambda$ Tapered Resistive Loads and Conducting Strip Reference, $\eta = 1/4 ( x  - 1)^4$ and $1/2 ( x  - 1)^4$ .....	4.8
4.11. Scattering Predictions for $2\lambda$ Conducting Strips with $1\lambda$ Tapered Resistive Loads and Conducting Strip Reference, $\eta = ( x  - 1)^4$ and $2( x  - 1)^4$ .....	4.8
4.12. Scattering Predictions for $2\lambda$ Conducting Strips with $1\lambda$ Tapered Resistive Loads and Conducting Strip Reference, $\eta = 1/4 ( x  - 1)$ and $1/4 ( x  - 1)^2$ .....	4.9
4.13. Scattering Predictions for $2\lambda$ Conducting Strips with $1\lambda$ Tapered Resistive Loads and Conducting Strip Reference, $\eta = 1/4 ( x  - 1)^3$ and $1/4 ( x  - 1)^4$ .....	4.10
4.14. Scattering Predictions for $2\lambda$ Conducting Strips with $1\lambda$ Tapered Resistive Loads and Conducting Strip Reference, $\eta = 1/2 ( x  - 1)$ and $1/2 ( x  - 1)^2$ .....	4.10
4.15. Scattering Predictions for $2\lambda$ Conducting Strips with $1\lambda$ Tapered Resistive Loads and Conducting Strip Reference, $\eta = 1/2 ( x  - 1)^3$ and $1/2 ( x  - 1)^4$ .....	4.11
4.16. Scattering Predictions for $2\lambda$ Conducting Strips with $1\lambda$ Tapered Resistive Loads and Conducting Strip Reference, $\eta =  x  - 1$ and $( x  - 1)^2$ .....	4.11
4.17. Scattering Predictions for $2\lambda$ Conducting Strips with $1\lambda$ Tapered Resistive Loads and Conducting Strip Reference, $\eta = ( x  - 1)^3$ and $( x  - 1)^4$ .....	4.12
4.18. Scattering Predictions for $2\lambda$ Conducting Strips with $1\lambda$ Tapered Resistive Loads and Conducting Strip Reference, $\eta = 2( x  - 1)$ and $2( x  - 1)^2$ .....	4.12
4.19. Scattering Predictions for $2\lambda$ Conducting Strips with $1\lambda$ Tapered Resistive Loads and Conducting Strip Reference, $\eta = 2( x  - 1)^3$ and $2( x  - 1)^4$ .....	4.13
4.20. Main Lobe Scattering Reduction for $a( x  - 1)^b$ Taper .....	4.16
4.21. Main Lobe Broadening for $a( x  - 1)^b$ Taper .....	4.17
4.22. Edge-On Reduction for $a( x  - 1)^b$ Taper .....	4.17
4.23. Sidelobe Reduction for $a( x  - 1)^b$ Taper, $0^\circ$ - $30^\circ$ .....	4.18
4.24. Sidelobe Reduction for $a( x  - 1)^b$ Taper, $30^\circ$ - $60^\circ$ .....	4.18

### List of Tables

Table	Page
3.1. Material Parameters .....	3.25
3.2. Measurements .....	3.31
4.1. Figures of Merit for Resistive-Loaded Conducting Strips.....	4.14

Abstract

This thesis investigates electromagnetic scattering from resistive strips and resistive-loaded conducting strips using a rigorous UTD formulation. The UTD diffraction coefficients are based on the Wiener-Hopf technique and Jones' method. Scattering predictions are performed for constant resistive strips, constant resistive-loaded conducting strips, tapered resistive strips, and tapered resistive-loaded conducting strips. All strip geometries have a total width of  $4\lambda$ . Predictions are compared to MM and measurements to determine the validity of the UTD prediction. Overall, there is good agreement. For  $TM_z$  polarization the only deviations that occur with MM are near edge-on when the degree of the taper increases. For  $TE_z$  polarization deviations with MM occur near edge-on for all strip geometries except constant resistive strips. Comparisons with measurements are better for  $TM_z$  except for constant resistive strips. Limitations are explored for tapered resistive strips and tapered resistive-loaded conducting strips based on edge-on scattering levels for  $TM_z$  polarization. From these limitations scattering characteristics of resistive-loaded conducting strips are explored for  $TM_z$  polarization. Constant loads decrease the main lobe's scattering level more, but suffer from main lobe broadening. Tapered loads have more significant reductions on sidelobe and edge-on scattering levels.

# A RIGOROUS UTD ANALYSIS OF ELECTROMAGNETIC SCATTERING FROM RESISTIVE STRIPS AND RESISTIVE-LOADED CONDUCTING STRIPS

## I. Introduction

### Background

Radar Cross Section. When an electromagnetic wave transmitted by a radar strikes a complex target, such as an aircraft, energy is scattered in all directions. The energy scattered in a particular direction determines the target's radar cross section (RCS) in that direction. RCS is defined by the formula

$$\sigma = \lim_{R \rightarrow \infty} 4\pi R^2 \left| \frac{E_s}{E_i} \right|^2 \quad (1.1)$$

where  $R$  is the range from the target to the radar,  $E_s$  is the scattered electromagnetic field in a given direction, and  $E_i$  is the incident electromagnetic field at the target. RCS is independent of range since the scattered field varies as  $1/R$  and the incident field's value is taken at the target. RCS is dependent upon the target's electrical size, shape, and materials, as well as the incident electromagnetic wave's frequency and polarization. Typically, the scattered field used in the computation has the same polarization as the incident field even though other polarizations may be scattered. This models a radar receiver/transmitter set-up, i.e., the radar transmits a vertically polarized wave and receives the vertically polarized portion of the scattered wave (VV) or the radar transmits and receives horizontally polarized waves (HH). Sometimes, VH or HV is used in the computation.

RCS Reduction. The goal in RCS reduction is to decrease the amount of energy scattered by the target back to the radar receiver. Consequently, the target's RCS and probability of detection are reduced. There are four ways to help reduce a target's RCS: shaping, radar absorbing materials, passive cancellation (impedance loading), and active cancellation (5:190-192).

Shaping a target to scatter the majority of the incident electromagnetic energy away from the radar receiver will decrease the RCS. Typically, the radar threat is considered to be in the forward sector of the aircraft; thus, shaping will be used to deflect the incident electromagnetic wave to the side and/or back. A disadvantage of shaping is that the aerodynamic performance of the aircraft may be degraded. Careful tradeoffs between mission and probability of radar detection requirements must be considered when using shaping to alter an aircraft's RCS.

Radar absorbing materials (RAM) and radar absorbing structure (RAS) reduce RCS by converting some of the incident electromagnetic wave into heat so that it cannot be scattered back to the radar receiver. Also, RAM and RAS may create multiple echoes of an incident wave that cancel each other. RAM is added to an existing structure while RAS is a structure that has been designed as a radar absorber. A disadvantage of RAM is that it is bulky and may degrade the aerodynamic performance of the aircraft. The tradeoffs mentioned in the shaping technique are applicable.

Passive cancellation or impedance loading decreases RCS by applying an impedance load to a metallic surface or geometry. The application of these loads produces new scattering centers that may destructively interfere with the original scattering pattern. A disadvantage of impedance loading is that it is typically frequency dependent; thus, much effort has been expended in designing impedance loads that are active over a range of frequencies.



Active cancellation is an RCS reduction technique that is much more complicated to implement than any of the previous three. The aircraft must have a receiver/transmitter setup that can sense the characteristics of an incoming electromagnetic wave, as well as know the aircraft scattering characteristics. Then, the receiver/transmitter setup must transmit a wave of proper amplitude and phase (at the correct timing) that cancels with the aircraft's scattered wave. Although the basic characteristics of this technique are known, it is difficult to put into practice with today's technology.

Resistive-Loaded Conducting Strips. Due to the complexity of aircraft structures, simpler geometries must be explored to model the RCS reductions obtained with resistive loading. Two-dimensional strips are a good starting geometry, because the scattering characteristics of conducting strips have been accurately modeled and measured. In addition, besides aircraft structures, this geometry could be extended for applying resistive loading to antennas to create desirable scattering patterns. The two models used in this thesis to predict scattering from resistive-loaded conducting strips are: moment method (MM) and uniform theory of diffraction (UTD).

Prediction Models. MM is actually a term used for a numerical technique used to solve general integral equations. An incident electromagnetic wave induces an unknown current density on the surface of a target. An integral equation is developed where the unknown current density is part of the integrand. MM is used to solve for the unknown current density. Then, the scattered field,  $E_s$ , is determined using a radiation integral (1:670). MM is limited by the fact that it is used primarily for electrically small targets. This is because the surface must be sampled up to ten times per wavelength to obtain accurate predictions. For electrically large targets, this results in very large matrices that increase computer run times significantly (5:57).

UTD is an accurate high frequency ray technique developed by Kouyoumjian and Pathak (6). It combines geometric optics fields with edge diffractions to determine the total

scattered electromagnetic field (1:743). Using asymptotic methods and the exact eigenfunction solutions for a conducting wedge, Kouyoumjian and Pathak developed an accurate high frequency solution for the edge diffractions from perfect electric conductors (PECs). Advantages of UTD are that it is computationally efficient and yields accurate results that compare well with measurements (1:744). A disadvantage is that most research in this area has applied only to metallic bodies. More recently, Rojas (9) has used the Wiener-Hopf technique to extend UTD to impedance materials.

Previous Research. Recent research has showed that resistive loading can significantly reduce the scattering characteristics of conducting strips (2; 3). Haupt and Liepa used MM to model a parabolically tapered resistive load that decreased the edge-on scattering of a conducting strip by 15 dB (2:57). Heaton heuristically modified the UTD diffraction coefficients for the case of resistive edges and junctions. It was discovered that uniform resistive loads decreased sidelobe and edge-on scattering of conducting strips relative to the main broadside lobe. Also, it was found that tapered impedance loads had a more pronounced decrease on the sidelobe and edge-on scattering of conducting strips. However, accurate prediction was limited from  $40^\circ$  to  $60^\circ$  from broadside incidence (3:6.2). A rigorous UTD formulation was developed by Rojas (9), using Wiener-Hopf techniques, for impedance discontinuities in a planar surface and for impedance edges on a half-plane. This research was extended by Ly (7) to predict backscatter from uniform resistive strips connected to a PEC half-plane. Up to third order diffractions were included in the formulation, and predictions were found to compare very favorably to an independent MM solution. Edge-on backscatter from a PEC half-plane was reduced 20 dB by introduction of an exponential resistive taper (7:112). Further research by Rojas and Otero (10) used Ly's formulation as the basis to synthesize a desired frequency response from resistive strips attached to a PEC half-plane. The rigorous UTD solution for the scattered field was used in a cost function that was minimized to determine the resistive strip values.

Backscatter from a PEC half-plane was reduced more than 30 dB over a wide range of incident angles by synthesizing a piecewise-constant seven section resistive transformer (10:59).

### Problem Statement

This thesis will continue the investigation into the scattering characteristics of resistive strips and resistive-loaded conducting strips begun in (3), but will use the more rigorous UTD formulation of Rojas and Ly. Limitations of the improved model will be defined by comparing predictions to an independent MM formulation. The investigation of the scattering characteristics of resistive-loaded conducting strips will place emphasis on backscatter reduction.

### Approach

The development of the rigorous UTD model is the topic of Chapter II. First, generalized resistive boundary conditions are introduced that simplify the scattering problem for application of the Wiener-Hopf technique. Second, the single order diffraction coefficients derived from this technique are presented. Last, higher order diffractions used in the model are defined.

Chapter III introduces the resistive strip and resistive-loaded conducting strip geometry investigated in this thesis. Then, the theory presented in Chapter II is applied to this particular geometry. The computer code of (10) is modified for the resistive strip and resistive-loaded strip geometry, and backscatter predictions are presented. These predictions are compared to MM predictions and measurements to ascertain the validity of the UTD formulation. Finally, limitations of the UTD formulation are investigated.

Scattering characteristics of resistive-loaded conducting strips are contained in Chapter IV. Various constant and tapered loads are investigated to determine the level of

scattering reduction that can be expected for a conducting strip. Tradeoffs are conducted between broadside, sidelobe, and edge-on scattering reductions based on the resistive load.

Last, Chapter V concludes the thesis by summarizing the research effort and findings and by recommending further research possibilities.

## II. Theory

This chapter outlines the rigorous UTD formulation developed by Ly, Otero, and Rojas (7; 10) for prediction of electromagnetic scattering from resistive junctions. First, the general problem of electromagnetic scattering from the junction of two different dielectric/ferrite half-plane slabs will be presented. Generalized impedance boundary conditions will be reviewed that simplify the problem for application of Wiener-Hopf techniques. The Wiener-Hopf technique and Jones' Method rigorously solve the scattering problem. Second, appropriate simplifications to the general problem of two dielectric/ferrite half-planes will be made for the more specific case of infinitely thin resistive half-planes. The single order diffraction coefficients for the prediction of electromagnetic scattering from a resistive junction are detailed. Last, higher order diffractions of the UTD formulation are presented for more complicated planar strip geometry. Double and triple order diffractions are listed for the case of a resistive strip placed between two resistive half-planes. Also, double and triple order diffractions are defined for nonadjacent junctions in a multiple resistive strip geometry.

### Scattering from the Junction of Dissimilar Dielectric Half-Plane Slabs

Before the more specific case of diffraction from resistive junctions can be outlined, the more general problem should be explored. This general problem consists of two different dielectric/ferrite half-plane slabs joined as shown in Figure 2.1. Each slab has a unique relative permittivity,  $\epsilon_r$ , relative permeability,  $\mu_r$ , and thickness,  $t$ . Both  $\epsilon_r$  and  $\mu_r$  can be complex to account for lossy materials. The thickness is considered to be thin enough so simplifications to the boundary conditions can be applied. Also, each slab is infinite in the  $z$ -dimension; thus, the scattering problem is reduced to a two-dimensional one. The half-plane slabs are illuminated by a plane wave that can either be transverse

magnetic to the z-axis ( $TM_z$ , E-Polarization) or transverse electric to the z-axis ( $TE_z$ , H-Polarization). The observation point is in the near-field. The first step in solving for the junction diffraction is to replace the dielectric/ferrite half-planes with generalized impedance boundary conditions (7:4).

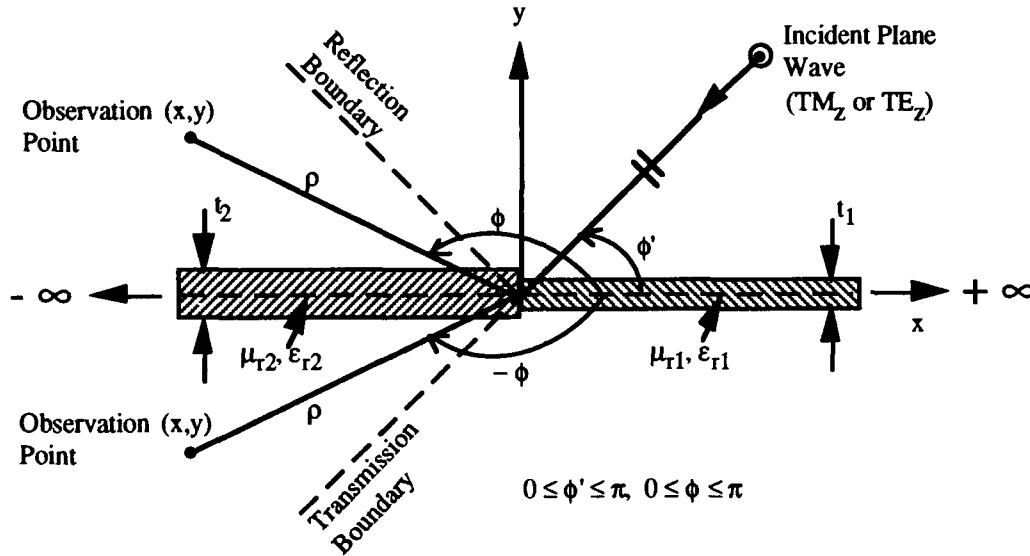


Figure 2.1. Two-Part Dielectric/Ferrite Plane Geometry (7:2)

Generalized Impedance Boundary Conditions. Weinstein has shown that if a partially transparent thin dielectric slab satisfies the condition

$$k\sqrt{\epsilon\mu}\frac{t}{2} \ll 1 \quad (2.1)$$

where  $k$  is the free space wavenumber,  $\epsilon$  is the slab permittivity,  $\mu$  is the slab permeability, and  $t$  is the slab thickness; then, the effect of the dielectric slab can be replaced by approximate "two-sided" boundary conditions. That is, both reflected and transmitted waves are considered so boundary conditions can be applied at  $y = 0^+$  and  $y = 0^-$  (12:301).

Ly applied Weinstein's concept of impedance boundary conditions to the two-part geometry shown in Figure 2.1. The boundary conditions were simplified by noting that for the two-dimensional problem the fields had no  $z$ -dependence. The final boundary conditions for  $TM_z$  incidence and  $TE_z$  incidence are presented in (7) and will not be repeated here.

Wiener-Hopf Technique. Once the boundary conditions are defined, the scattered field from the two-part geometry shown in Figure 2.1 can be determined using the Wiener-Hopf technique. The Wiener-Hopf technique was introduced in 1931 to solve a special type of integral equation. During World War II further work revealed that the technique was well suited for problems involving diffraction from semi-infinite planes. Solutions to these problems were formulated by both Schwinger and Copson by using Fourier integrals to find complex variable equations. The complex variable equations were solved using analytic continuation (8:vii). Rojas (9) used the Wiener-Hopf technique along with Jones' method to solve for the diffraction from an impedance discontinuity and impedance edge with oblique incidence. The Jones' method simplifies the Wiener-Hopf technique by applying Fourier transforms directly to the problem before applying the boundary conditions. After the boundary conditions are applied, the solution can be obtained by asymptotically evaluating the inverse Fourier transform of the scattered field (7:21). The asymptotic evaluation using steepest descent integration casts the solution in the UTD form.

The first step in using the Wiener-Hopf technique is to separate the scattering problem posed in Figure 2.1 into two parts:

$$u(x,y) = u^{up}(x,y) + u^p(x,y), \quad \forall(x,y) \quad (2.2)$$

where  $u(x,y)$  is the total field,  $u^{up}$  is the unperturbed field, and  $u^p$  is the perturbed field for any observation point. All the fields satisfy the two-dimensional Helmholtz equation. The total field is the scattered field that results from the two-part geometry. The unperturbed

field is the scattered field that would occur if just the right slab in Figure 2.1, with material parameters of  $\epsilon_{r1}$  and  $\mu_{r1}$ , was occupying the full plane. The unperturbed field is found by using the appropriate generalized impedance boundary conditions to derive reflection and transmission coefficients for the incident field (7:17). The perturbed field is the contribution to the total field by the impedance discontinuity that occurs by adding the left slab with material parameters of  $\epsilon_{r2}$  and  $\mu_{r2}$ . The perturbed field incorporates the junction diffraction as well as the change to the reflection and transmission coefficients for  $x < 0$ . Because the perturbed field must satisfy different generalized impedance boundary conditions at  $x > 0$  and  $x < 0$  caused by the change in material parameters, the Wiener-Hopf technique is chosen for its applicability to planar two-part geometries (7:19).

The next step for the Wiener-Hopf technique is to apply Fourier transformations to the perturbed field before applying the appropriate generalized impedance boundary conditions (7:20), i.e.,

$$\hat{u}^p(s,y) = \frac{1}{\sqrt{2\pi}} \int_{-\infty}^{\infty} u^p(x,y) e^{jsx} dx = \hat{u}_+^p(s,y) + \hat{u}_-^p(s,y) \quad (2.3)$$

where

$$\hat{u}_+^p(s,y) = \frac{1}{\sqrt{2\pi}} \int_0^{\infty} u^p(x,y) e^{jsx} dx \quad (2.4)$$

$$\hat{u}_-^p(s,y) = \frac{1}{\sqrt{2\pi}} \int_{-\infty}^0 u^p(x,y) e^{jsx} dx \quad (2.5)$$

This is an application of Jones' Method (4) and leads to the solution of  $u^p(x,y)$  by applying appropriate generalized impedance boundary conditions to  $\hat{u}^p(s,y)$  and then taking the inverse Fourier transform of  $\hat{u}^p(s,y)$ . Without going through the detailed intermediate steps this results in (7:18,21,23,24):



$$u^p(x, y) = \frac{j}{2\pi} \int_{-\infty}^{\infty} \sin \phi \frac{Z_e' \left( \frac{s}{k} \cos \phi \right) \Lambda_e(s) \pm z_0 \Lambda_o(s)}{s - k \cos \phi} e^{\pm j\beta y} e^{-jsx} ds, \quad y \geq 0, |x| < \infty \quad (2.6)$$

where

$$Z_e' \left( \frac{s}{k} \cos \phi \right) = (\sin v_{1a} + \sin v_{1b}) (1 + \sin v_{2a} \sin v_{2b} - \cos^2 \phi) - (\sin v_{2a} + \sin v_{2b}) (1 + \sin v_{1a} \sin v_{1b} - \cos^2 \phi) \quad (2.7)$$

$$\sin v_{1a,2a} + \sin v_{1b,2b} = \begin{cases} -\mu_{r1,2} \sin \zeta_{1,2}, & TM_z \\ -\epsilon_{r1,2} \sin \zeta_{1,2}, & TE_z \end{cases} \quad (2.8)$$

$$\sin v_{1a,2a} \sin v_{1b,2b} = \begin{cases} -\frac{\mu_{r1,2} \epsilon_{r1,2} - 1}{\mu_{r1,2} - 1}, & TM_z \\ -\frac{\mu_{r1,2} \epsilon_{r1,2} - 1}{\epsilon_{r1,2} - 1}, & TE_z \end{cases} \quad (2.9)$$

$$\sin \zeta_{1,2} = \begin{cases} \frac{j}{k(\mu_{r1,2} - 1) \frac{t_{1,2}}{2}}, & TM_z \\ \frac{j}{k(\epsilon_{r1,2} - 1) \frac{t_{1,2}}{2}}, & TE_z \end{cases} \quad (2.10)$$

$$\Lambda_e(s) = G_-(s, v_{2a}) G_-(s, v_{2b}) G_-(-k \cos \phi, v_{2a}) G_-(-k \cos \phi, v_{2b}) \times G_+(s, v_{1a}) G_+(s, v_{1b}) G_+(-k \cos \phi, v_{1a}) G_+(-k \cos \phi, v_{1b}) \quad (2.11)$$

$$\Lambda_o(s) = G_-(s, \zeta_2) G_-(-k \cos \phi, \zeta_2) G_+(s, \zeta_1) G_+(-k \cos \phi, \zeta_1) \quad (2.12)$$

$$\beta = \sqrt{k^2 - s^2} \quad (2.13)$$

$G(s, \nu)$  is defined as:

$$G(s, \nu) = G_+(s, \nu) G_-(s, \nu) = \frac{k}{\beta + k \sin \nu} \quad (2.14)$$

The factorization of  $G(s, \nu)$  is described in Appendix C of (7) and will not be repeated here.

The Wiener-Hopf integral outlined in Eqs (2.6) through (2.14) can't be solved by conventional methods. Because of its complexity, an asymptotic evaluation using steepest descent integration is required. This casts the solution into the UTD form first formulated by Kouyoumjian and Pathak (6). Evaluation of the integral yields a surface wave field and a diffracted field emanating from the junction of the dielectric/ferrite slabs. Along with the geometric optics (GO) field derived from reflection and transmission coefficients, this results in a total scattered field of

$$u(\rho, \phi) = u^{GO}(\rho, \phi) + u^{sw}(\rho, \phi) + u^d(\rho, \phi), \quad 0 \leq \phi' \leq \pi, \quad -\pi \leq \phi \leq \pi \quad (2.15)$$

where  $u(\rho, \phi)$  is the total scattered field,  $u^{GO}(\rho, \phi)$  is the GO field,  $u^{sw}(\rho, \phi)$  is the surface wave field, and  $u^d(\rho, \phi)$  is the diffracted field (7:31). The diffracted field can be defined in terms of UTD diffraction coefficients as follows (7:32):

$$u^d(\rho, \phi) \sim \frac{e^{jk\rho}}{\sqrt{\rho}} [D^e(\phi, \phi', \nu_1, \nu_2) + D^o(\phi, \phi', \zeta_1, \zeta_2)] \quad (2.16)$$

The UTD diffraction coefficients in Eq (2.16) are complicated and will not be repeated here. These diffraction coefficients are the starting point for the case of scattering from the junction of resistive half-planes.

### Scattering from the Junction of Resistive Half-Planes

The UTD diffraction coefficients outlined in the previous section can be simplified for resistive materials. In Figure 2.1, the dielectric/ferrite slabs were assigned material

parameters of  $\epsilon_{r1,2}$ ,  $\mu_{r1,2}$ , and  $t_{1,2}$  where both  $\epsilon_{r1,2}$  and  $\mu_{r1,2}$  can be complex. If the following conditions are satisfied, the dielectric/ferrite slabs are reduced to infinitely thin resistive sheets (7:36):

$$\begin{aligned} \mu_{r1,2} &= 1 \\ t_{1,2} &\rightarrow 0 \\ \lim_{t_{1,2} \rightarrow 0} \frac{j}{k(\epsilon_{r1,2} - 1)t_{1,2}} &= \frac{R_{1,2}}{Z_0} \end{aligned} \quad (2.17)$$

where  $R_{1,2}$  are real resistances and  $Z_0$  is the free space wave impedance. Under these conditions the following simplifications can be applied to the two-part dielectric/ferrite solution (7:36,37):

$$\left. \begin{aligned} |\sin \zeta| &\rightarrow \infty \\ |\sin v_d| &\rightarrow \infty \\ \sin v_b &\rightarrow \frac{Z_0}{2R} \end{aligned} \right\} TM_z \quad (2.18)$$

$$\left. \begin{aligned} \sin \zeta &\rightarrow \frac{2R}{Z_0} \\ |\sin v_d| &\rightarrow \infty \\ \sin v_b &\rightarrow 0 \end{aligned} \right\} TE_z \quad (2.19)$$

yielding a diffracted field of (7:38):

$$u(\rho, \phi) \sim \begin{cases} \frac{e^{jk\rho}}{\sqrt{\rho}} D^e(\phi, \phi'; \gamma, \gamma_2), & TM_z \\ \frac{e^{jk\rho}}{\sqrt{\rho}} D^o(\phi, \phi'; \gamma, \gamma_2), & TE_z \end{cases} \quad (2.20)$$

where (7:33,34,38,134):

$$D^e(\phi, \phi'; \eta, \eta) = \frac{e^{j\frac{\pi}{4}}}{\sqrt{2\pi k}} (\sin \eta - \sin \eta) g_+ \left( \begin{matrix} \phi \\ 2\pi - \phi, \eta \end{matrix} \right) g_- \left( \begin{matrix} \phi \\ 2\pi - \phi, \eta \end{matrix} \right) \\ \times g_+(\phi', \eta) g_-(\phi', \eta) \left| \cos \frac{\phi}{2} \right| \cos \frac{\phi}{2} \left[ \frac{F(-k\rho a^-)}{\cos \left( \frac{\phi - \phi'}{2} \right)} - \frac{F(-k\rho a^+)}{\cos \left( \frac{\phi + \phi'}{2} \right)} \right], \quad (2.21)$$

$$\begin{cases} 0 \leq \phi \leq \pi \\ \pi \leq \phi \leq 2\pi \end{cases}$$

$$D^o(\phi, \phi'; \eta, \eta) = \frac{e^{j\frac{\pi}{4}}}{\sqrt{2\pi k}} (\sin \eta - \sin \eta) g_+ \left( \begin{matrix} \phi \\ 2\pi - \phi, \eta \end{matrix} \right) g_- \left( \begin{matrix} \phi \\ 2\pi - \phi, \eta \end{matrix} \right) \\ \times g_+(\phi', \eta) g_-(\phi', \eta) \sin \frac{\phi}{2} \sin \frac{\phi}{2} \left[ \frac{F(-k\rho a^-)}{\cos \left( \frac{\phi - \phi'}{2} \right)} - \frac{F(-k\rho a^+)}{\cos \left( \frac{\phi + \phi'}{2} \right)} \right], \quad (2.22)$$

$$\begin{cases} 0 \leq \phi \leq \pi \\ \pi \leq \phi \leq 2\pi \end{cases}$$

$$\sin \eta_{1,2} = \begin{cases} \frac{Z_0}{2R_{1,2}}, & TM_z \\ \frac{2R_{1,2}}{Z_0}, & TE_z \end{cases} \quad (2.23)$$

$$g_{+,-}(w, v) = \begin{cases} \tilde{g}_{+,-}(w, v), & 0 < \operatorname{Re} v < \frac{\pi}{2} \\ \tilde{g}_{+,-}(w, -\pi - v), & -\frac{\pi}{2} < \operatorname{Re} v < 0, \operatorname{Im} v < 0 \\ \tilde{g}_{+,-}(w, \pi - v), & -\frac{\pi}{2} < \operatorname{Re} v < 0, \operatorname{Im} v > 0 \end{cases} \quad (2.24)$$

$$\tilde{g}_{+}(w, v) = \frac{e^{l(\pi - w, v)/2\pi}}{\sqrt{\cos v - \cos w}} \quad (2.25)$$

$$\tilde{g}_-(w, v) = \frac{e^{I(w, v)/2\pi}}{\sqrt{\cos v - \cos w}} \quad (2.26)$$

$$I(w, v) = \int_{w+v}^{w-v} \frac{t}{\sin t} dt \quad (2.27)$$

$$F(x) = 2j\sqrt{x}e^{jx} \int_{\sqrt{x}}^{\infty} e^{-t^2} dt, \quad -\frac{3\pi}{2} < \arg(x) < \frac{\pi}{2} \quad (2.28)$$

$$a^{\pm} = 2 \cos^2 \left( \frac{\phi \pm \phi'}{2} \right) \quad (2.29)$$

Eqs (2.21) through (2.29) define the single-order UTD diffraction coefficients for resistive junctions. Both E-Polarization and H-Polarization cases are defined for the case of plane wave incidence and near-field observation point.

For far-zone observation points the diffraction coefficients can be simplified further. As  $x \rightarrow \infty$  in Eq (2.28),  $F(x)$  approaches one.  $F(x)$  is the standard transition function introduced in (6) for UTD diffraction coefficients. Thus, for a far-zone observation point, i.e.,  $kr \rightarrow \infty$ , the single diffraction coefficient for  $TM_z$  reduces to:

$$\begin{aligned} D_1(\phi, \phi'; \eta, \eta) &= \frac{e^{j\pi/4}}{\sqrt{2\pi k}} (\sin \eta - \sin \eta) g_+(\pm\phi, \eta) g_+(\phi', \eta) \\ &\times g_-(\pm\phi, \eta) g_-(\phi', \eta) \sin(\pm\phi) \frac{\sin \phi}{\cos \phi + \cos \phi'}, \end{aligned} \quad (2.30)$$

$$\begin{cases} 0 \leq \phi \leq \pi \\ -\pi \leq \phi \leq 0 \end{cases}$$

For the  $TE_z$  case,  $\sin(\pm\phi)$  is replaced by  $\sin \phi$ .

## Multiple Diffractions

For more complicated resistive strip geometries, multiple (higher order) diffractions may contribute an important amount to the total scattered field. This contribution is more significant if the diffracted field from one resistive junction is not ray-optical when it illuminates a second resistive junction. The first geometry to examine where higher order diffractions occur is presented in Figure 2.2. A resistive strip of length  $d$  is placed between two resistive half-planes creating two junctions where multiple diffractions can occur. Each resistive section is infinitely thin and has a unique resistance,  $R$ . Plane-wave illumination is  $TM_z$  or  $TE_z$  with the observation point in the far-zone. The far-zone case is chosen because of greater interest; in addition, the near-field multiple diffraction solution is much more difficult to derive. Double and triple order diffractions between points  $Q_1$  and  $Q_2$  in Figure 2.2 were derived for both top and bottom face propagation (7:40,41).

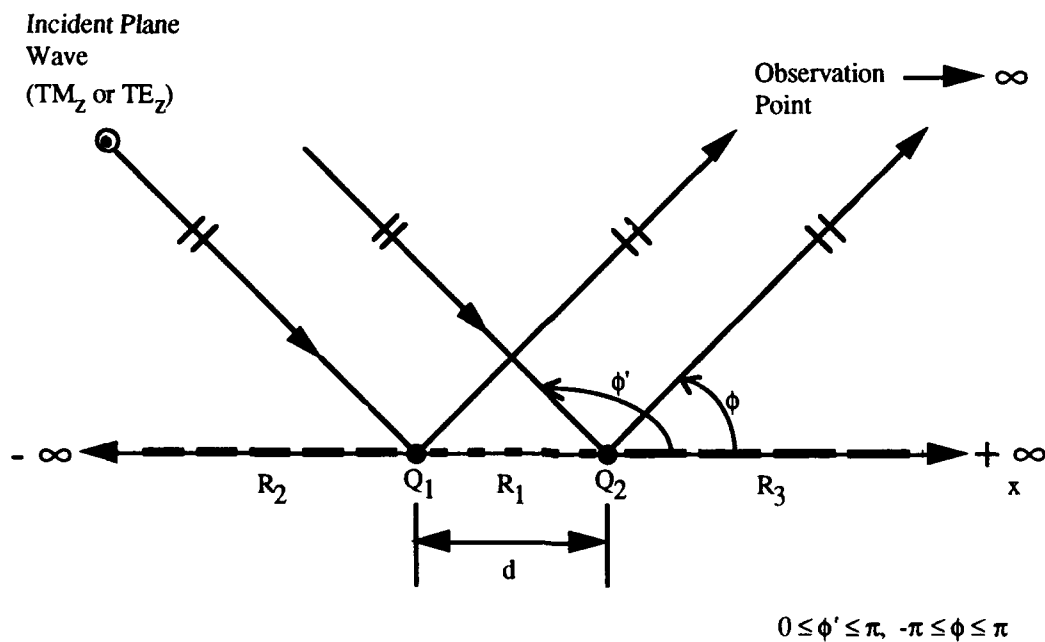


Figure 2.2. Three-Part Resistive Plane Geometry (7:70)

Examining Eq (2.30) reveals that the single diffraction coefficient is equal to zero when the incident or observation angle is  $0^\circ$  or  $180^\circ$ . This is an artifact of the single diffraction solution. Thus, due to the planar geometries considered, if one were to calculate a multiple diffracted field by repeated application of the appropriate single diffraction coefficient, an incorrect field value of zero would result. However, if the multiple diffracted fields are calculated via the modified spectral ray method (MSRM) developed in (11), this problem does not occur. Even if this artifact of the single diffraction solution did not exist, repeated application of single diffraction coefficients would be invalid when the diffracted field from one resistive junction is not ray-optical upon illuminating a second junction. The MSRM was specifically developed to surmount this latter difficulty. Thus, the MSRM was used in (7) for determination of all multiple diffracted fields. MSRM treats the first diffraction on the second edge as an infinite sum of inhomogeneous plane waves. This is accomplished by defining the first diffraction in terms of the steepest descent integral that was used in the derivation of the single diffraction coefficient. In effect, the exact single diffracted field in steepest descent integral form is used as the illuminating field on the second junction and then the asymptotic evaluation occurs (7:45,47). MSRM similarly solves the triple diffraction solution. Ly derives the double and triple diffraction coefficients for the more general case of a dielectric/ferrite three-part geometry. Simplified for resistive materials, the double and triple diffraction coefficients for  $TM_z$  are (7:71,72):

$$\begin{aligned}
 D_2(\phi, \phi'; \eta, \eta_2, \eta_3) &= \frac{j}{\pi k} \frac{e^{jkd}}{\sqrt{d}} (\sin \eta - \sin \eta_2) (\sin \eta - \sin \eta_3) \sin(\pm \phi) \sin \phi \\
 &\times g_+(\pm \phi, \eta) g_+(\phi', \eta) g_-(\pm \phi, \eta_2) g_-(\phi', \eta_2) \\
 &\times g_+^2(0, \eta) g_-(0, \eta_2) g_-(0, \eta_3) a_\gamma \left[ \frac{1 - F(-kda_1)}{(a_1 - a_2)(a_1 - a_\gamma)} \right. \\
 &\left. + \frac{1 - F(-kda_2)}{(a_2 - a_1)(a_2 - a_\gamma)} + \frac{1 - F(-kda_\gamma)}{(a_\gamma - a_2)(a_\gamma - a_1)} \right], \quad \begin{cases} 0 \leq \phi \leq \pi \\ -\pi < \phi < 0 \end{cases}
 \end{aligned} \tag{2.31}$$

$$\begin{aligned}
D_3(\phi, \phi'; \eta, \eta_2, \eta_3) &= e^{j3\pi/4} \sqrt{\frac{2}{(\pi k)^3}} \frac{e^{jk2d}}{d} (\sin \eta - \sin \eta_2)^2 (\sin \eta - \sin \eta_3) \\
&\times \sin(\pm\phi) \sin \phi g_+(\pm\phi, \eta) g_+(\phi', \eta) g_-(\pm\phi, \eta_2) g_-(\phi', \eta_2) \\
&\times g_+^4(0, \eta) g_-^2(0, \eta_2) g_-^2(0, \eta_3) a_\gamma^2 \frac{F(-kda_2) - F(-kda_\gamma)}{(a_2 - a_\gamma)} \\
&\times \left[ \frac{1 - F(-kda_1)}{(a_1 - 2)(a_1 - a_\gamma)} + \frac{1 - F(-2kd)}{(2 - a_1)(2 - a_\gamma)} + \frac{1 - F(-kda_\gamma)}{(a_\gamma - 2)(a_\gamma - a_1)} \right], \quad (2.32) \\
&\begin{cases} 0 \leq \phi \leq \pi \\ -\pi < \phi < 0 \end{cases}
\end{aligned}$$

where

$$\begin{cases} a_1 = 2 \cos^2 \frac{\phi}{2} \\ a_2 = 2 \cos^2 \frac{\phi}{2} \\ a_\gamma = 2 \sin^2 \frac{\eta}{2} \end{cases} \quad (2.33)$$

$$\sin \eta_{1,2,3} = \begin{cases} \frac{Z_0}{2R_{1,2,3}}, & TM_z \\ \frac{2R_{1,2,3}}{Z_0}, & TE_z \end{cases} \quad (2.34)$$

For the  $TE_z$  case,  $\sin(\pm\phi)$  is replaced by  $\sin \phi$  in Eqs (2.31) and (2.32).

The second strip geometry to consider is when  $R_1$  in Figure 2.2 is replaced by several resistive strips where higher order diffractions can occur between both adjacent and non-adjacent junctions. The lengths and resistances of the strips may vary. Eqs (2.31) and (2.32) can be used to calculate the double and triple diffractions between the adjacent junctions. Otero and Rojas (10) used the same MSRM technique as Ly to define the double and triple diffraction coefficients for points  $Q_{1,2}$  and non-adjacent junctions. As Figure 2.3 shows, the only difference is that four different resistances must be considered in the formulation rather than just three different resistances for the adjacent junction case. These



diffraction coefficients are very similar to Eqs (2.31) and (2.32); thus, will not be repeated here. Interested readers may consult (10) for more detail.

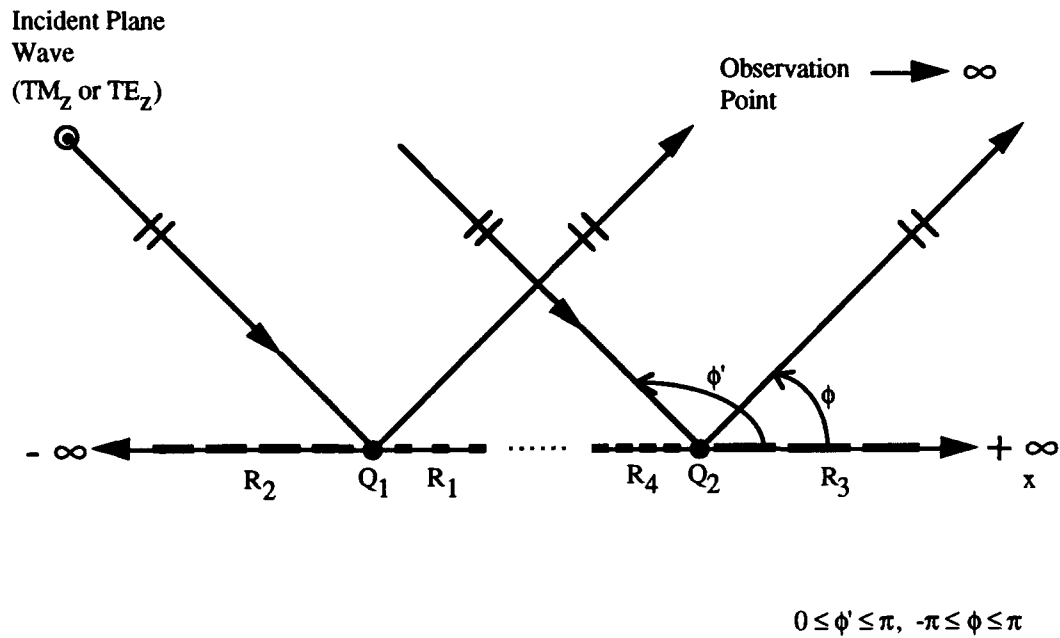


Figure 2.3. Four-Part Resistive Plane Geometry (10:11)

### III. Resistive Strips and Resistive-Loaded Conducting Strips

This chapter introduces the resistive strip and resistive-loaded conducting strip geometries investigated in this thesis. Next, the theory presented in the previous chapter is applied to these particular geometries. Verification of the rigorous UTD formulation is accomplished by comparison to an independent MM code and measurements. Finally, limitations of the rigorous UTD formulation are explored.

#### Geometry

The specific strip geometry is shown in Figure 3.1. A resistive strip or resistive-loaded conducting strip of width,  $d$ , is assumed to be infinite in the  $z$ -dimension. The observation point is collocated with the source in the far-zone ( $\rho = \rho' \rightarrow \infty, \phi = \phi'$ ). The angle  $\theta$  is defined as degrees from broadside and plots of scattering width will be presented with  $\theta$  as the independent variable.

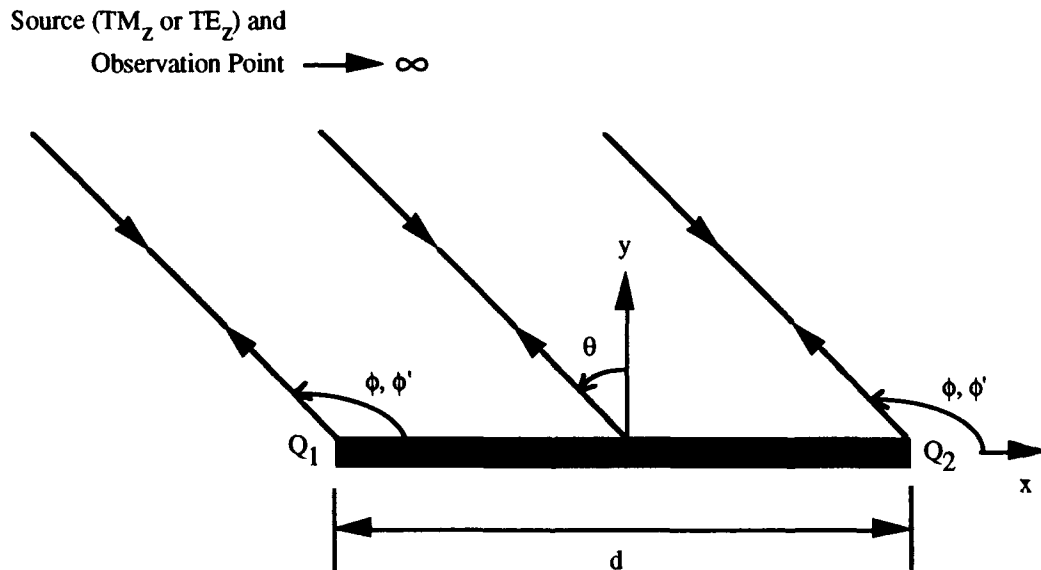
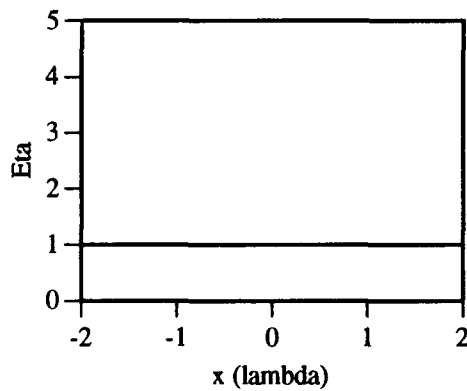
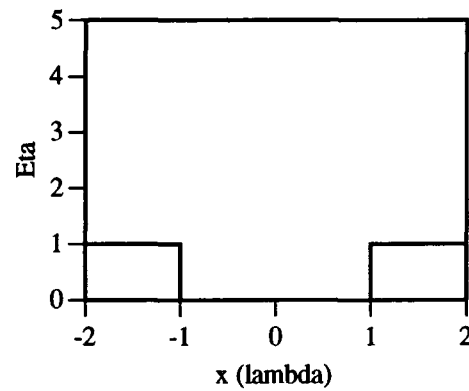


Figure 3.1. Strip Geometry

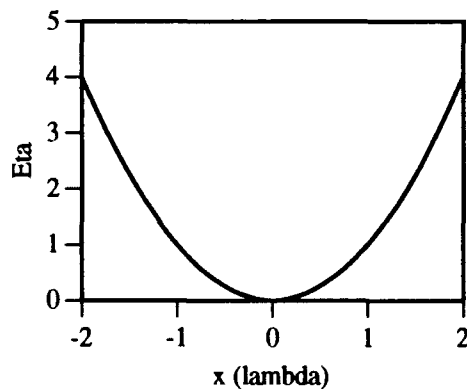
Four types of resistive strips and resistive-loaded conducting strips were examined for this thesis effort. The four types were constant resistive strips, constant resistive-loaded conducting strips, tapered resistive strips, and tapered resistive-loaded conducting strips. Examples of the various strip resistances as a function of  $x$ , where  $x$  is in wavelengths, are contained in Figure 3.2. All resistances, denoted by  $\eta$ , are normalized to the free space wave impedance,  $Z_0$ .



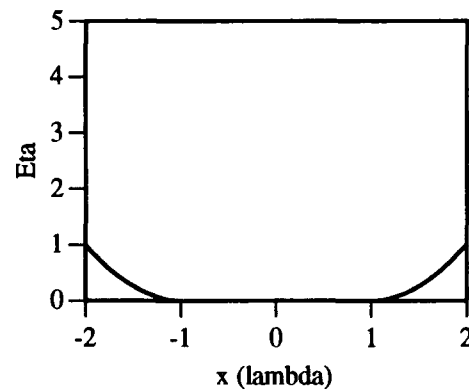
a. Constant Resistive Strip,  $\eta = 1$



b. Constant Resistive-Loaded Conducting Strip,  $\eta = 1$



c. Tapered Resistive Strip,  $\eta = x^2$



d. Tapered Resistive-Loaded Conducting Strip,  $\eta = (|x| - 1)^2$

Figure 3.2. Normalized Resistances of Different Strip Geometries

All types of strips investigated in this thesis were four wavelengths in width. This width was chosen based on the amount of lobing that occurs. For larger widths, i.e., larger electrical width, increased lobing occurs that makes the analysis more difficult, especially when comparing predictions to measurements. Also, Figure 3.2 shows that all the strip resistances are modeled for symmetry around  $x = 0$ .

### Application of Theory

In the previous chapter, single diffraction coefficients were defined for resistive junctions. Also, double and triple diffraction coefficients were defined for adjacent and nonadjacent resistive junctions. The computer code of (10) uses these UTD diffraction coefficients for predicting the far-zone scattering width of a PEC half-plane loaded with constant resistive strips. The length and resistance of each strip could be entered through a data file, and up to fifty strips could be input into the program. Also, the computer code could synthesize the resistances for a set number of equal length strips attached to a PEC half-plane based on a desired frequency response. Either  $TM_z$  or  $TE_z$  could be specified in the input data file, as well as inclusion of multiple diffractions. As an example, Figure 3.3 shows the scattering width of a PEC half-plane and of a PEC half-plane loaded with two  $0.354\lambda$  resistive strips for  $TM_z$ . The prediction for the loaded PEC half-plane includes multiple diffractions. Note the non-symmetry inherent in the scattering pattern of the loaded PEC half-plane, as well as the reduction in scattering width by the application of resistive loads.

For the purposes of this thesis, the scattering prediction portion of the computer code was modified for the strip geometries described in Figure 3.2. Since the resistances are symmetrical on these geometries, the scattering patterns found will also be symmetrical, as in the example shown in Figure 3.4. Thus, for subsequent plots, the scattering width will be presented with  $\theta$  (degrees from broadside) varying from  $0^\circ$  to  $90^\circ$ . Conducting strips were modeled in the computer code by assigning them a low resistance; i.e.,

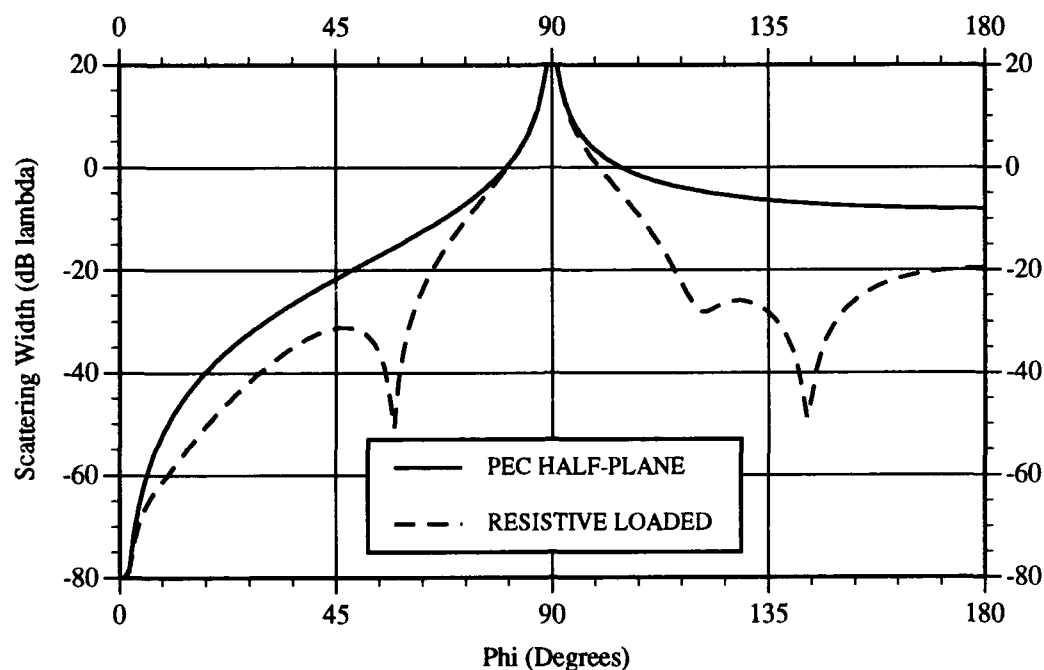


Figure 3.3. Scattering Prediction for a PEC Half-Plane and Loaded PEC Half-Plane,  $0.354\lambda$  Loads,  $R_1 = 121\Omega$ ,  $R_2 = 624\Omega$ ,  $TM_z$ , Multiple Diffractions (10:37)

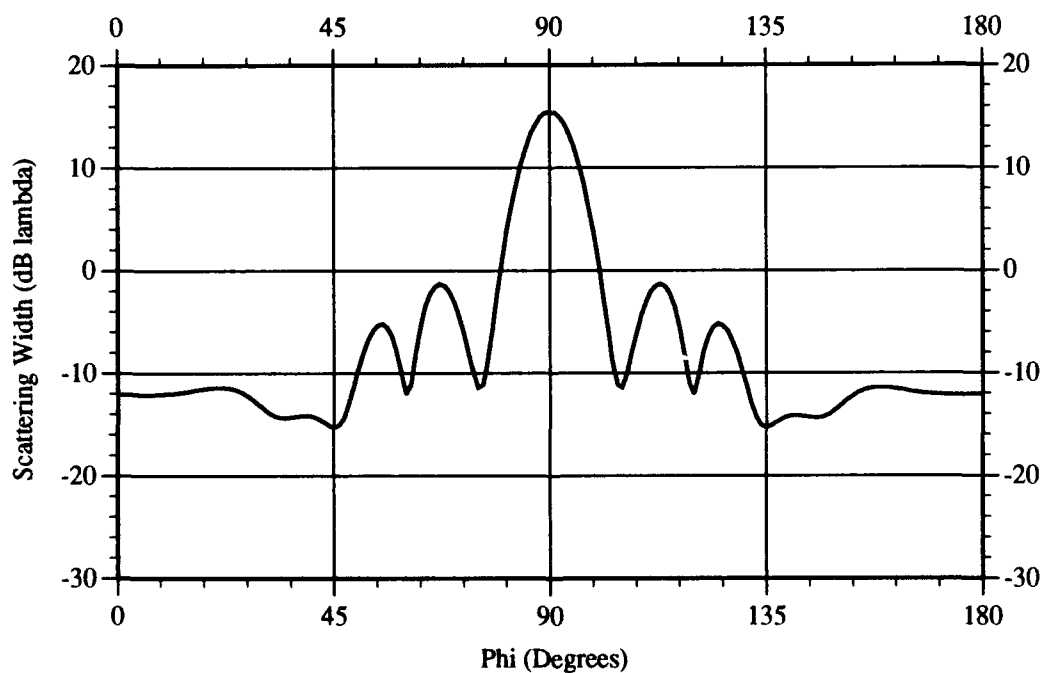


Figure 3.4. Scattering Prediction for a  $2\lambda$  Conducting Strip with  $1\lambda$  Constant Resistive Loads,  $\eta = 2$ ,  $TM_z$ , Multiple Diffractions

$\eta = 0.001$ . Resistive tapers were input into the computer code by modeling them as discrete resistive strips, as shown in Figure 3.5. For this thesis, unless stated otherwise, ten segments per wavelength were used for the taper modelling. To facilitate use of the scattering prediction code, a program was developed to write the various strip geometries shown in Figure 3.2 to the main program's input data file.

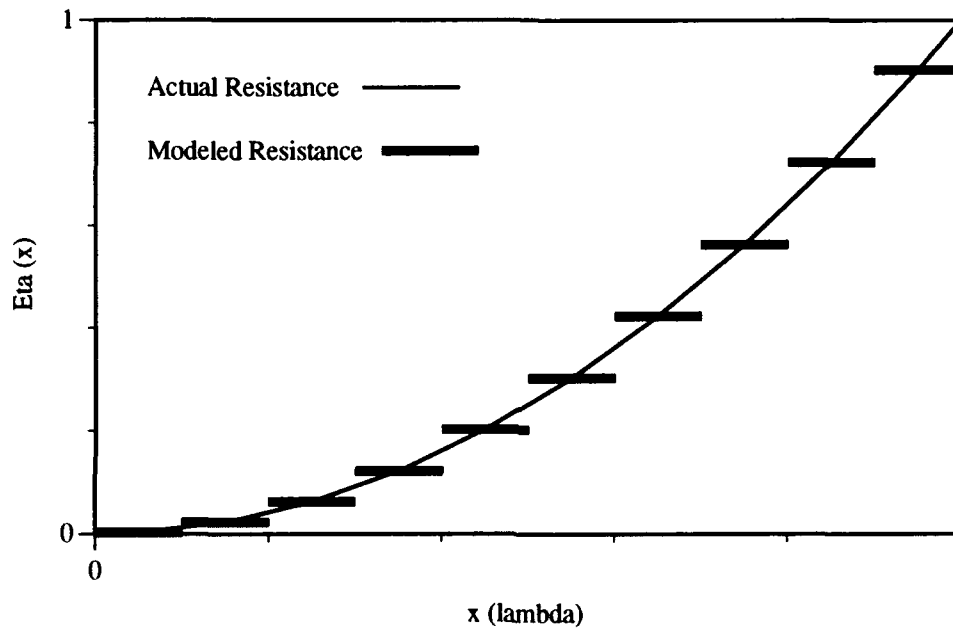


Figure 3.5. Resistive Taper,  $\eta = x^2$ , Modeled With Discrete Resistive Strips, Ten Segments Per Wavelength

### Verification

The rigorous UTD formulation was verified by comparing scattering width predictions to an independent MM code used in (2) and measurements conducted in the AFIT RCS Measurement Chamber.

MM Comparison. Haupt (2) developed a MM code to predict scattering from the strip geometries described in Figure 3.2. The incident field was related to the surface current density on the strip as follows (2:12,13):

$$H_o e^{jkx \cos \phi_o} = \eta(x) J_z(x) + \frac{k}{4} \int_{-d/2}^{d/2} J_z(x') H_0^{(2)}(k|x-x'|) dx', \quad TM_z \quad (3.1)$$

$$H_o \sin \phi_o e^{jkx \cos \phi_o} = \eta(x) J_x(x) + \frac{k}{4} \int_{-d/2}^{d/2} J_x(x') \frac{1}{k|x-x'|} H_1^{(2)}(k|x-x'|) dx', \quad TE_z \quad (3.2)$$

where  $H_o$  is the magnitude of the incident magnetic field,  $\phi_o$  is the source angle measured from the positive x-axis,  $\eta(x)$  is the strip resistance, and  $J_{z,x}(x)$  are the unknown surface current densities. The unknown surface current densities are solved using the MM numerical technique for integral equations. Pulse basis functions and midpoint integration routines are used in the MM code. The number of basis functions can be varied through a data input file (2:16-26). Once the surface current densities are known the scattering width is calculated as follows (2:40):

$$\sigma_{2D} = \frac{k}{4H_o^2} \left| \int_{-d/2}^{d/2} J_z(x') e^{jkx' \cos \phi_o} dx' \right|^2, \quad TM_z \quad (3.3)$$

$$\sigma_{2D} = \frac{k}{4H_o^2} \left| \sin \phi_o \int_{-d/2}^{d/2} J_x(x') e^{jkx' \cos \phi_o} dx' \right|^2, \quad TE_z \quad (3.4)$$

Comparisons to MM were made for constant resistive strips, constant resistive-loaded conducting strips, tapered resistive strips, and tapered resistive-loaded conducting strips. The rigorous UTD solution includes multiple diffractions unless otherwise noted.

**Constant Resistive Strips.** Scattering width predictions for strips with constant resistance are contained in Figures 3.6 through 3.13. In Figures 3.6 and 3.7, predictions are made for a  $4\lambda$  conducting strip ( $\eta = 0$ ) for  $TM_z$  and  $TE_z$ , respectively. Usually, the number of pulse basis functions used in the MM solution for accurate

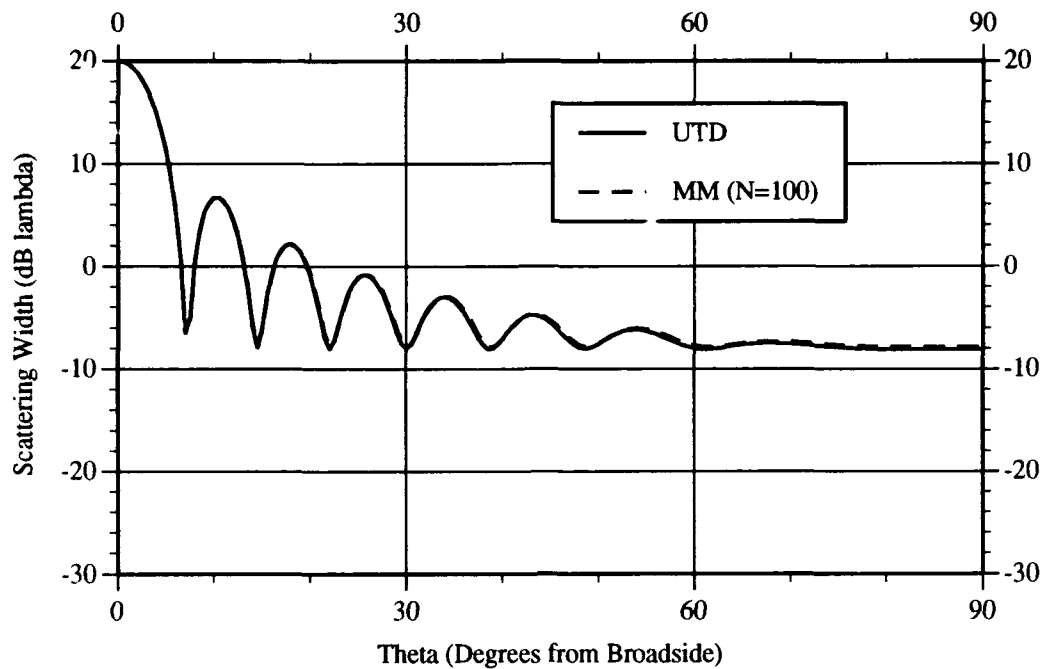


Figure 3.6. Scattering Prediction for a  $4\lambda$  Conducting Strip,  $TM_z$

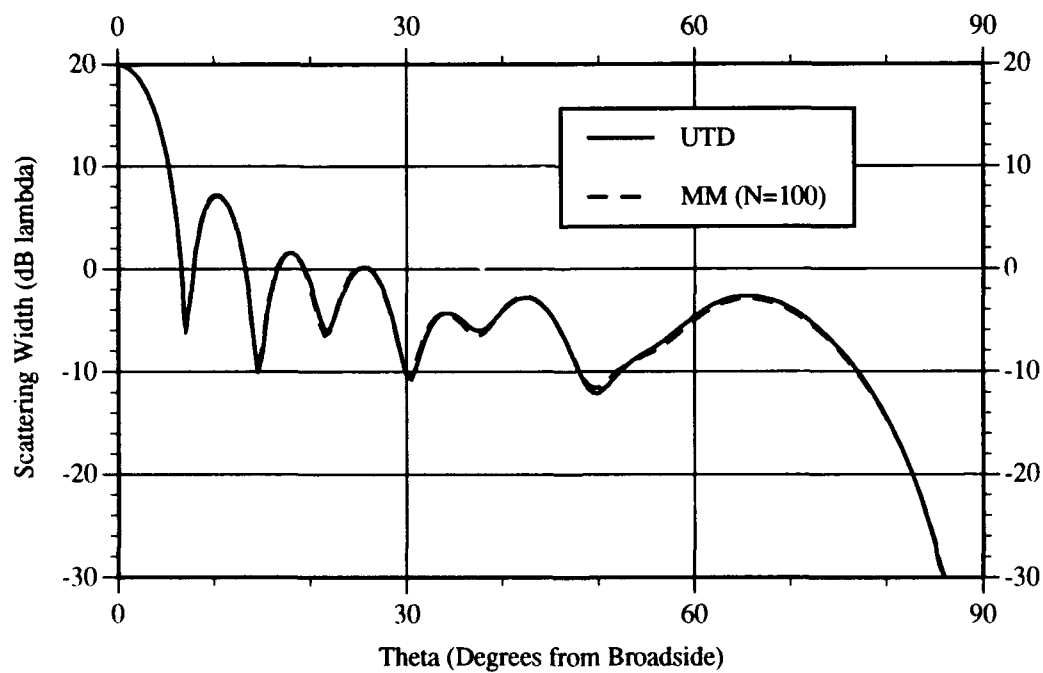


Figure 3.7. Scattering Prediction for a  $4\lambda$  Conducting Strip,  $TE_z$



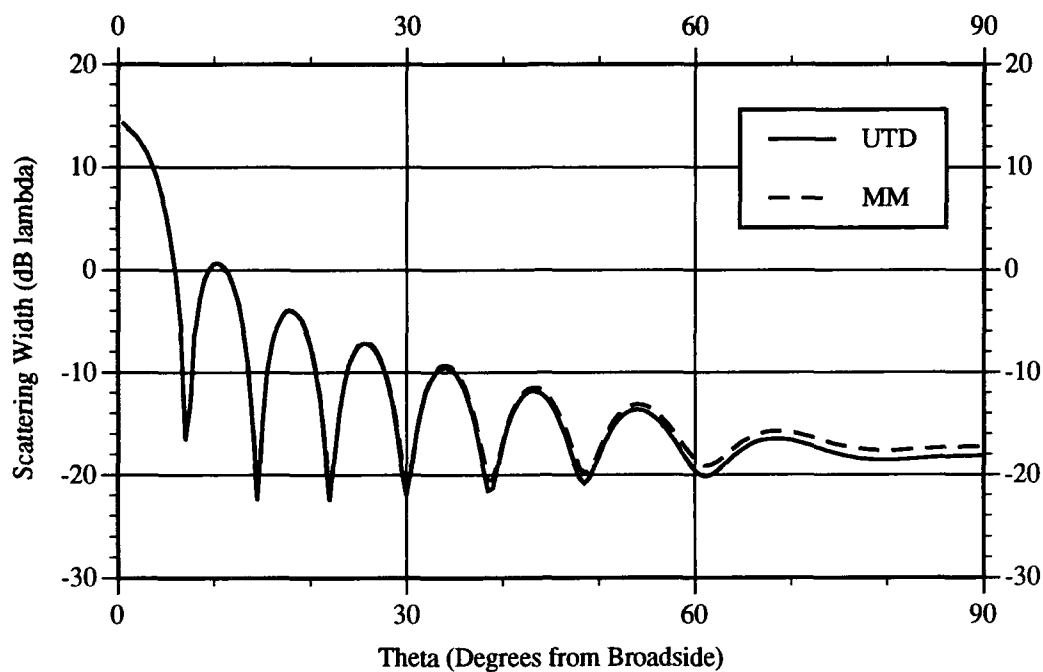


Figure 3.8. Scattering Prediction for a  $4\lambda$  Constant Resistive Strip,  $\eta = 0.5$ ,  $TM_z$

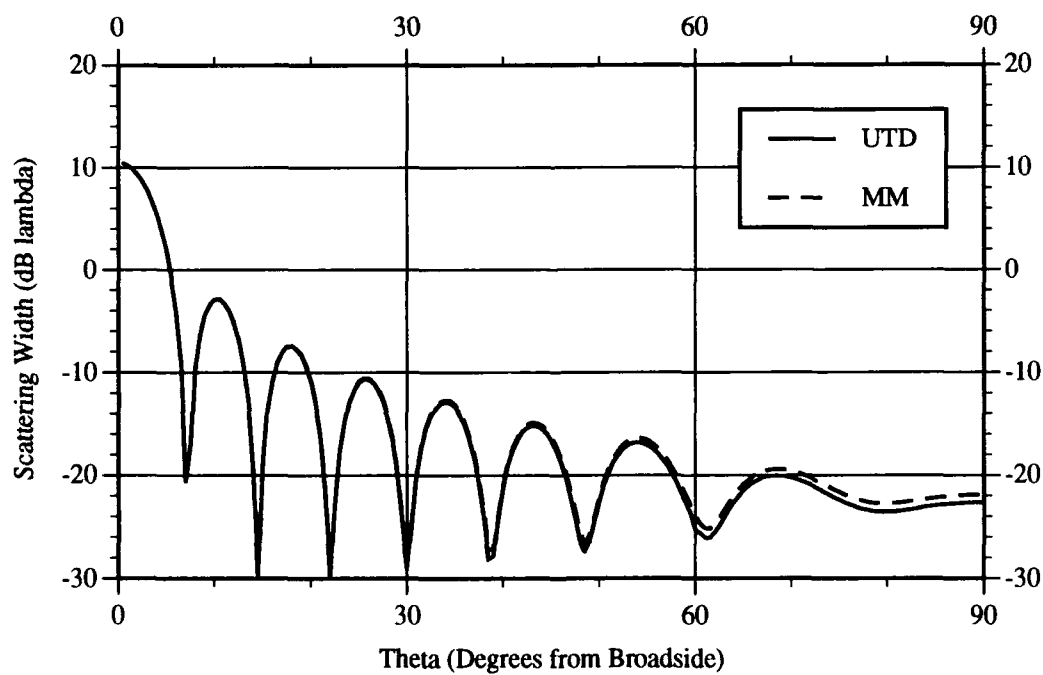


Figure 3.9. Scattering Prediction for a  $4\lambda$  Constant Resistive Strip,  $\eta = 1$ ,  $TM_z$

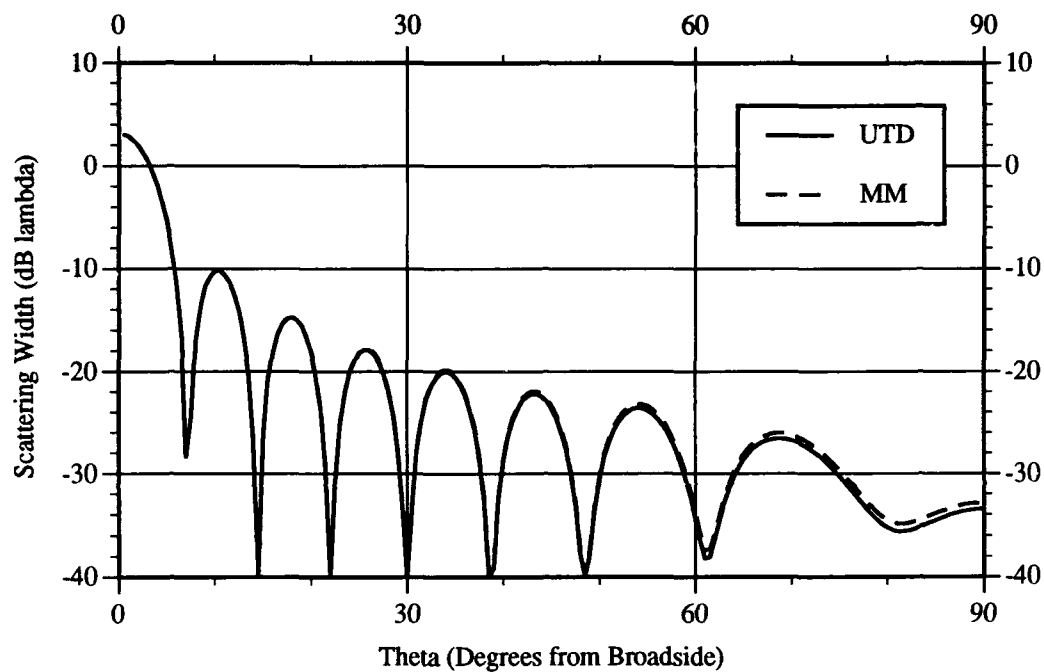


Figure 3.10. Scattering Prediction for a  $4\lambda$  Constant Resistive Strip,  $\eta = 3$ ,  $TM_z$

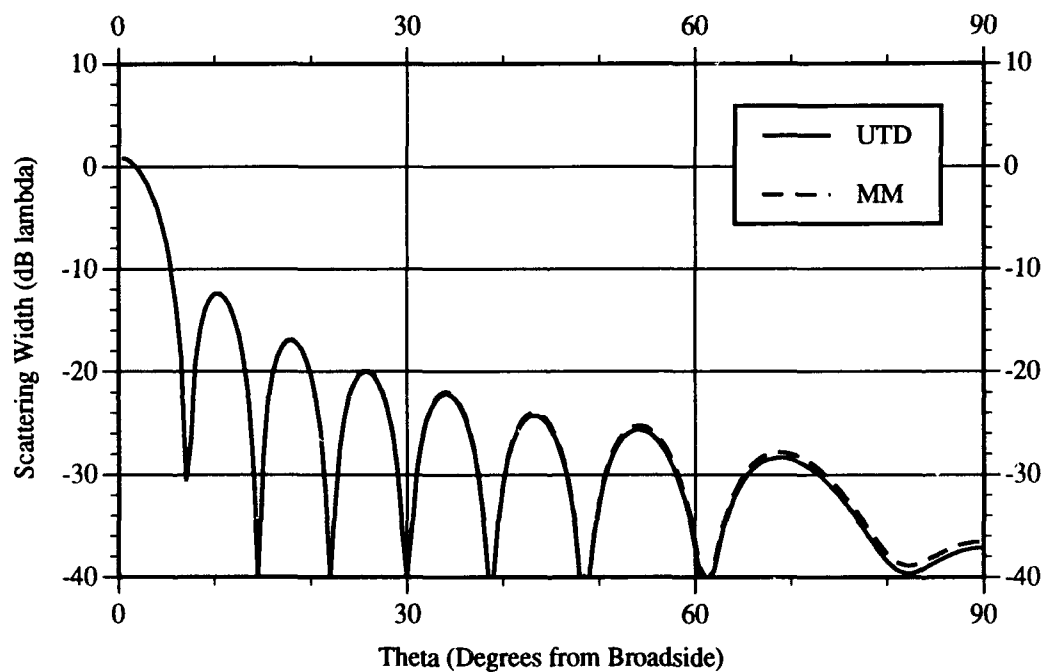


Figure 3.11. Scattering Prediction for a  $4\lambda$  Constant Resistive Strip,  $\eta = 4$ ,  $TM_z$

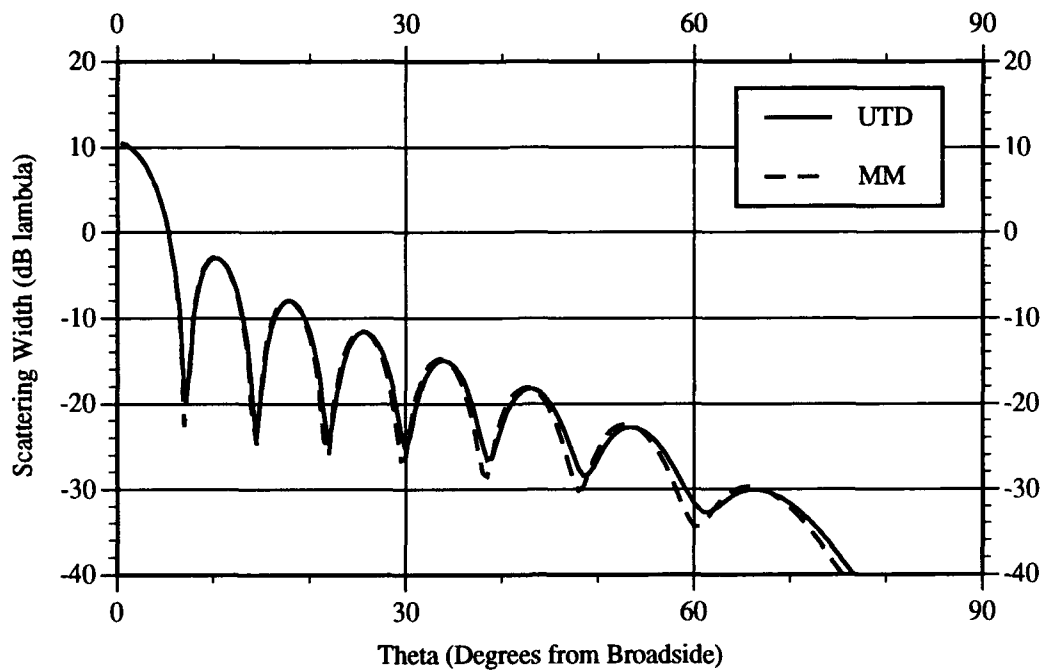


Figure 3.12. Scattering Prediction for a  $4\lambda$  Constant Resistive Strip,  $\eta = 1$ ,  $TE_z$

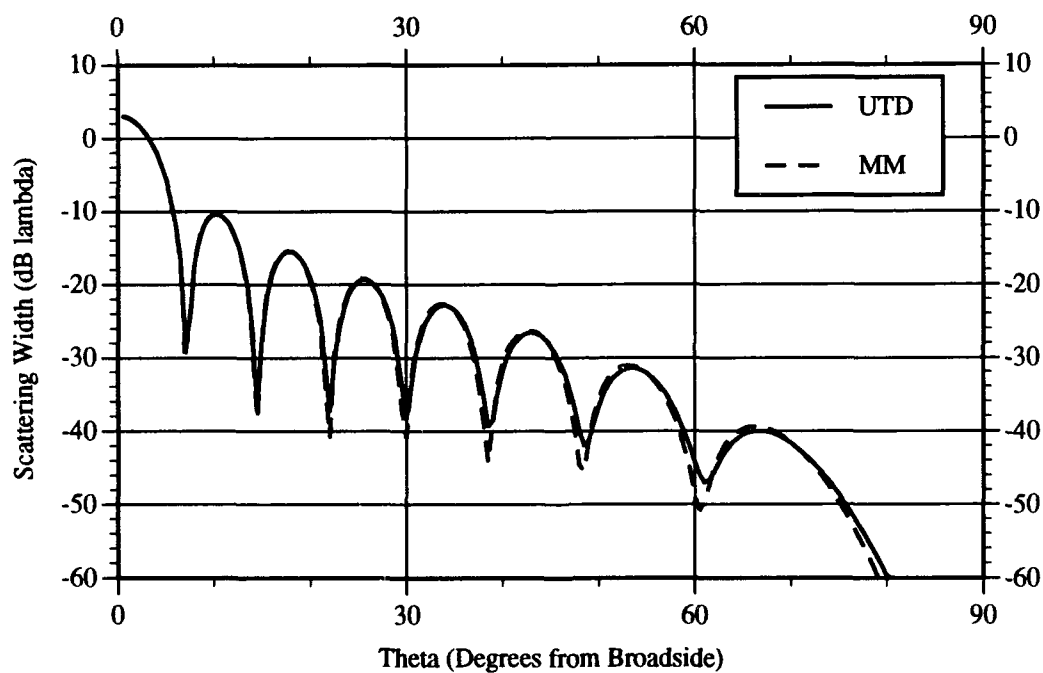


Figure 3.13. Scattering Prediction for a  $4\lambda$  Constant Resistive Strip,  $\eta = 3$ ,  $TE_z$

solutions is ten per wavelength; however, for conducting strips Haupt noted that more pulse basis functions were required to obtain accurate results (2:25,26). Thus, the number of pulse basis functions for the case of a conducting strip is chosen as 25 per wavelength. All other MM predictions in this thesis use ten pulse basis functions per wavelength. As Figures 3.6 shows, the UTD prediction for a  $4\lambda$  conducting strip with  $TM_z$  incidence compares almost exactly with the moment method prediction. The slightest deviation occurs only towards edge-on and is approximately 0.2 dB. For the same conducting strip with  $TE_z$  incidence the UTD prediction again compares almost exactly to the moment method solution as shown in Figure 3.7. The location of the peak of the traveling wave lobe for  $TE_z$  is predicted by (5:149) to be:

$$\theta = 49.35 \sqrt{\lambda/l} \quad (3.5)$$

where  $\theta$  is measured from edge-on,  $\lambda$  is the wavelength, and  $l$  is the width of the strip in wavelengths. For a  $4\lambda$  conducting strip, the traveling wave lobe is calculated to be approximately  $25^\circ$  from edge-on, or  $65^\circ$  from broadside. This agrees with both the UTD and MM prediction. For constant resistive strips with  $TM_z$  incidence, the UTD prediction compares very favorably to the MM prediction. As the resistance increases no discernible change in the comparison occurs. Towards edge-on, the difference between predictions in Figures 3.8 through 3.11 is less than 1 dB. Figures 3.12 and 3.13 show the excellent agreement between predictions for  $TE_z$  incidence. Overall, as the resistance increases the scattering patterns decrease as compared to a conducting strip for both polarizations. For  $TM_z$ , the sidelobes are not reduced relative to the main lobe, although the nulls deepen as the resistance increases. In effect, the scattering pattern is scaled down by the increase in resistance. For  $TE_z$ , the sidelobes are reduced from the main lobe and the pattern's shape changes.

Constant Resistive-Loaded Conducting Strips. Figures 3.14 through 3.19 show the scattering width predictions for various constant resistive-loaded conducting strips. All cases have a  $2\lambda$  conducting strip in the center with  $1\lambda$  resistive loads on each side. For  $TM_z$ , Figures 3.14 through 3.17 show the excellent agreement between the UTD and MM predictions. As the resistive loads increase from  $\eta = 0.5$  to 4, the differences in predictions remain less than 1 dB towards edge-on. However, this slight difference starts earlier than it did for the constant resistive strip cases. For  $TE_z$  incidence, as Figures 3.18 and 3.19 indicate, the predictions compare very well except for a deviation towards edge-on incidence. For this geometry, close to edge-on the MM solution predicts a smooth decay towards zero. The UTD solution predicts the same thing; however, first it increases a few dB and defines another small sidelobe before the scattering width drops to zero. This may suggest that the multiple order diffractions being used in the UTD formulation (up to third order) are not high enough to predict the scattering behavior close to edge-on for  $TE_z$

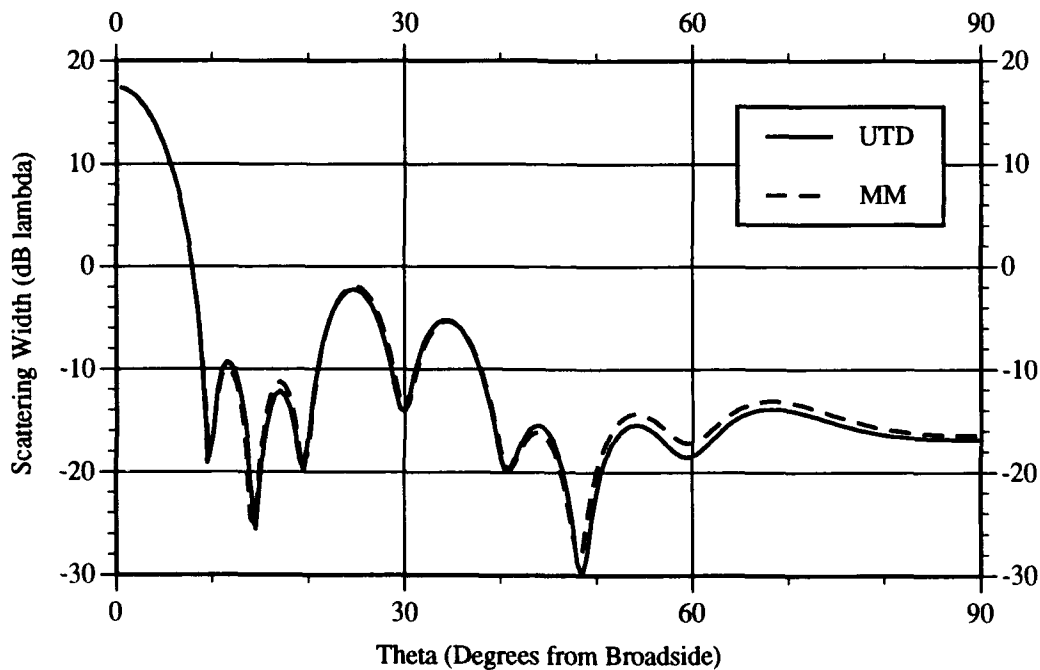


Figure 3.14. Scattering Prediction for a  $2\lambda$  Conducting Strip with  $1\lambda$  Constant Resistive Loads,  $\eta = 0.5$ ,  $TM_z$

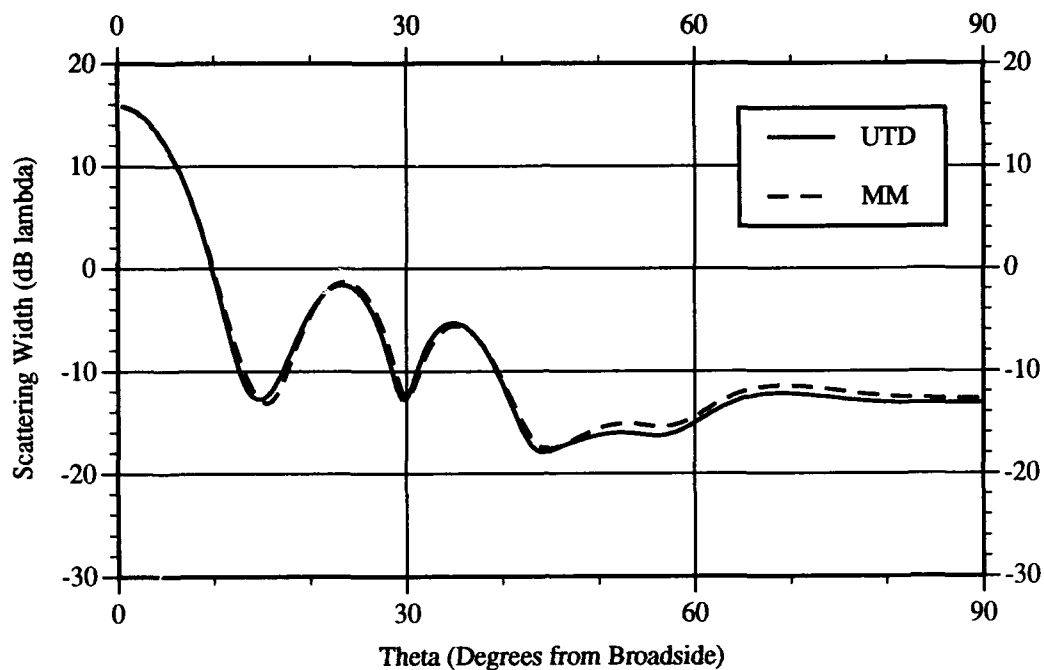


Figure 3.15. Scattering Prediction for a  $2\lambda$  Conducting Strip with  $1\lambda$  Constant Resistive Loads,  $\eta = 1.5$ ,  $TM_z$

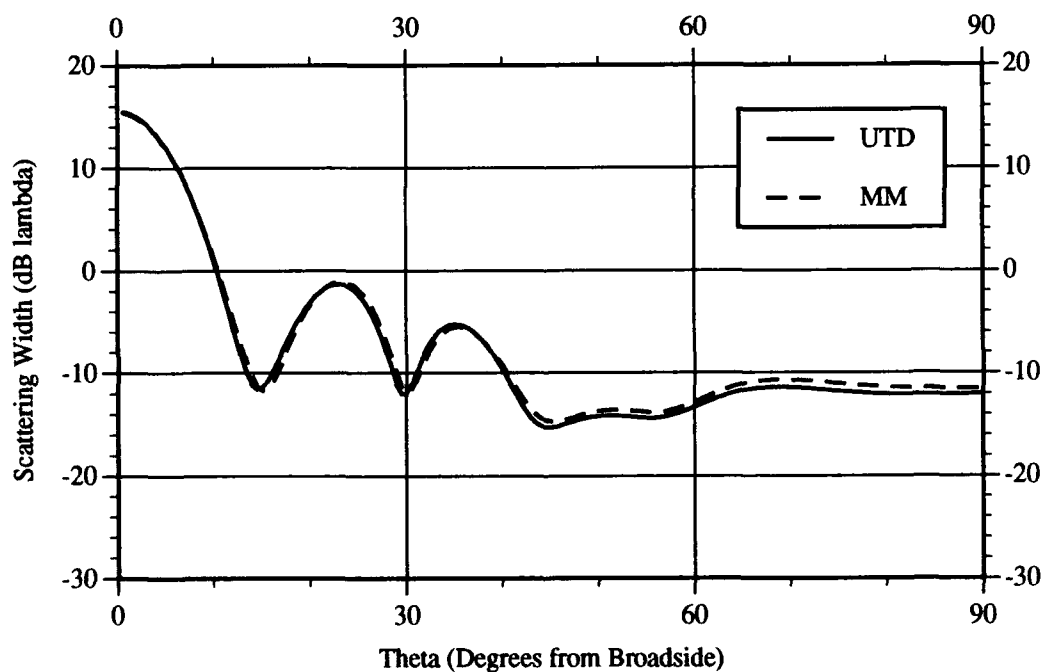


Figure 3.16. Scattering Prediction for a  $2\lambda$  Conducting Strip with  $1\lambda$  Constant Resistive Loads,  $\eta = 2$ ,  $TM_z$

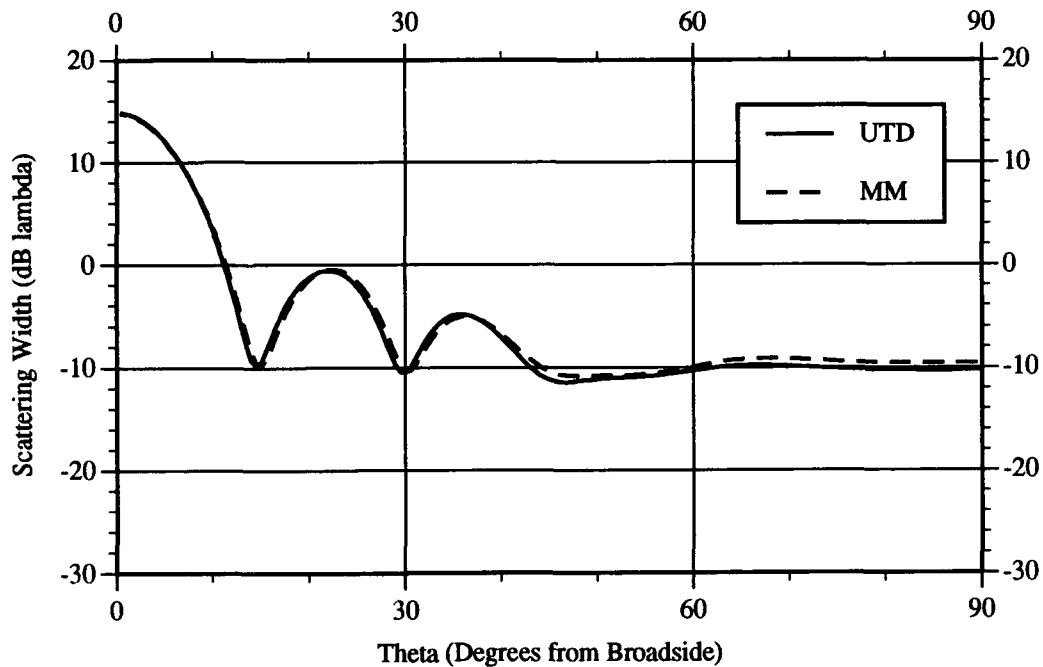


Figure 3.17. Scattering Prediction for a  $2\lambda$  Conducting Strip with  $1\lambda$  Constant Resistive Loads,  $\eta = 4$ ,  $TM_z$

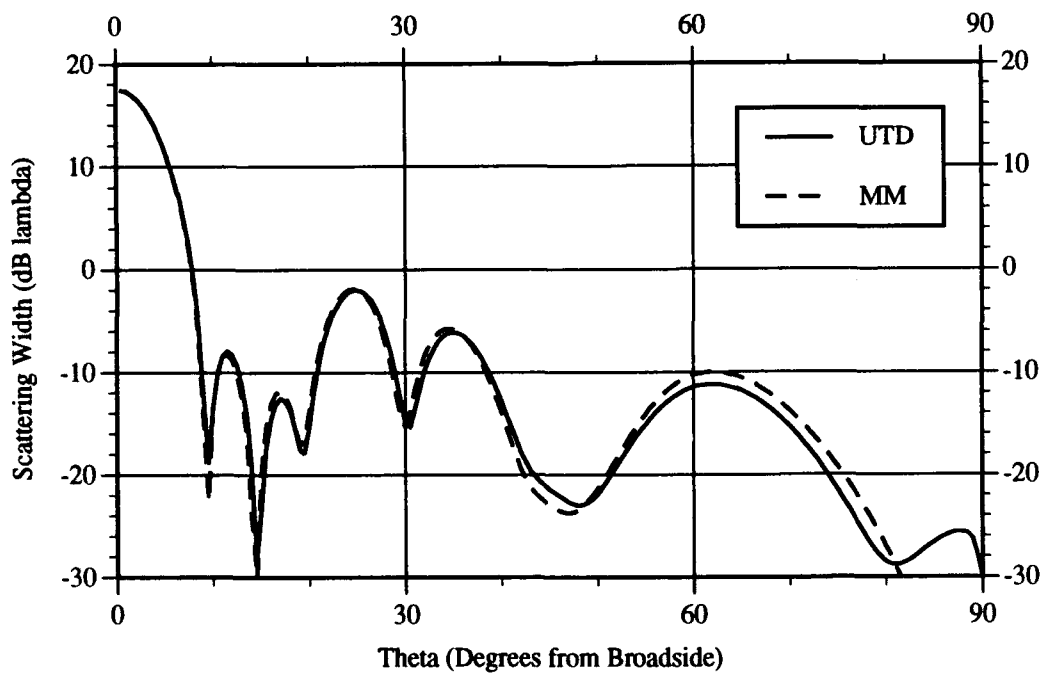


Figure 3.18. Scattering Prediction for a  $2\lambda$  Conducting Strip with  $1\lambda$  Constant Resistive Loads,  $\eta = 0.5$ ,  $TE_z$

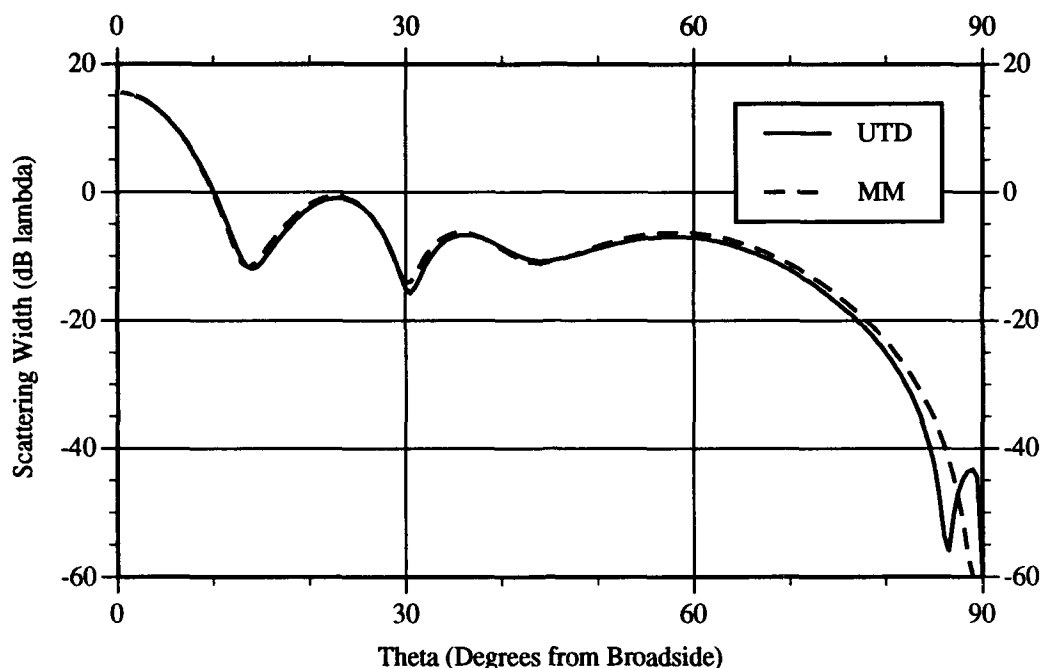


Figure 3.19. Scattering Prediction for a  $2\lambda$  Conducting Strip with  $1\lambda$  Constant Resistive Loads,  $\eta = 2$ ,  $TE_z$

incidence. Thus, it appears that the accuracy of the formulation depends on the polarization especially near grazing incidence. In any event, accuracy to within a few dB for the near edge-on scattering width is not as important for  $TE_z$  as it is for  $TM_z$  polarization, since the scattering width is approaching zero near edge-on in the  $TE_z$  case.

**Tapered Resistive Strips.** Scattering predictions for a variety of  $4\lambda$  tapered resistive strips are presented in Figures 3.20 through 3.25. The resistive tapers considered here are  $|x|^b$ , where  $b$  is an integer. The strip geometry is symmetrical as shown in Figure 3.2.c. As Figure 3.20 shows, the comparison between the UTD prediction and MM prediction is very good up to about  $60^\circ$  from broadside for a taper of  $\eta = |x|$ . From this point on the difference between the predictions increases to about 3 dB at edge-on. As the constant  $b$  increases, the edge-on difference increases also. In Figure 3.21, for an  $x^2$  resistive taper, the edge-on difference has increased to about 4.5 dB. For the resistive



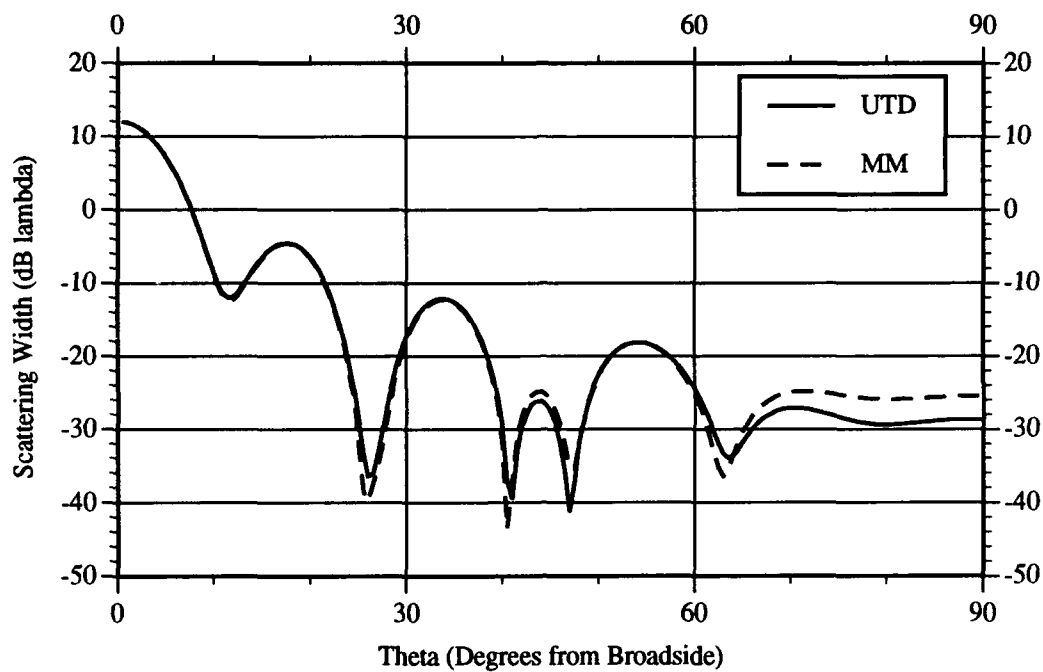


Figure 3.20. Scattering Prediction for a  $4\lambda$  Tapered Resistive Strip,  $\eta = |x|$ ,  $TM_z$

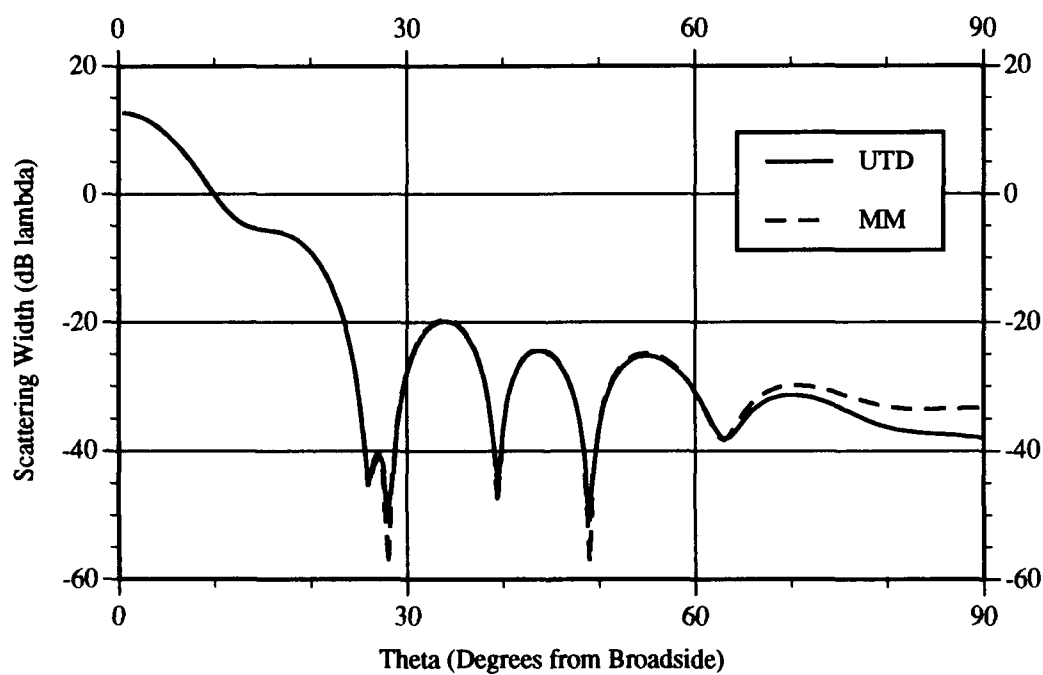


Figure 3.21. Scattering Prediction for a  $4\lambda$  Tapered Resistive Strip,  $\eta = x^2$ ,  $TM_z$

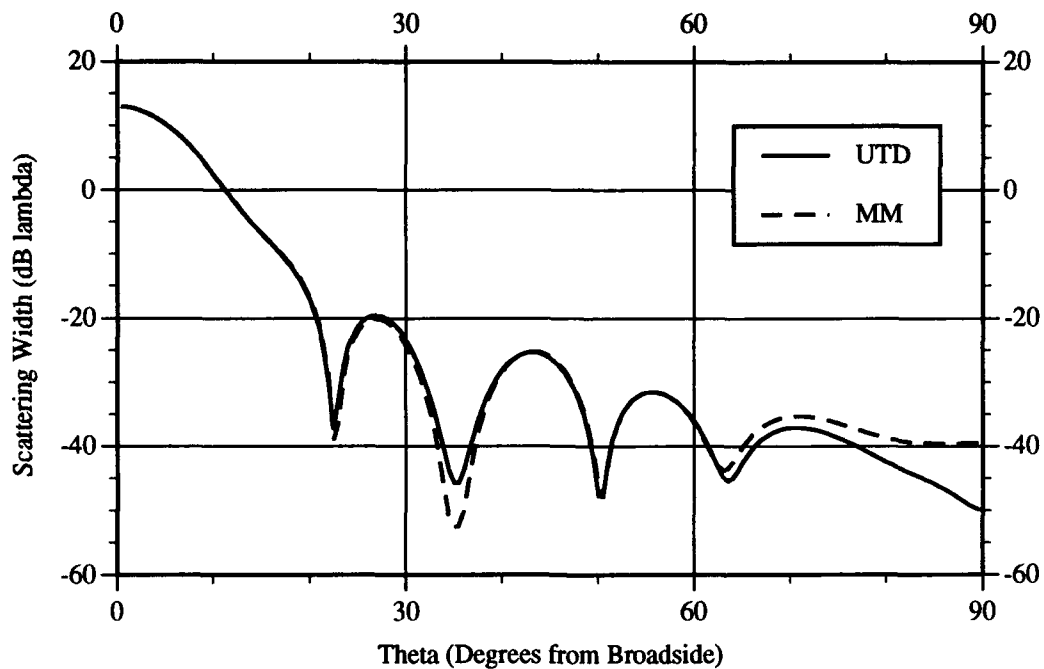


Figure 3.22. Scattering Prediction for a  $4\lambda$  Tapered Resistive Strip,  $\eta = |x|^3$ ,  $TM_z$

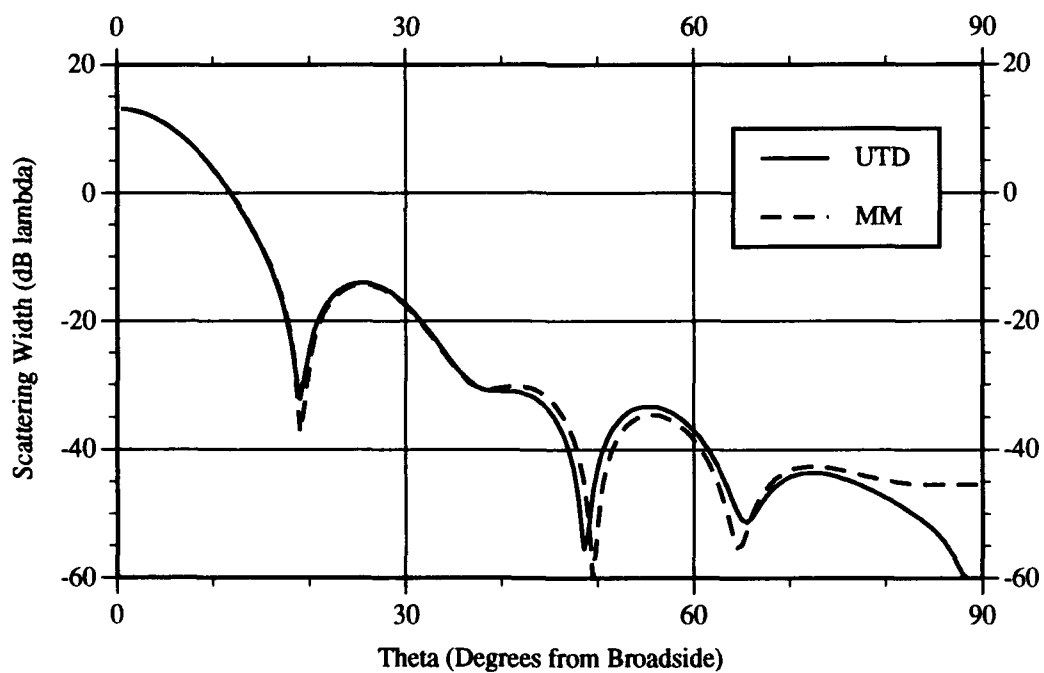


Figure 3.23. Scattering Prediction for a  $4\lambda$  Tapered Resistive Strip,  $\eta = x^4$ ,  $TM_z$

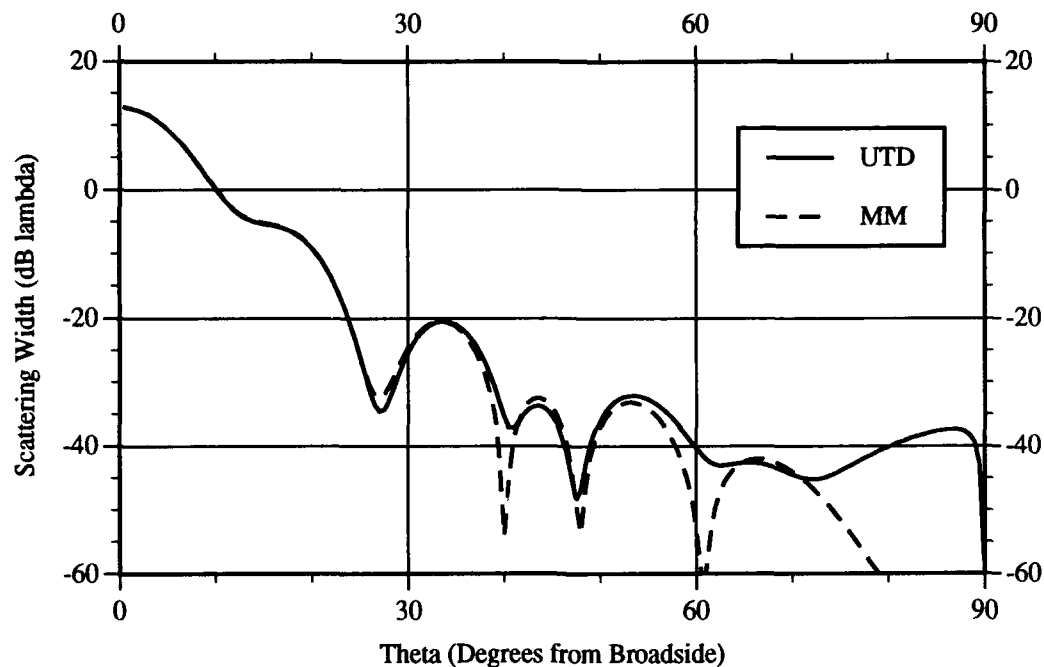


Figure 3.24. Scattering Prediction for a  $4\lambda$  Tapered Resistive Strip,  $\eta = x^2$ ,  $TE_z$

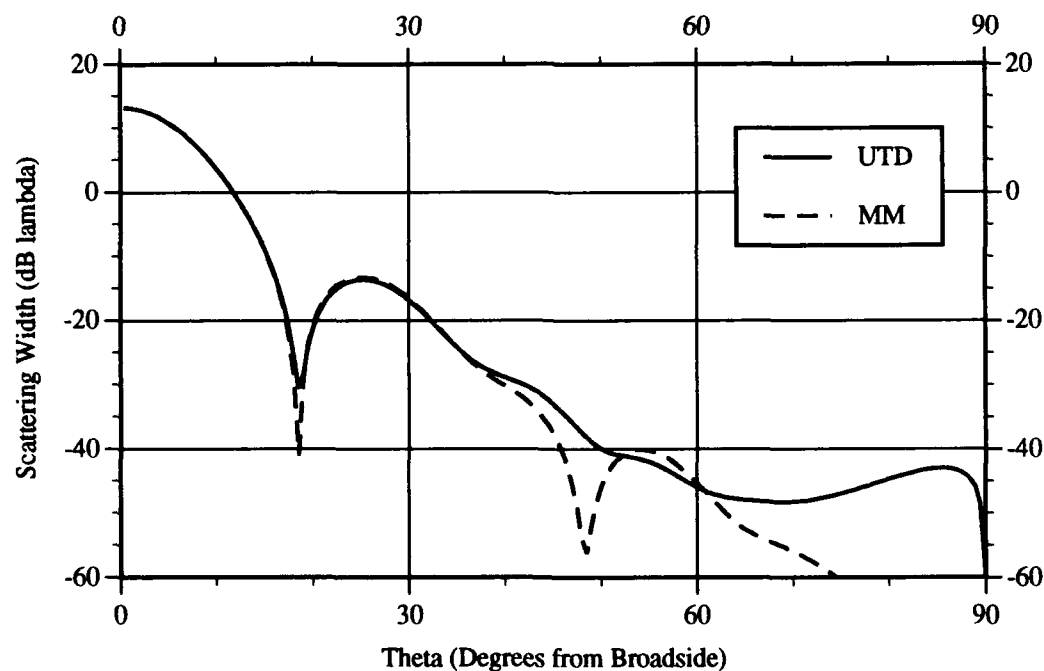


Figure 3.25. Scattering Prediction for a  $4\lambda$  Tapered Resistive Strip,  $\eta = x^4$ ,  $TE_z$

tapers of  $|x|^3$  and  $x^4$ , shown in Figures 3.22 and 3.23, the edge-on difference has increased to approximately 10 dB and 15 dB, respectively. Note, however, that the edge-on scattering width is decreasing greatly as  $b$  increases. For angles close to edge-on, higher order diffractions have an increasing contribution to the scattering pattern. Since the UTD prediction only includes up to third order diffractions, some deviation is to be expected. The deviation increases with  $b$  because the discrete strips that model the taper become more discontinuous with each other. This increases the amount of interactions that can exist between the discrete strips. For example, based on the modelling scheme shown in Figure 3.5, the  $|x|$  resistive taper starts at  $\eta = 0.05$  and ends at  $\eta = 1.95$ . The  $x^4$  resistive taper starts at  $\eta = 0.00000625$  and ends at  $\eta = 14.46$ . For the  $x^4$  resistive taper, diffractions higher than the third order may start contributing significantly to the scattering pattern towards edge-on. Excellent agreement still occurs in Figures 3.20 through 3.23 to just past  $60^\circ$  from broadside. For the  $TE_z$  cases shown in Figures 3.24 and 3.25 large variations between the predictions occur close to edge-on. The UTD prediction comes back up several dB before it goes to zero like the MM prediction. Also, as the polynomial increases to degree four the predictions agree to only just past  $30^\circ$  from broadside. Again, the discontinuities between the discrete resistive strips that model the tapers require higher order diffractions than third order to model the edge-on scattering.

Tapered Resistive-Loaded Conducting Strips. Figures 3.26 through 3.31 show the scattering predictions for several tapered resistive-loaded conducting strips. Each of the strips has a  $2\lambda$  conducting strip in the center with  $1\lambda$  tapered resistive loads. The loads specified are  $(|x| - 1)^b$ , where  $b$  is an increasing integer. Since the loads are only  $1\lambda$  wide, ideally, the resistance at the ends of the strips is  $\eta = 1$  for all the different degrees of polynomials. However, the shapes of the resistive tapers differ per the degree of the polynomial as shown in Figure 3.32. Because of the discrete modelling, the last resistance will vary per the degree of the polynomial. For ten segments per wavelength, the last

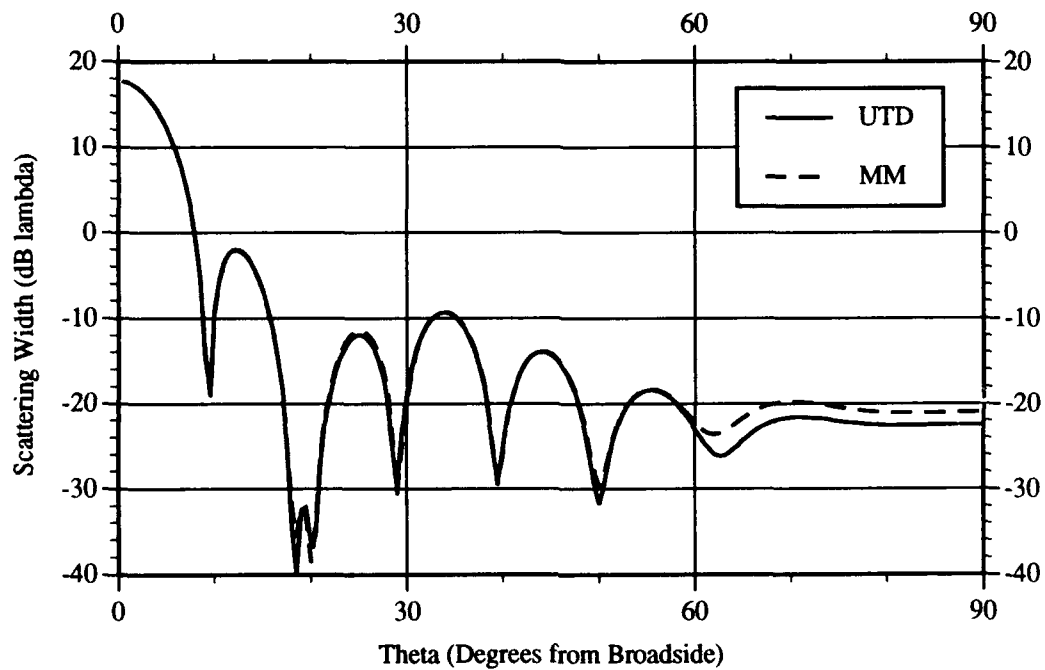


Figure 3.26. Scattering Prediction for a  $2\lambda$  Conducting Strip with  $1\lambda$  Tapered Resistive Loads,  $\eta = |x| - 1$ ,  $TM_z$

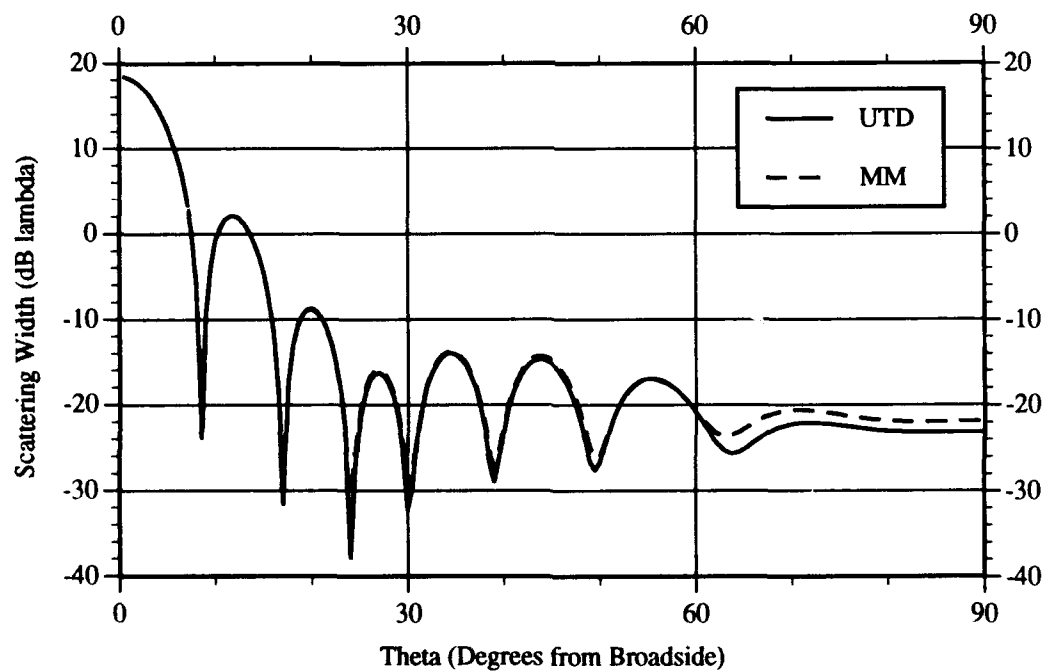


Figure 3.27. Scattering Prediction for a  $2\lambda$  Conducting Strip with  $1\lambda$  Tapered Resistive Loads,  $\eta = (|x| - 1)^2$ ,  $TM_z$

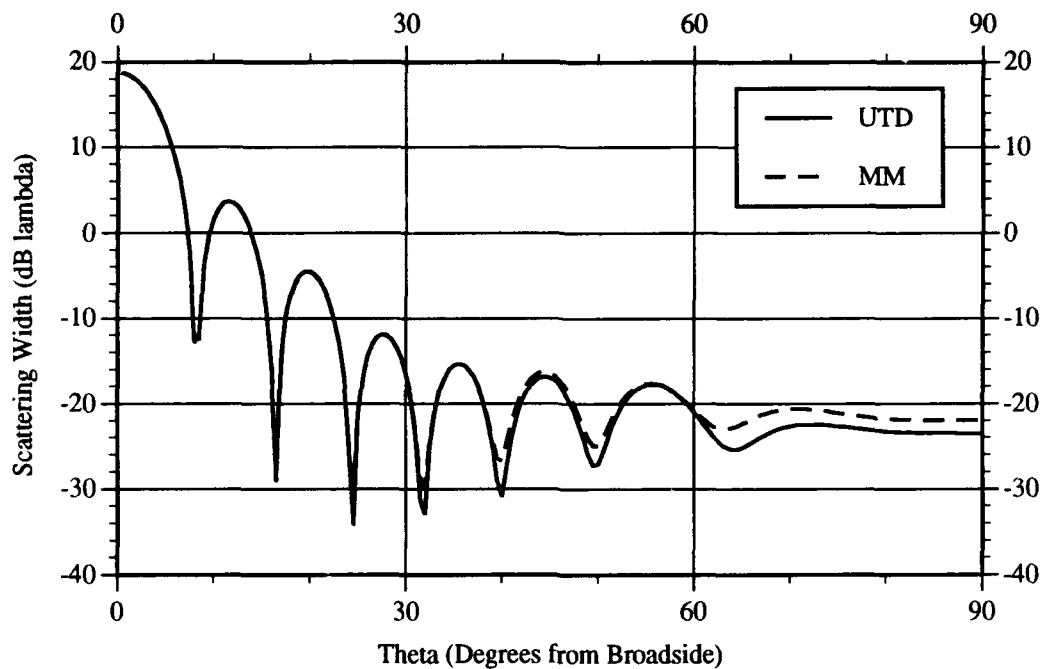


Figure 3.28. Scattering Prediction for a  $2\lambda$  Conducting Strip with  $1\lambda$  Tapered Resistive Loads,  $\eta = (|x| - 1)^3$ ,  $TM_z$

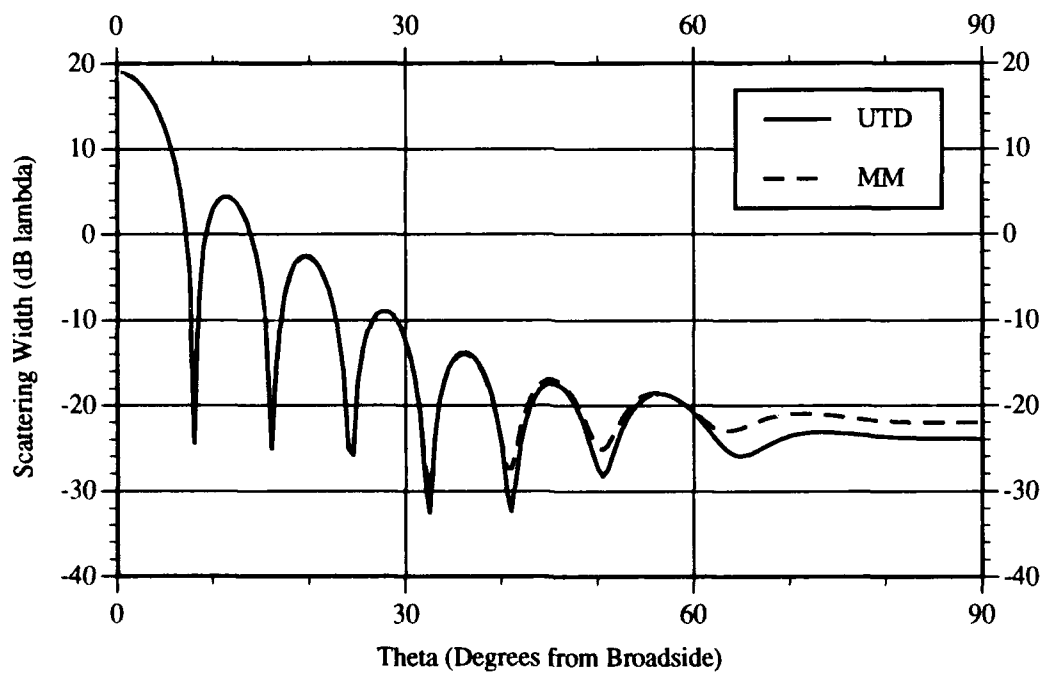


Figure 3.29. Scattering Prediction for a  $2\lambda$  Conducting Strip with  $1\lambda$  Tapered Resistive Loads,  $\eta = (|x| - 1)^4$ ,  $TM_z$

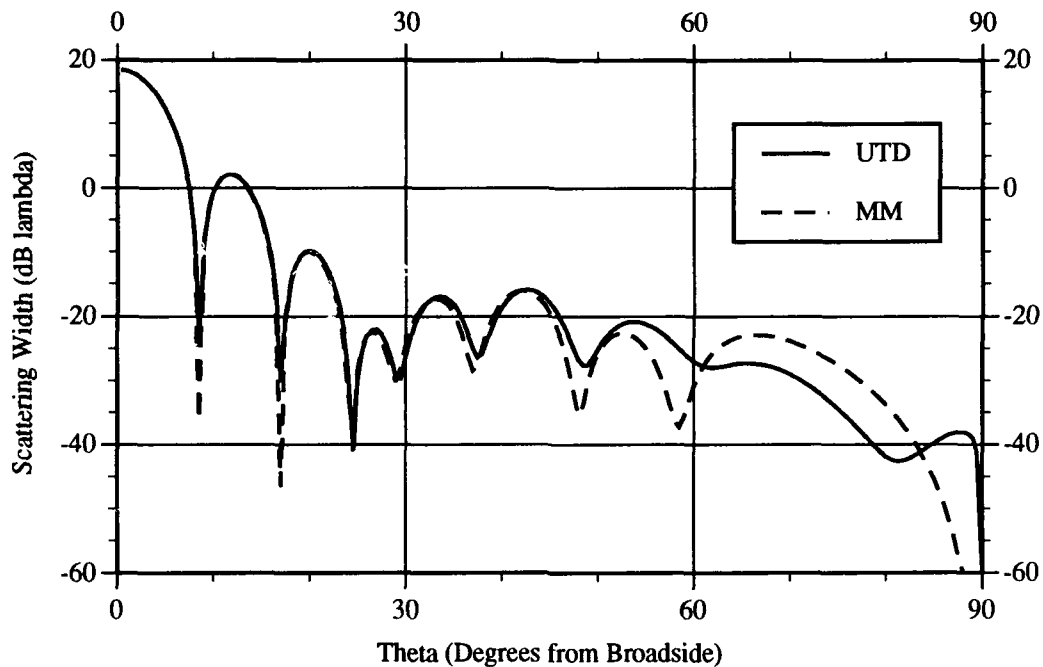


Figure 3.30. Scattering Prediction for a  $2\lambda$  Conducting Strip with  $1\lambda$  Tapered Resistive Loads,  $\eta = (|x| - 1)^2$ ,  $TE_z$

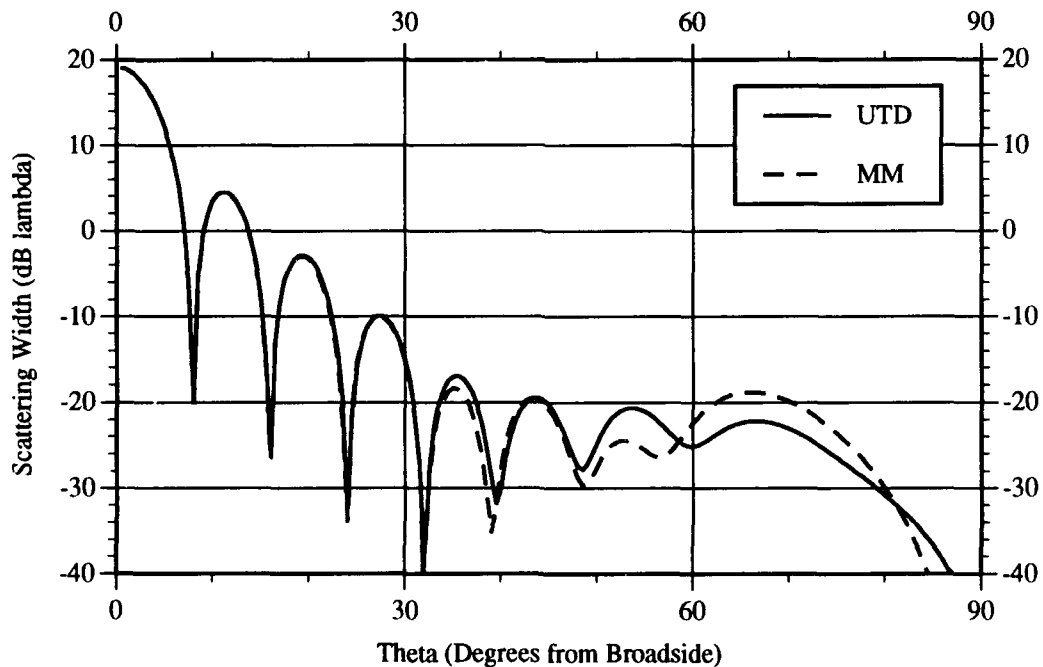


Figure 3.31. Scattering Prediction for a  $2\lambda$  Conducting Strip with  $1\lambda$  Tapered Resistive Loads,  $\eta = (|x| - 1)^4$ ,  $TE_z$

resistive discrete strip is  $(0.95)^b$ . The moment method code used the same discrete strip modeling; thus, comparisons were valid. As Figures 3.26 through 3.29 indicate, for  $TM_z$  with  $b$  increasing from 1 to 4, the predictions agree almost perfectly to just past  $60^\circ$  from broadside. Up to edge-on the difference is approximately 2 dB. Thus, even though the discontinuities between the discrete resistive strips differ depending on the degree of the polynomial, the multiple diffractions being used are sufficient to predict the scattering pattern. For the  $TE_z$  cases presented in Figures 3.30 and 3.31, differences between the predictions start occurring sooner at about  $45^\circ$  from broadside. Note that the UTD prediction in Figure 3.30 displays the same odd behavior near edge-on incidence as described previously.

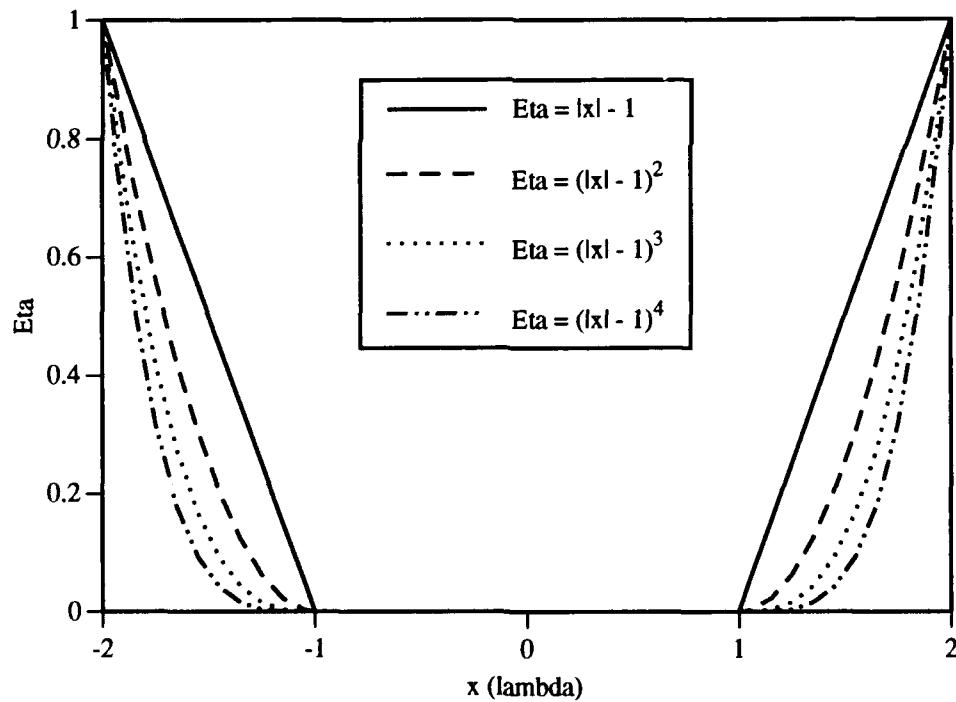


Figure 3.32. Tapered Resistive-Loaded Conducting Strip Comparison,  
 $b = 1, 2, 3, 4$



Measurements. Measurements were conducted at the AFIT School of Engineering's RCS measurement chamber. Measurements were performed on a conducting strip, constant resistive strips, constant resistive-loaded conducting strips, tapered resistive strips, and tapered resistive-loaded conducting strips. The chamber used is a far-field measurement facility with separate receive and transmit horn antennas. The antennas can be rotated for  $TM_z$  (E) or  $TE_z$  (H) polarization. Targets are set on an ogive pedestal approximately 27 feet from the horn antennas. All strips measured were 4 in by 6 in (total); the illuminating frequency was 11.8 GHz. The frequency was set to this particular number so one wavelength equaled 1 in. Thus, the strips were  $4\lambda$  wide and  $6\lambda$  long. All loaded conducting strips had a center conductor that was 2 in wide. Because the scattering predictions were made for infinitely long strips that were  $4\lambda$  wide, the three-dimensional RCS measured in the chamber had to be converted to two-dimensional scattering width. This conversion is defined in (1:578) as:

$$\sigma_{2D}(dbm) \equiv \sigma_{3D}(dbsm) \frac{\lambda}{2l^2} \quad (3.6)$$

where  $\lambda$  is the wavelength and  $l$  is the length of the strip. Substituting  $\lambda = 1$  in (0.0254 m) and  $l = 6$  in (0.1524 m) into Eq 3.6, converting  $\sigma_{2D}$  (dBm) to  $\sigma_{2D}$  (dB $\lambda$ ), and changing the equation for dB values yields:

$$\sigma_{2D}(dB\lambda) = \sigma_{3D}(dBsm) + 13.33 \quad (3.7)$$

Thus, measurements made in the chamber were converted to the same units as the predictions for comparison in overlay plots.

Resistive Materials. Emerson and Cuming supplied two types of constant resistive material used to construct various strips. Eccosorb SC 100 is a graphite impregnated cloth with a specified surface resistance of 100  $\Omega$ /sq. Eccosorb VF is a

flexible conductive plastic film available in several surface resistances. VF 10, VF 20, and VF 30, with specified surface resistances of 377, 200, and 130  $\Omega/\text{sq}$  respectively, were used. Sheldahl provided a 1 in wide tapered R-card. The surface resistance varies from 5  $\Omega/\text{sq}$  on one edge to 1500  $\Omega/\text{sq}$  on the other edge. The R-card was constructed by Sheldahl by sputtering nichrome onto a Kapton substrate. It was used to construct a tapered resistive-loaded conducting strip.

Waveguide measurements at 11.8 GHz revealed that the VF material exhibited different resistances than specified. Heaton (3) discovered this while constructing strips from the SC 100 and VF 10 material. The waveguide measurements were conducted on the VF material using the procedures outlined in (3:5.2-5.4). The following table lists the specified and measured resistive values, as well as the thicknesses of the SC and VF materials used to construct the various strip geometries. The SC 100 measurement was obtained from (3). Performing measurements on the Sheldahl taper was beyond the scope of this thesis.

TABLE 3.1  
MATERIAL PARAMETERS

TYPE	SPECIFIED RESISTANCE ( $\Omega$ )	MEASURED RESISTANCE ( $\Omega$ )	THICKNESS (mils)
SC 100	100	$180 + 96.1j$	10
VF 10	377	$129 + 21.5j$	10
VF 20	200	$96.2 + 64.0j$	20
VF 30	130	$77.4 + 104j$	30

As Table 3.1 indicates, both the SC and VF materials exhibit an imaginary resistive component. Also, for the VF material the real part of the measured resistance decreases from VF 10 to VF 30 as it does for the specified values. However, the imaginary part of the measured resistance increases from VF 10 to VF 30 as the material gets thicker. The computer code used to predict the scattered patterns was developed for just real resistances; thus, a decision was made to use just the real part of the resistances in the comparison of scattering predictions to measurements. Although, this approach discounted the imaginary parts' contribution to the scattering patterns, it was found that using just the real part resulted in excellent comparisons.

#### Target Preparation.

Each of the materials listed in Table 3.1 were used to construct 4 in by 6 in constant resistive strips. Figures 3.33 through 3.38 show the remaining construction geometries for constant resistive-loaded conducting strips, tapered resistive strips, and tapered resistive-loaded conducting strips. As Figure 3.33 shows, for constant resistive-loaded conducting strips, just the SC 100 and VF 10 were used. These were constructed by sandwiching a 4 in by 6 in resistive strip between two 2 in conducting strips. Figures 3.34 through 3.37 show how the three different kinds of VF material were used to construct tapered resistive strips and tapered resistive-loaded conducting strips. Each successive discrete resistive strip from the center had a larger resistance. The tapered resistive-loaded conducting strips in Figures 3.36 and 3.37 were constructed by sandwiching a large piece of the innermost resistive load between two 2 in by 6 in conducting strips. The Sheldahl taper was used to construct a tapered resistive-loaded conducting strip as shown in Figure 3.38. Flashbreaker tape, a low RCS material, was used to hold the materials in place for all constructions.

Several styrofoam cut-off cone frustrum mounts were fabricated for the different strip geometries. This shape was selected because it was symmetrical and the slant of the

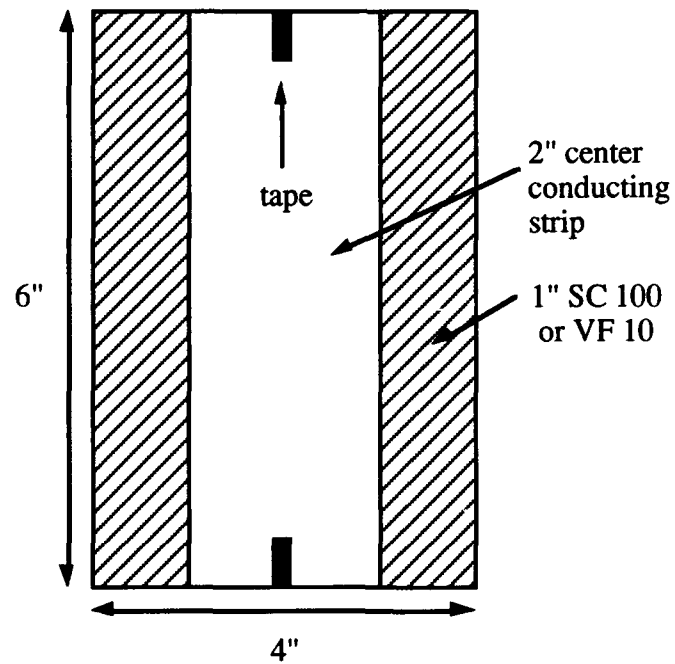


Figure 3.33. Constant Resistive-Loaded Strip  
Constructed of SC 100 or VF 10

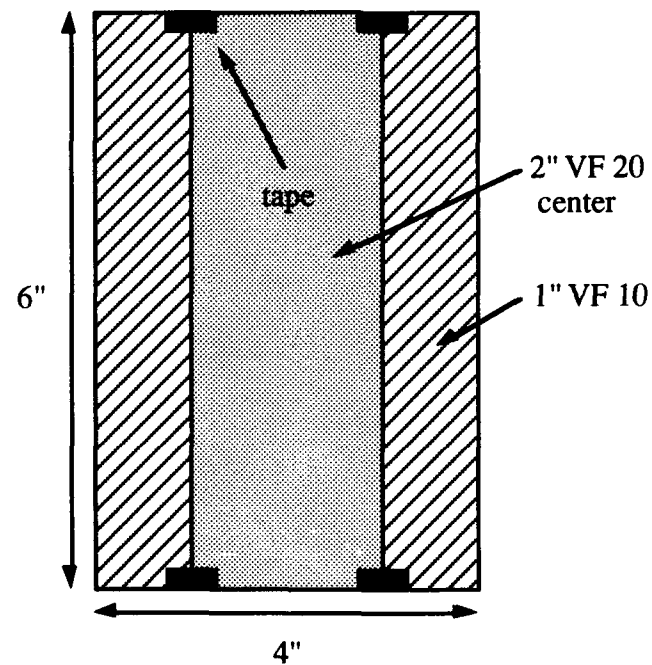


Figure 3.34. Tapered Resistive Strip Constructed  
with VF 10 and VF 20

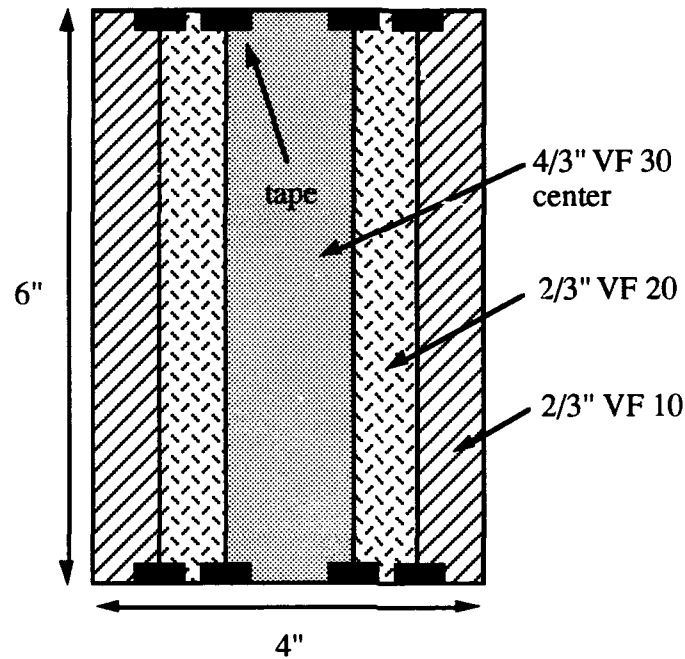


Figure 3.35. Tapered Resistive Strip Constructed with VF 10, VF 20, and VF 30

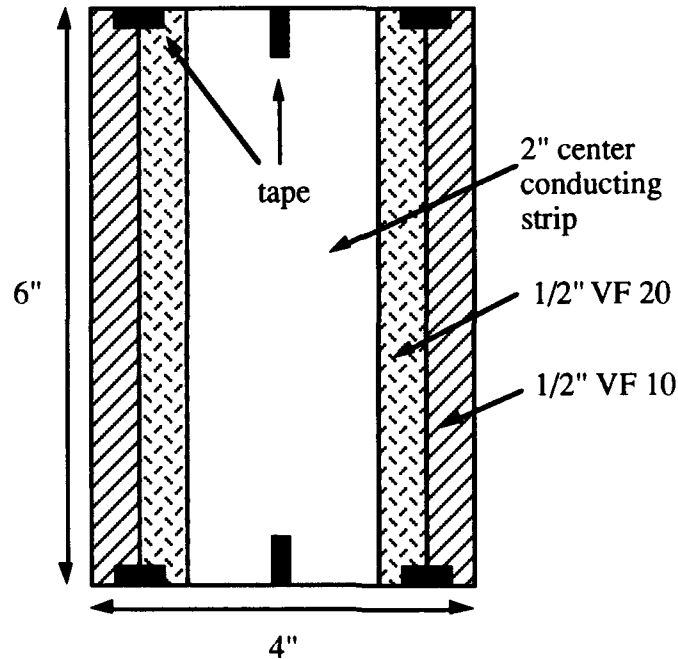


Figure 3.36. Tapered Resistive-Loaded Conducting Strip Constructed with VF 10 and VF 20

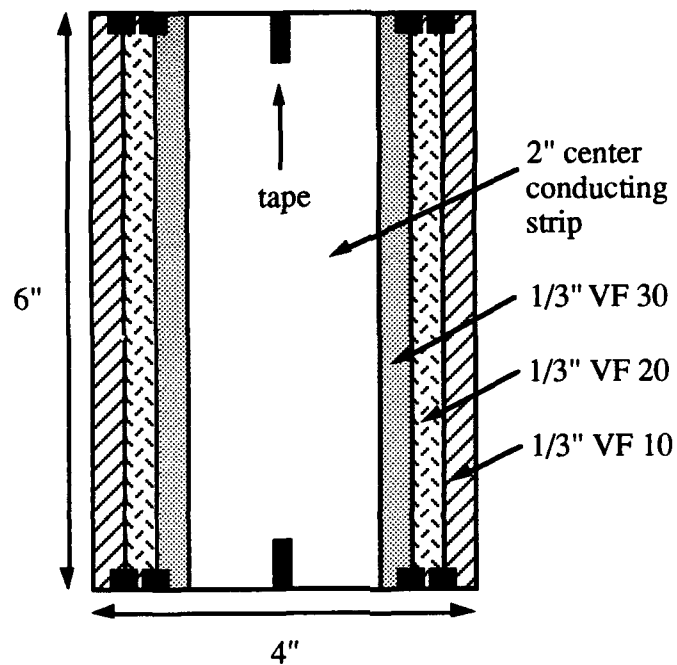


Figure 3.37. Tapered Resistive-Loaded Conducting Strip Constructed with VF 10, VF 20, and VF 30

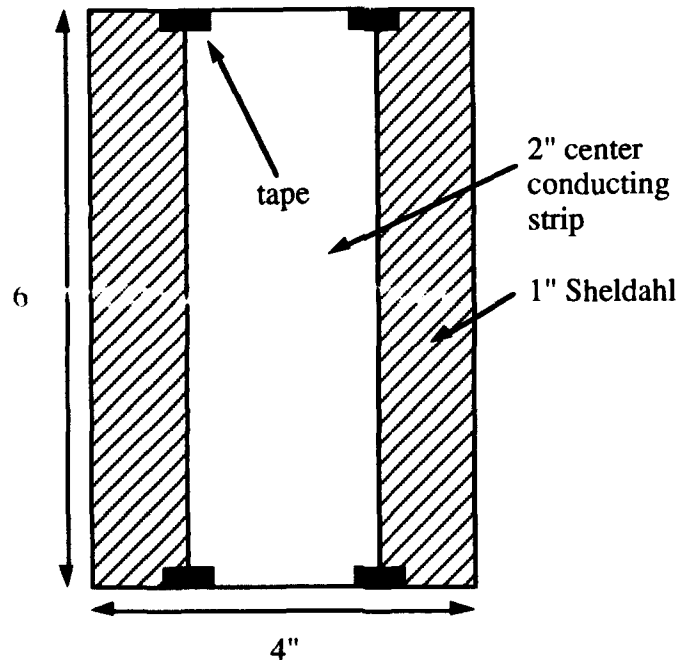


Figure 3.38. Tapered Resistive-Loaded Conducting Strip Constructed with a Sheldahl Taper

cone would reduce energy scattered back to the receiver antenna from the mount. Also, this type of mount can be subtracted from the measurements as a separate target background. As Figure 3.39 shows, the cut-off cones were sliced in half lengthwise so the strip could be placed inside. Then, the two halves were held together with flashbreaker tape and placed on a styrofoam base for rotation of the azimuth scan. For the 4 in by 6 in conducting and VF 30 strips, a cut-off cone was fabricated with an equivalent cavity to accommodate the thickness of the strips. The other constant resistive strips were thin enough for a cut-off cone without any cavity. For the resistive-loaded conducting strips a cut-off cone was used that had a 2 in by 6 in cavity to accommodate the thickness of the center conductor. The tapered resistive strips used the cut-off cone without a cavity. Target background subtraction was accomplished with a solid cut-off cone.

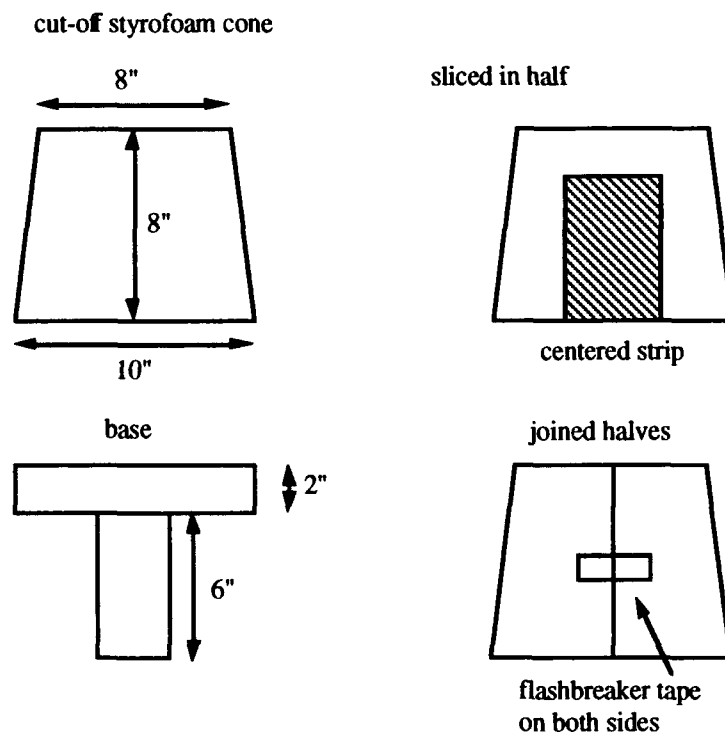


Figure 3.39. Styrofoam Mount Construction

Table 3.2 summarizes the measurements to be presented. In the measurement column CS stands for conducting strip, RS stands for constant resistive strip, TRS stands for tapered resistive strip, LS stands for constant resistive-loaded conducting strip, and TLS stands for tapered resistive-loaded conducting strip. E and H stands for E polarization ( $TM_z$ ) and H polarization ( $TE_z$ ), respectively.

TABLE 3.2  
MEASUREMENTS

MEASUREMENT	CONDUCTING STRIP WIDTH ( $\lambda$ )	RESISTIVE STRIP OR LOAD WIDTH ( $\lambda$ )	GEOMETRY ( $\lambda$ )	FIGURE NUMBER
CSE	4	N/A	4	3.40
CSH	4	N/A	4	3.41
RS/SC100E	N/A	4	4	3.42
RS/SC100H	N/A	4	4	3.43
RS/VF10E	N/A	4	4	3.44
RS/VF10H	N/A	4	4	3.45
RS/VF20E	N/A	4	4	3.46
RS/VF20H	N/A	4	4	3.47
RS/VF30E	N/A	4	4	3.48
RS/VF30H	N/A	4	4	3.49



LS/SC100E	2	1	SC100/CS/SC100 1/2/1	3.50
LS/SC100H	2	1	SC100/CS/SC100 1/2/1	3.51
LS/VF10E	2	1	VF10/CS/VF10 1/2/1	3.52
LS/VF10H	2	1	VF10/CS/VF10 1/2/1	3.53
TRS/VF10/20E	N/A	4	VF10/VF20/VF10 1/2/1	3.54
TRS/VF10/20H	N/A	4	VF10/VF20/VF10 1/2/1	3.55
TRS/VF10/20/30E	N/A	4	VF10/VF20/VF30/VF20/VF10 .67/.67/1.33/.67/.67	3.56
TRS/VF10/20/30H	N/A	4	VF10/VF20/VF30/VF20/VF10 .67/.67/1.33/.67/.67	3.57
TLS/VF10/20E	2	1	VF10/VF20/CS/VF20/VF10 .5/.5/2/.5/.5	3.58
TLS/VF10/20H	2	1	VF10/VF20/CS/VF20/VF10 .5/.5/2/.5/.5	3.59
TLS/VF10/20/30E	2	1	VF10/VF20/VF30/CS /VF30/VF20/VF10 .33/.33/.33/2/.33/.33/.33	3.60
TLS/VF10/20/30H	2	1	VF10/VF20/VF30/CS /VF30/VF20/VF10 .33/.33/.33/2/.33/.33/.33	3.61
TLS/SHEL/E	2	1	SHEL/CS/SHEL 1/2/1	3.62

Constant Resistive Strips. Scattering width predictions of strips with constant resistance are compared to measurements in Figures 3.40 through 3.49. Figures 3.40 and 3.41 show the excellent agreement between predictions and measurements for a conducting strip ( $\eta = 0$ ) with  $TM_z$  and  $TE_z$  polarization, respectively. For  $TM_z$  polarization the only deviation that bears notice is at approximately  $65^\circ$ . The measured sidelobe is about 2 dB higher than the prediction. The edge-on scattering difference is just above 0.5 dB. For  $TE_z$  polarization, there are deviations between the lobing structure at approximately  $35^\circ$  and  $55^\circ$ . These deviations could be due to interactions between the target and pedestal (3:5.14). Figures 3.42 and 3.43 show the comparison for the SC 100 material. For  $TM_z$  polarization the entire prediction scattering pattern seems to be between 1 dB and 2 dB higher than the measurement. This could be due to just using the real part of the resistance in the prediction and neglecting the imaginary part. As Table 3.1 shows, the SC 100 material has a proportionally large imaginary component. Additionally, the offset

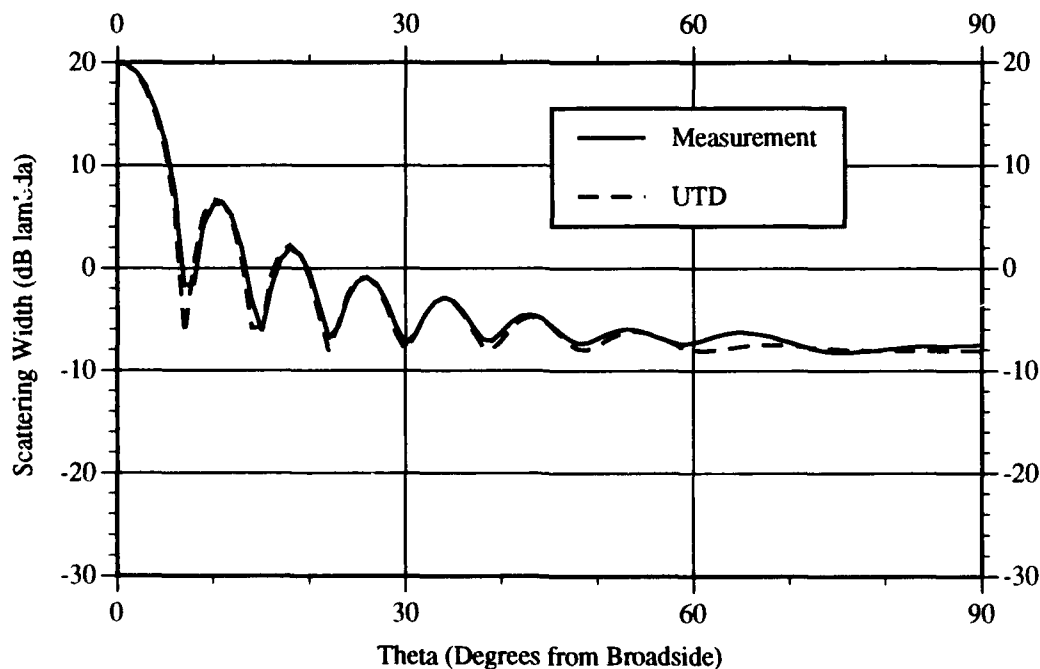


Figure 3.40. Scattering Measurement and Prediction for a  $4\lambda$  Conducting Strip,  $TM_z$

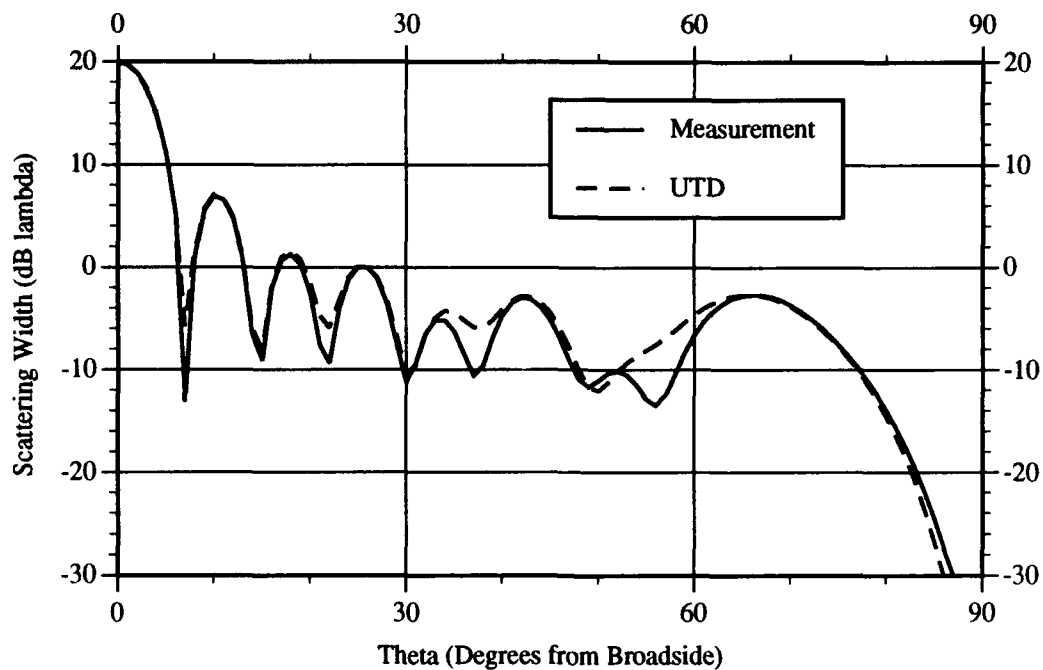


Figure 3.41. Scattering Measurement and Prediction for a  $4\lambda$  Conducting Strip,  $TE_z$

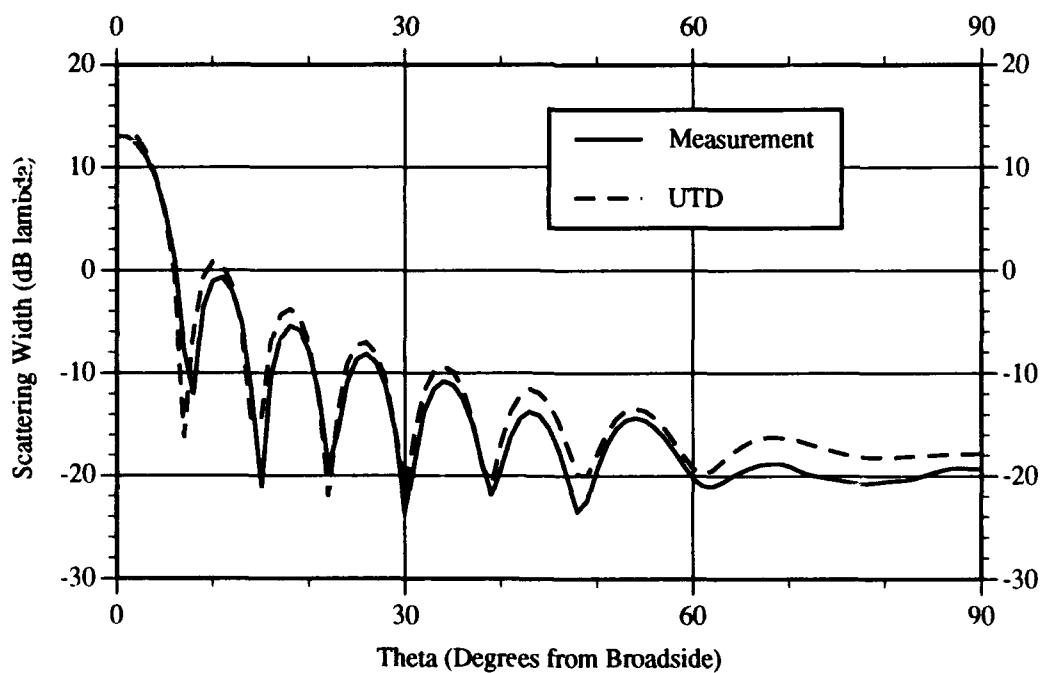


Figure 3.42. Scattering Measurement and Prediction for a  $4\lambda$  Constant Resistive Strip, SC 100,  $TM_z$

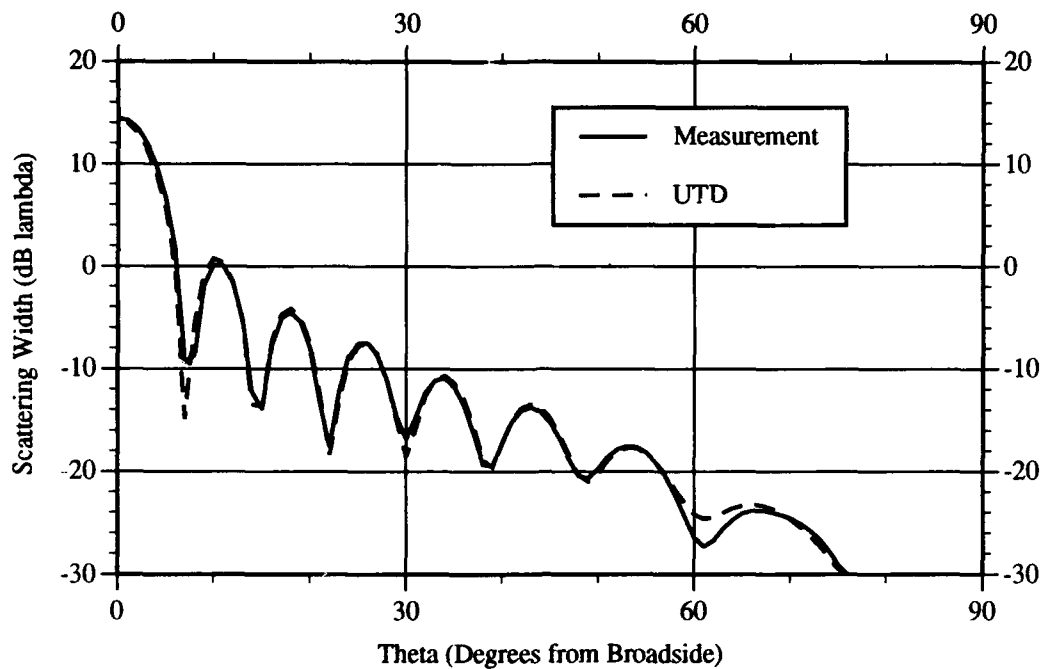


Figure 3.43. Scattering Measurement and Prediction for a  $4\lambda$  Constant Resistive Strip, SC 100,  $TE_z$

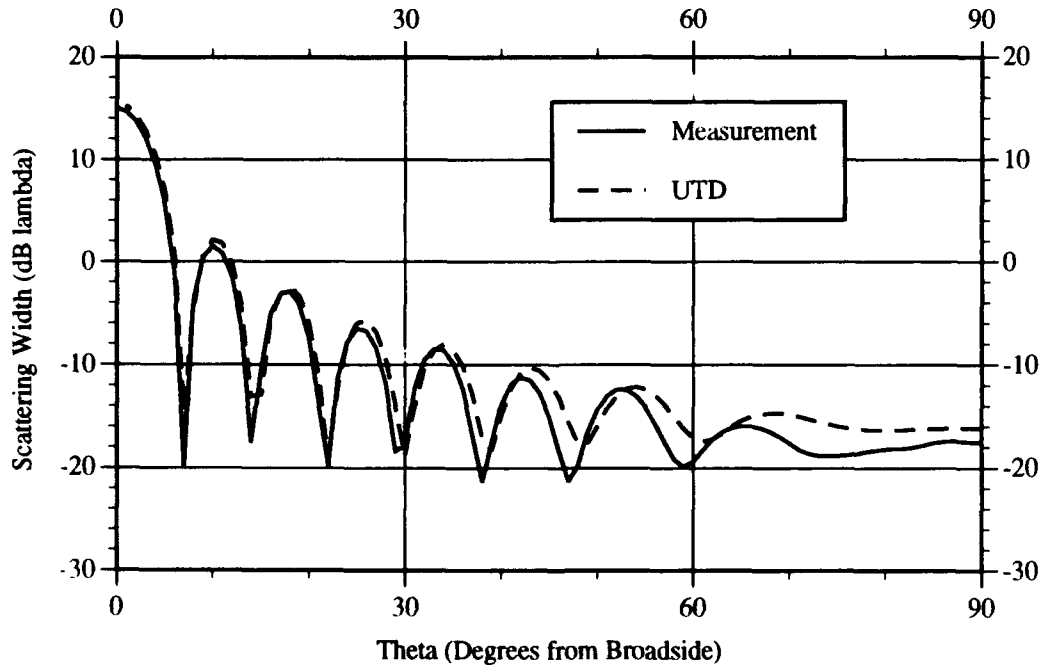


Figure 3.44. Scattering Measurement and Prediction for a  $4\lambda$  Constant Resistive Strip, VF 10,  $TM_z$

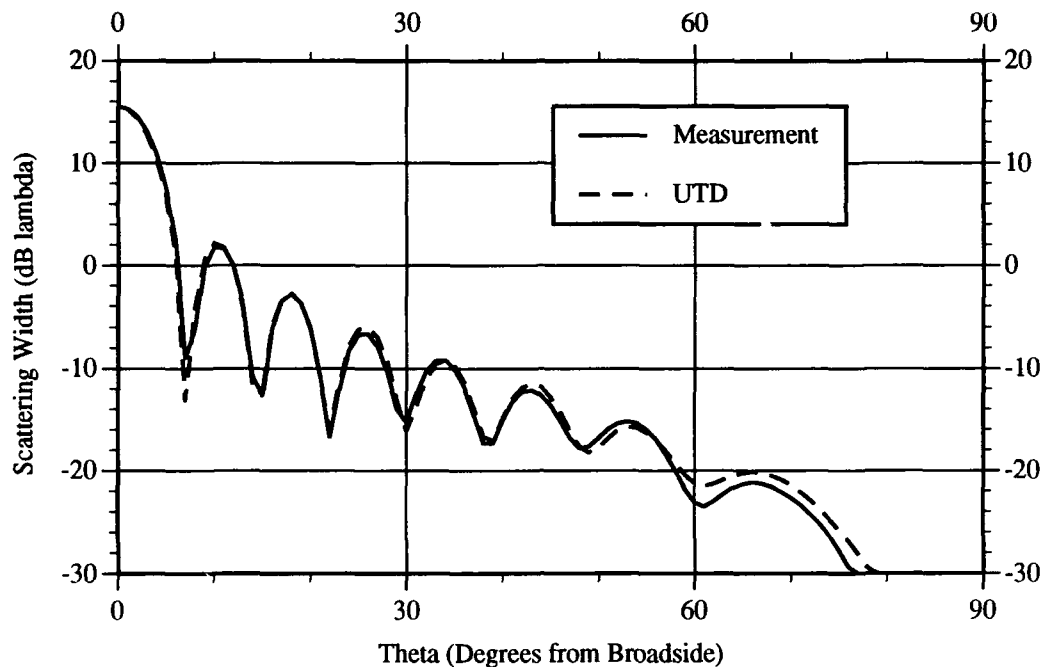


Figure 3.45. Scattering Measurement and Prediction for a  $4\lambda$  Constant Resistive Strip, VF 10,  $TE_z$

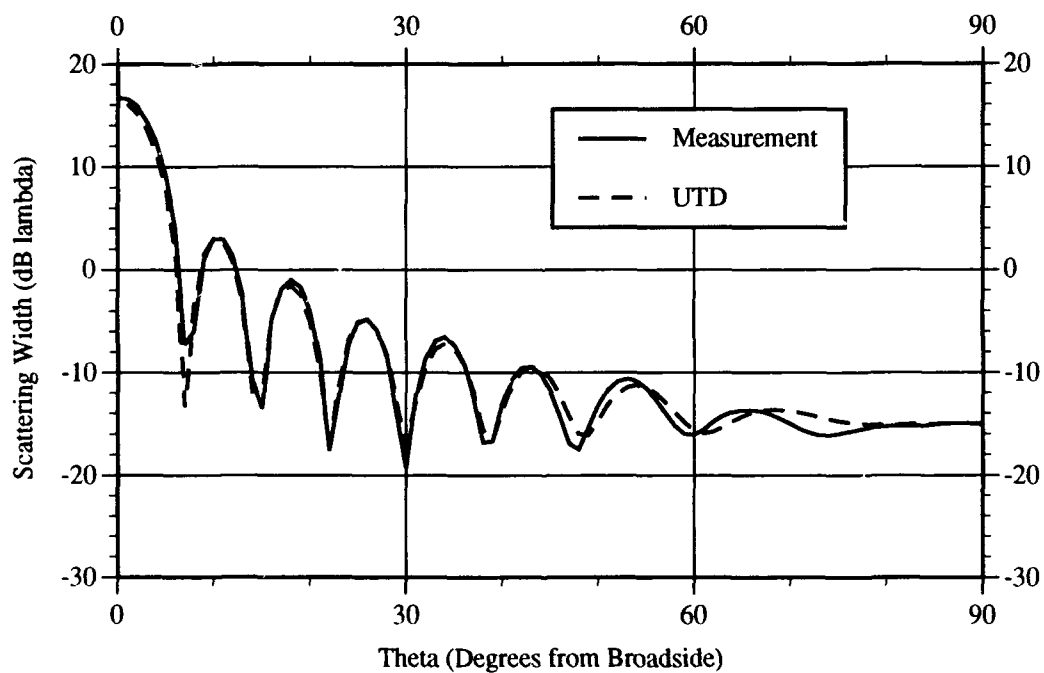


Figure 3.46. Scattering Measurement and Prediction for a  $4\lambda$  Constant Resistive Strip, VF 20,  $TM_z$

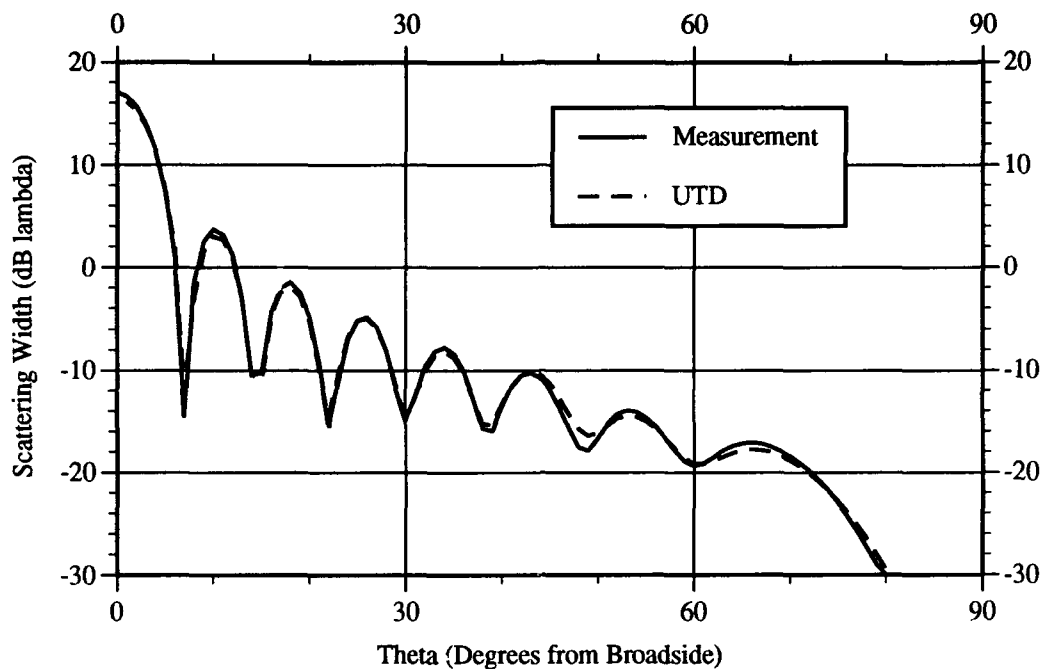


Figure 3.47. Scattering Measurement and Prediction for a  $4\lambda$  Constant Resistive Strip, VF 20,  $TE_z$

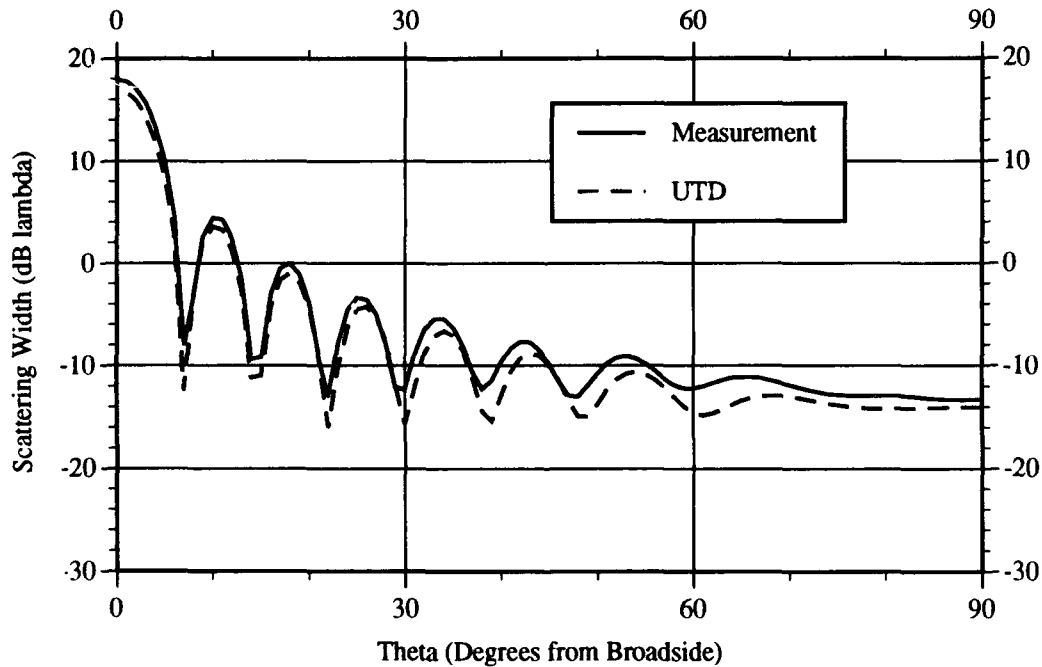


Figure 3.48. Scattering Measurement and Prediction for a  $4\lambda$  Constant Resistive Strip, VF 30,  $TM_z$

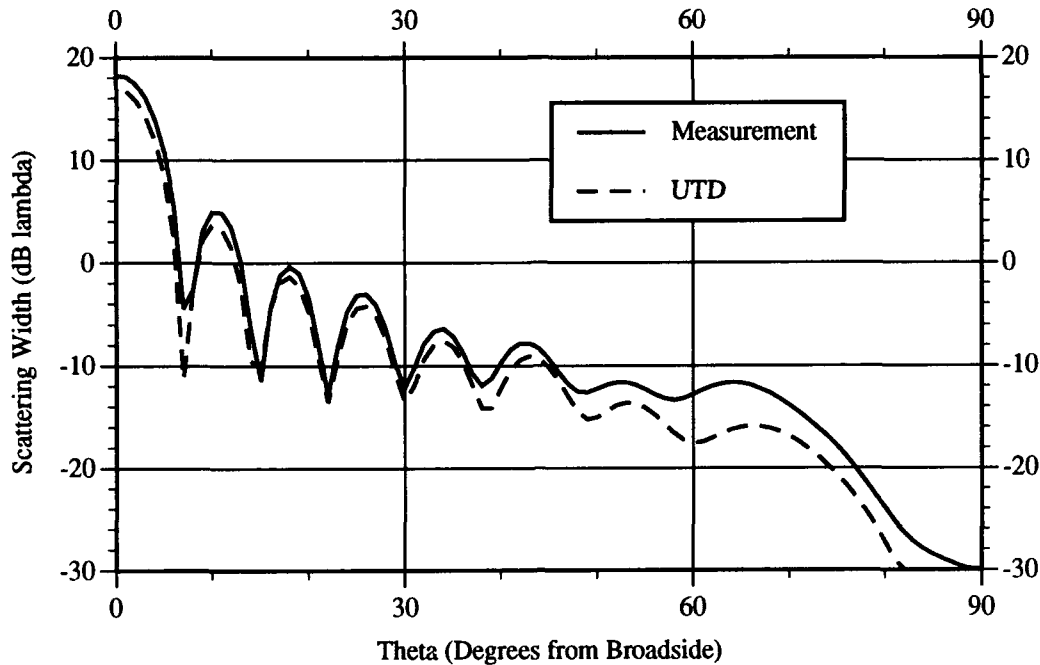


Figure 3.49. Scattering Measurement and Prediction for a  $4\lambda$  Constant Resistive Strip, VF 30,  $TE_z$

could be just an error in measurement, such as a slightly tilted target. Also, the original measurement in the waveguide to determine the resistance of the material could be suspect. Even with this offset the edge-on scattering difference is only 1.5 dB. For  $TE_z$  polarization the prediction compares very favorably to the measurement, which tends to support an error in measurement for  $TM_z$  polarization. Measurements of a VF 10 strip are contained in Figures 3.44 and 3.45. The measured scattering pattern starts lagging the prediction at about  $30^\circ$  for  $TM_z$  polarization. Edge-on scattering difference is still small at 1.5 dB. In Figure 3.45, for  $TE_z$  polarization, excellent agreement exists out to  $60^\circ$ ; then, a 1 dB to 2 dB difference exists for the rest of the comparison. For the VF 20 strip, shown in Figures 3.46 and 3.47, excellent agreement occurs for both  $TM_z$  and  $TE_z$  polarization. A slight deviation of the measurement in relation to the prediction starts at  $45^\circ$  for  $TM_z$  polarization. This doesn't affect the edge-on scattering difference of 0 dB. For both the VF 10 and VF 20 the  $TE_z$  case compares slightly better than the  $TM_z$  case. In Figures 3.48 and 3.49, the

VF 30 strip exhibits an offset between the prediction and measurement for both  $TM_z$  and  $TE_z$  polarization. The measurement is 1 dB to 2.5 dB higher than the prediction for  $TM_z$  polarization. This is a different offset than was encountered for the SC 100, where the measurement was lower than the prediction. The edge-on difference is still only 1 dB. For  $TE_z$  polarization the measurement is 1 dB to 2 dB higher than the prediction to just past  $55^\circ$ . For the rest of the comparison, the offset increases to 5 dB, then falls off again. These offsets, since they are consistent from  $TM_z$  to  $TE_z$  polarization, suggest that the waveguide measurement could be slightly off. A smaller resistance would have yielded better comparison between the prediction and measurement.

Overall the comparisons between predictions and measurements for constant resistive strips ranged from good to excellent. This was an important step to bridge since these resistive materials were used to construct the rest of the strip geometries investigated in this thesis.

Constant Resistive-Loaded Conducting Strips. Figures 3.50 through 3.53 contain the comparisons of predictions to measurements for constant resistive-loaded conducting strips. Generally, the comparisons for  $TM_z$  polarization are better than  $TE_z$  polarization. In Figure 3.50, the comparison for a constant resistive-loaded conducting strip with SC 100 loads is presented for  $TM_z$  polarization. The prediction is within 1 dB of the measurement except in two regions: from  $10^\circ$  to  $20^\circ$  and from  $48^\circ$  to  $58^\circ$ . The edge-on scattering difference comes back to almost zero. For  $TE_z$  polarization, in Figure 3.51, the first two measurement sidelobes are higher than the prediction. Starting at  $42^\circ$  the measurement deviates from the prediction for the rest of the scan. Past  $80^\circ$  the UTD prediction exhibits the same behavior as it did during the comparison of MM to UTD in the previous section. The prediction comes up from  $80^\circ$  to  $89^\circ$  and then drops to zero at edge-on. In Figure 3.52, the measurement for a constant resistive-loaded conducting strip using VF 10 and  $TM_z$  polarization compares well with the prediction. The difference is small up



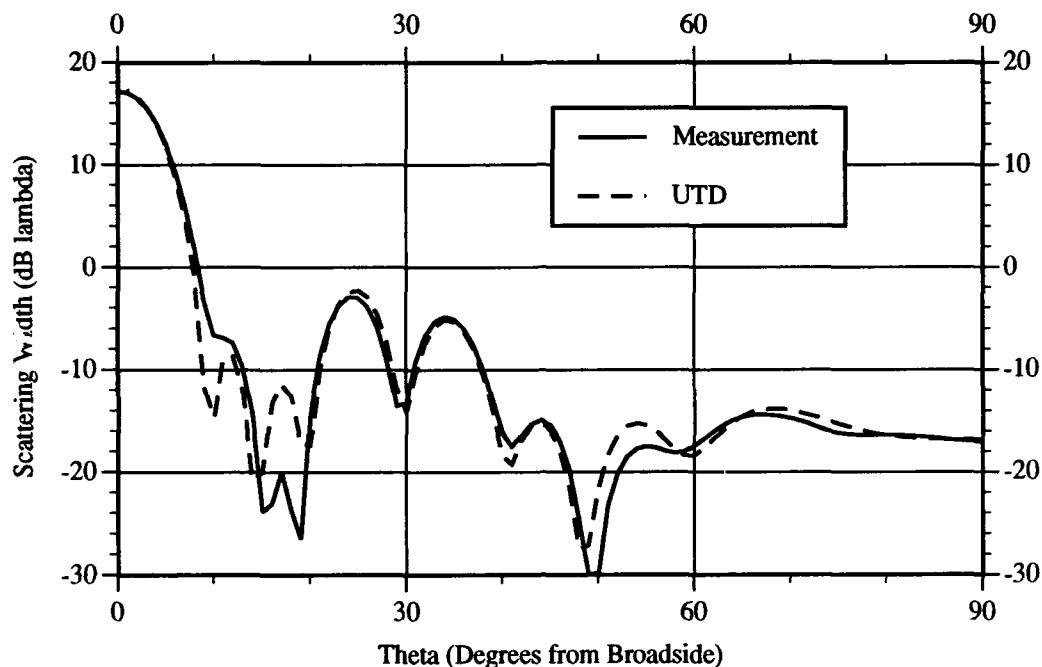


Figure 3.50. Scattering Measurement and Prediction for a  $2\lambda$  Conducting Strip with  $1\lambda$  Constant Resistive Loads, SC 100,  $TM_z$

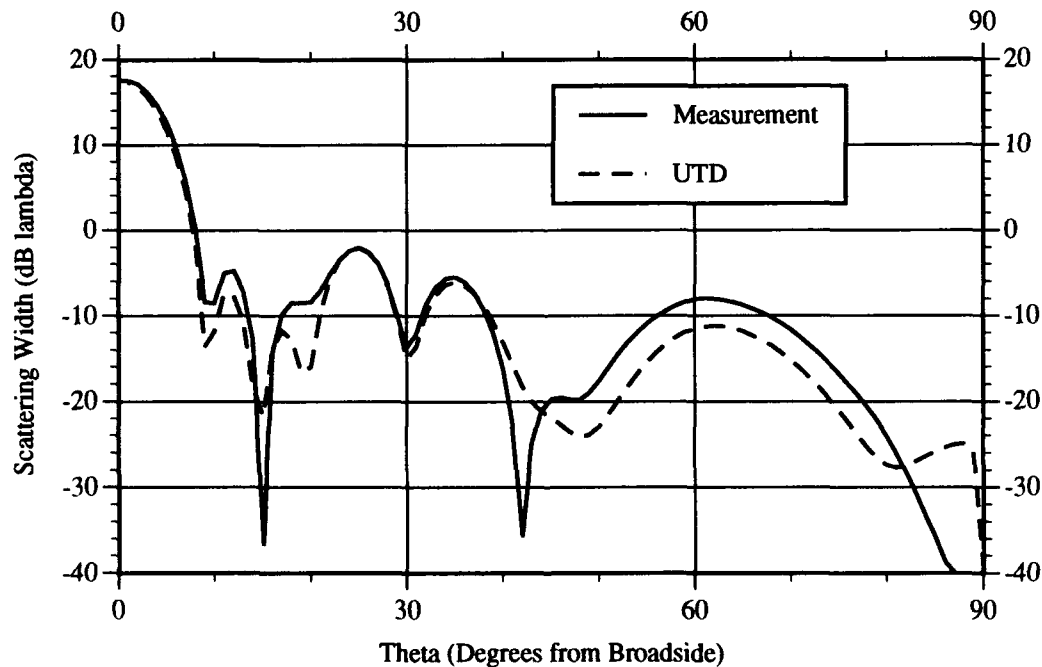


Figure 3.51. Scattering Measurement and Prediction for a  $2\lambda$  Conducting Strip with  $1\lambda$  Constant Resistive Loads, SC 100,  $TE_z$

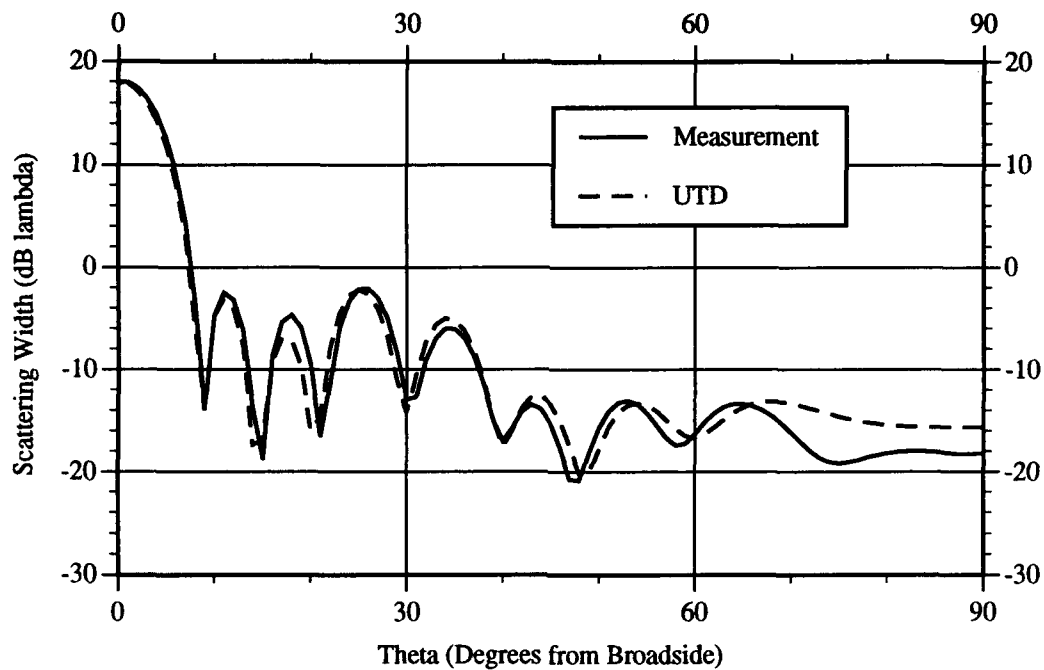


Figure 3.52. Scattering Measurement and Prediction for a  $2\lambda$  Conducting Strip with  $1\lambda$  Constant Resistive Loads, VF 10,  $TM_z$

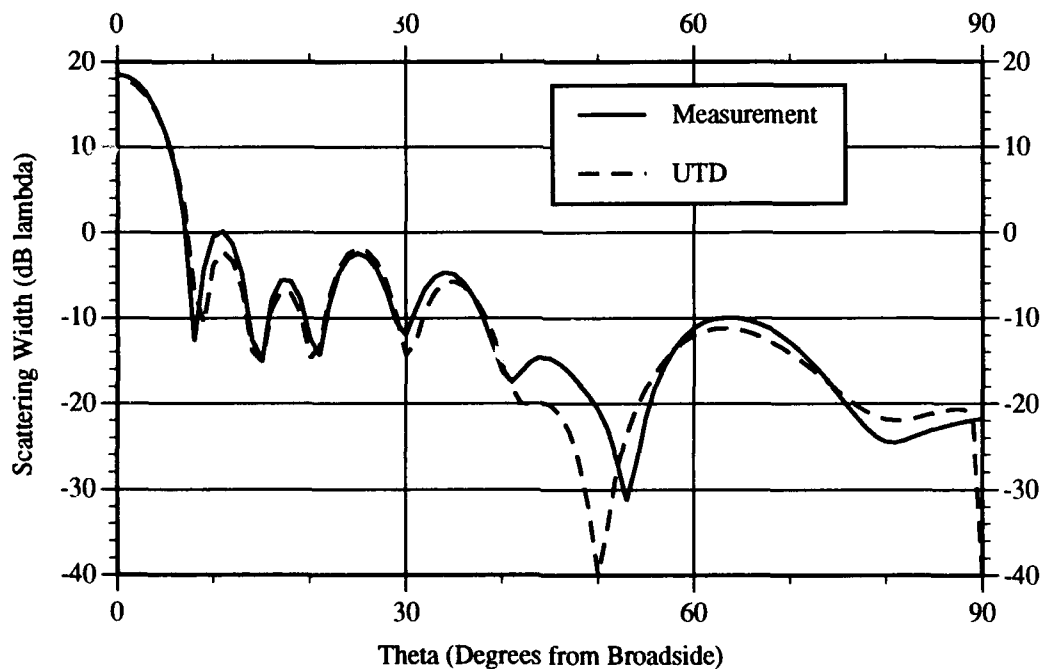


Figure 3.53. Scattering Measurement and Prediction for a  $2\lambda$  Conducting Strip with  $1\lambda$  Constant Resistive Loads, VF 10,  $TE_z$

to  $70^\circ$ . Towards edge-on the difference increases to 2.5 dB. For the same strip with  $TE_z$  polarization, Figure 3.53 shows that the difference is small up to  $40^\circ$ . At  $45^\circ$  the measurement is 5 dB higher than the prediction. Also, the measurement null is offset from the prediction null. At edge-on the prediction rises and then drops to zero as mentioned earlier.

Overall the comparisons between predictions and measurements for constant resistive-loaded conducting strips ranged from fair to good. Generally, the  $TM_z$  polarization showed better agreement than the  $TE_z$  polarization, especially near edge-on.

Tapered Resistive Strips. Figures 3.54 through 3.57 contain the comparisons between predictions and measurements for tapered resistive strips. Figures 3.54 and 3.55 show the measurements of a taper constructed from the VF 10 and VF 20 material. Both  $TM_z$  and  $TE_z$  polarization show good comparisons between predictions and measurements. Figure 3.54 shows very good agreement until just past  $70^\circ$  where the edge-on difference increases to only 2.5 dB. Figure 3.55 shows very good agreement to  $60^\circ$  from broadside. In the region from  $60^\circ$  to  $70^\circ$  a deviation of up to 4 dB is encountered. Figure 3.56 and 3.57 represent the taper constructed of VF 10, VF 20, and VF 30 material for  $TM_z$  and  $TE_z$  polarization, respectively. These comparisons don't agree as well as the previous two. For  $TM_z$  polarization the prediction follows the measurement generally well up to  $60^\circ$ . Then a measurement null occurs that is not represented by the prediction. Still, the edge-on difference is just over 2.5 dB. For  $TE_z$  polarization the prediction is relatively close to the prediction up to  $38^\circ$ ; then, falls off as compared to the measurement.

Overall, for tapered resistive strips, the strip constructed of VF 10 and VF 20 had measurements that compared better to predictions. For the strip constructed of VF 10, VF 20, and VF 30,  $TM_z$  polarization had better comparison than  $TE_z$  polarization.

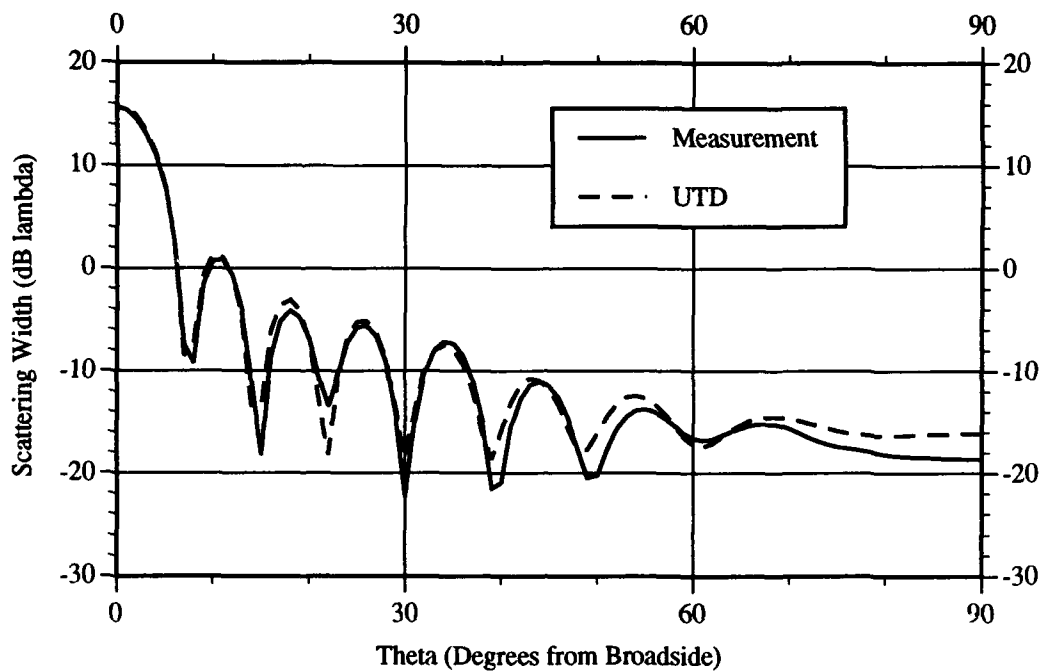


Figure 3.54. Scattering Measurement and Prediction for a  $4\lambda$  Tapered Resistive Strip, VF 10 and VF 20,  $TM_z$

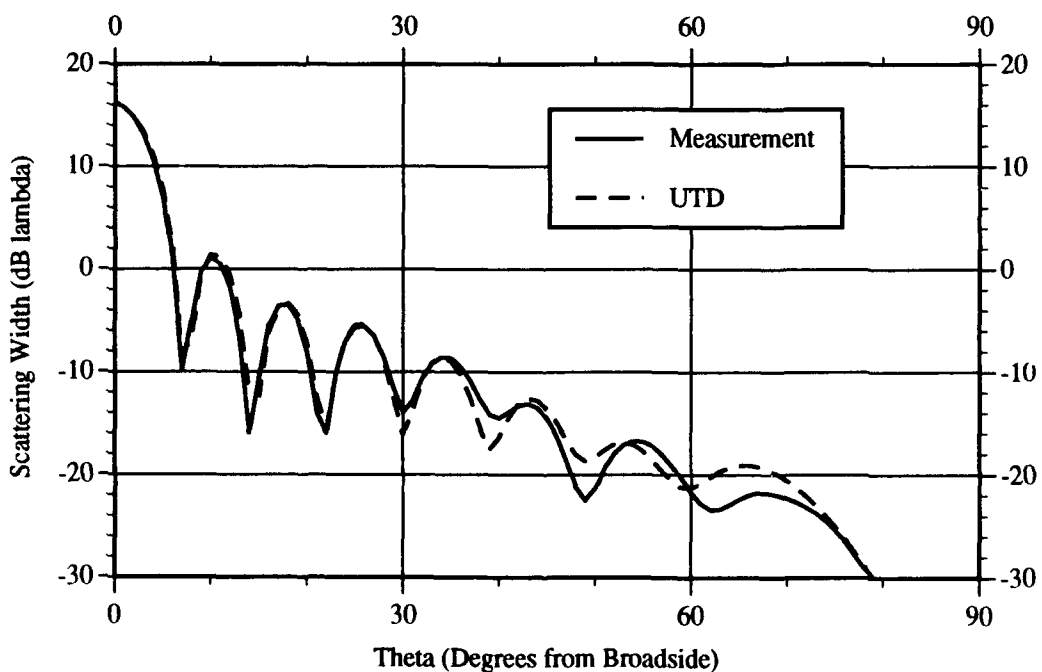


Figure 3.55. Scattering Measurement and Prediction for a  $4\lambda$  Tapered Resistive Strip, VF 10 and VF 20,  $TE_z$

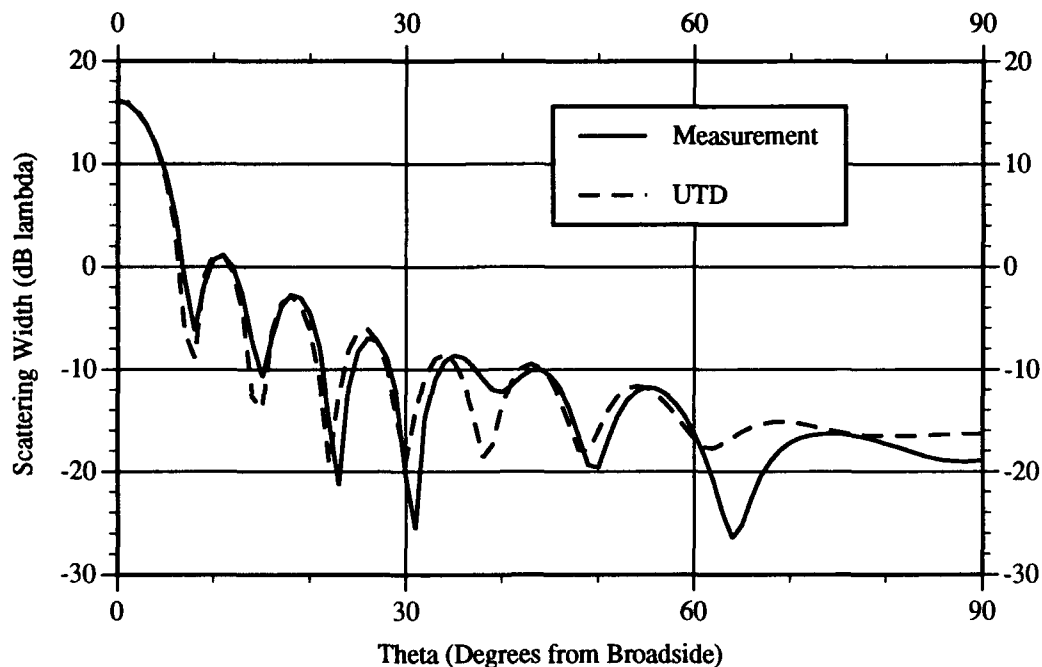


Figure 3.56. Scattering Measurement and Prediction for a  $4\lambda$  Tapered Resistive Strip, VF 10, VF 20, and VF 30,  $TM_z$

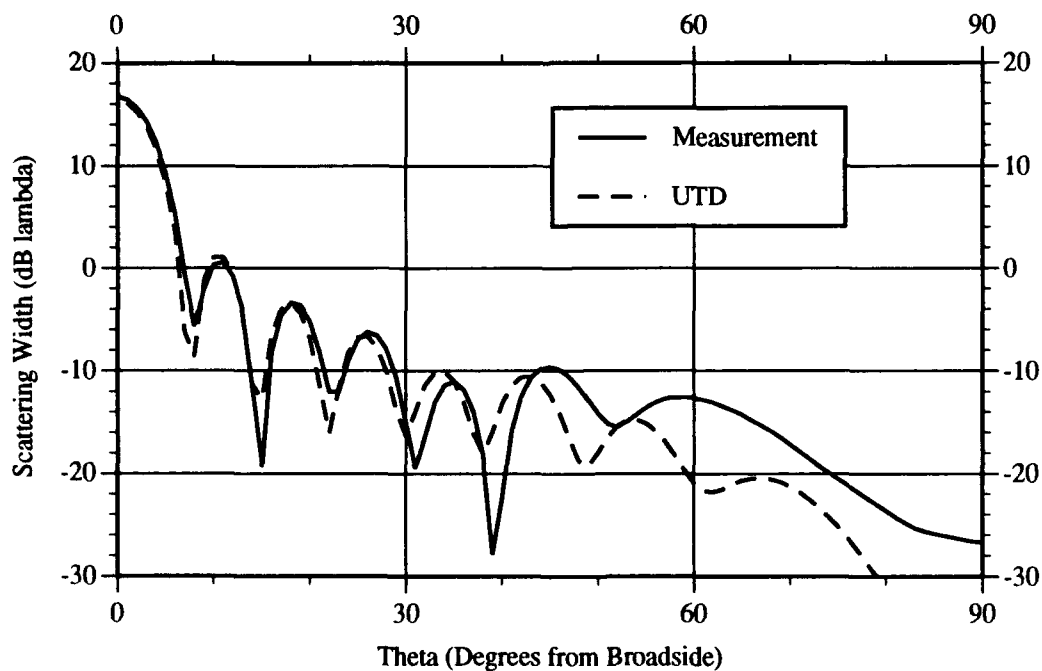


Figure 3.57. Scattering Measurement and Prediction for a  $4\lambda$  Tapered Resistive Strip, VF 10, VF 20, and VF 30,  $TE_z$

Tapered Resistive-Loaded Conducting Strips. Figures 3.58 through 3.62 present the comparisons between measurements and predictions for tapered resistive-loaded conducting strips. Two types were measured: tapers constructed from VF material and a Sheldahl taper. Measurements for a loaded strip composed of VF 10 and VF 20 material are contained in Figures 3.58 and 3.59. For  $TM_z$  polarization, the prediction agrees within 3.5 dB for all the peaks. Edge-on difference is about 2 dB. For  $TE_z$  polarization, the comparison is better for the first four sidelobes, but then the prediction fails to represent the next measurement sidelobe. Again, the UTD prediction rises slightly before dropping to zero. Measurements for a loaded strip composed of VF 10, VF 20, and VF 30 material are contained in Figures 3.60 and 3.61. Figure 3.60 shows the excellent agreement between the prediction and measurement for  $TM_z$ . Edge-on difference for this case is 0 dB. Figure 3.61 shows some differences for several sidelobes, with the maximum difference being 7.5 dB. The ever present rise and then drop towards edge-on is evident also for the prediction.

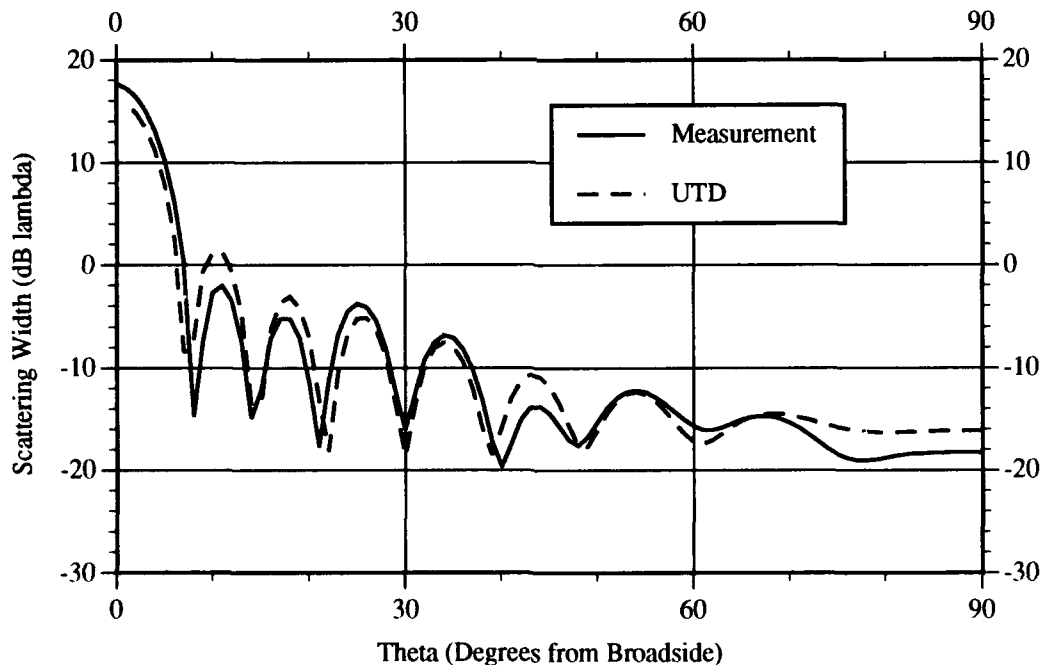


Figure 3.58. Scattering Measurement and Prediction for a  $2\lambda$  Conducting Strip with  $1\lambda$  Tapered Resistive Loads, VF 10 and VF 20,  $TM_z$

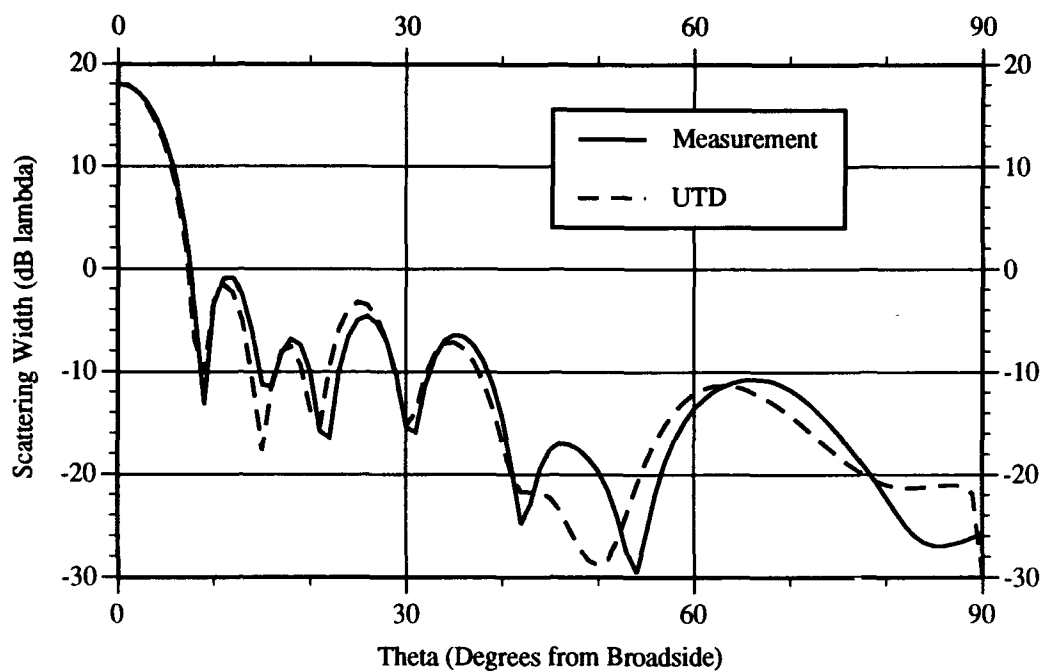


Figure 3.59. Scattering Measurement and Prediction for a  $2\lambda$  Conducting Strip with  $1\lambda$  Tapered Resistive Loads, VF 10 and VF 20,  $TE_z$

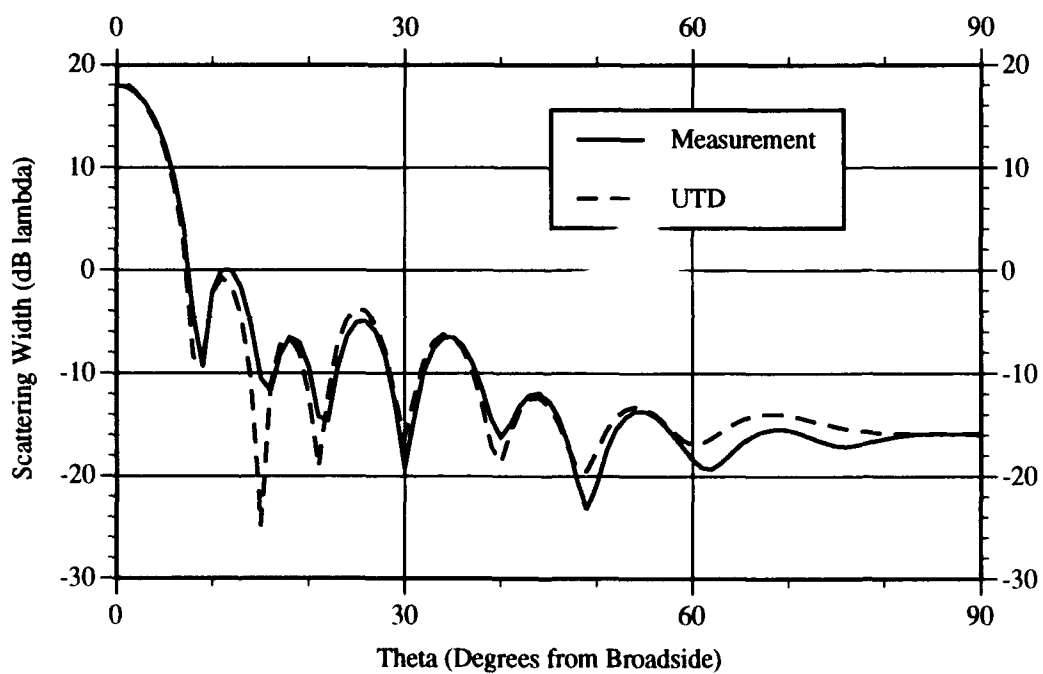


Figure 3.60. Scattering Measurement and Prediction for a  $2\lambda$  Conducting Strip with  $1\lambda$  Tapered Resistive Loads, VF 10, VF 20, and VF 30,  $TM_z$

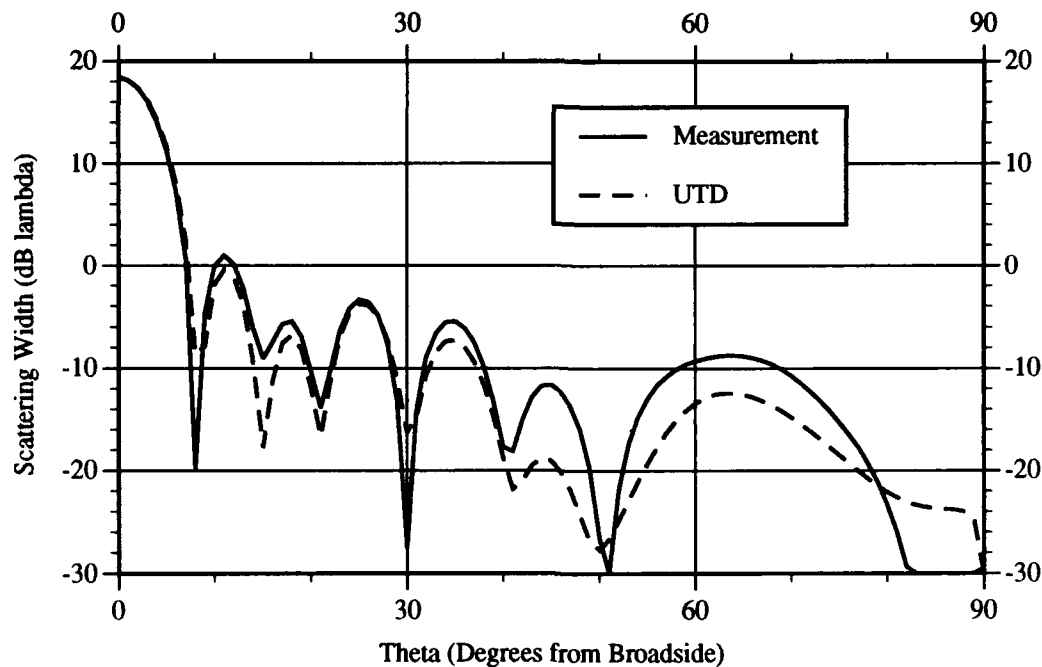


Figure 3.61. Scattering Measurement and Prediction for a  $2\lambda$  Conducting Strip with  $1\lambda$  Tapered Resistive Loads, VF 10, VF 20, and VF 30,  $TE_z$

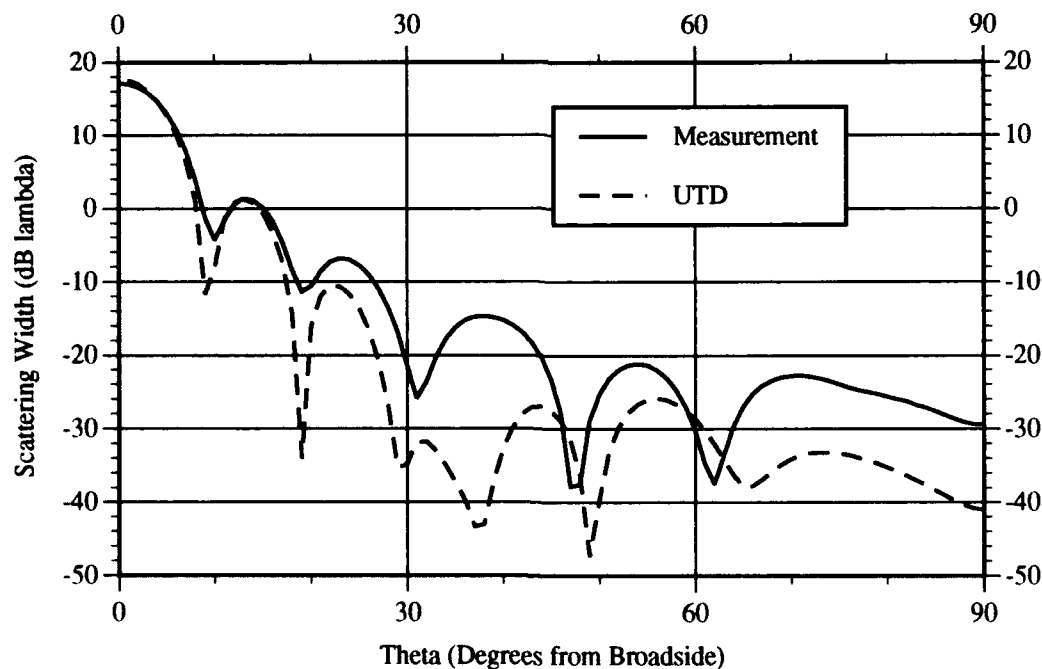


Figure 3.62. Scattering Measurement and Prediction for a  $2\lambda$  Conducting Strip with  $1\lambda$  Tapered Resistive Loads, Sheldahl,  $TM_z$



Figure 3.62 presents the measurement using the 1 in Sheldahl taper to construct the loaded strip. Differences between prediction and measurement are over 10 dB in some cases. This is probably due to the lack of specified resistance values on the taper. Resistance measurements were made for every 1/4 in on the taper, yielding five values. To model this for the prediction, discrete linear steps were calculated between the measured values. It's possible that the number of measured values was not enough to accurately predict the scattering from the loaded strip. In any event, further measurements on the Sheldahl taper were not made, although accurate knowledge of the Sheldahl resistance variation is highly suspect as the cause for the poor agreement.

### Limitations

As the verification of the rigorous UTD formulation indicates, the UTD predictions overall compared very well to MM predictions and measurements. The only major discrepancy that surfaced was the prediction of edge-on or close to edge-on scattering for certain strip geometries. For  $TM_z$  polarization this discrepancy was noted during comparisons between UTD and MM predictions. Specifically, this surfaced during comparisons for tapered resistive strips. Agreement between UTD and MM for edge-on scattering level worsened when the degree of the polynomial describing the taper increased. For  $TE_z$  polarization, an odd behavior towards edge-on was discovered for all strip geometries except constant resistive strips. This suggests that inclusion of up to third order diffractions handled the  $TM_z$  case better than the  $TE_z$  case. (The  $TE_z$  case would require more multiple diffractions for better accuracy in edge-on scattering predictions.) In any event, for the reasons mentioned earlier, the edge-on scattering level for  $TM_z$  polarization is more significant than it is for  $TE_z$  polarization. Thus, edge-on scattering levels for tapered resistive strips and tapered resistive-loaded conducting strips were investigated further for  $TM_z$  polarization.

**Tapered Resistive Strip Edge-On Scattering.** UTD predictions were compared to MM predictions for varying degrees of taper. Specifically, the constants  $a$  and  $b$  were varied for a  $4\lambda$  strip with a taper of  $ax|b$ . Figures 3.63 and 3.64 present plots that show the edge-on scattering difference for various values of  $a$  and  $b$ . In Figure 3.63,  $b$  is varied from 0.5 to 6 for values of  $a$  equal to 0.5, 1, and 2. Generally, as  $a$  and  $b$  increase the edge-on difference increases also. The third-order diffractions in the UTD formulation are not sufficient for the edge-on scattering prediction. The  $|x|^5$  resistive taper does not seem to follow the general trend in Figure 3.63. As Figure 3.65 shows, although the UTD prediction doesn't agree towards edge-on the UTD sidelobe pattern rises at edge-on. Figure 3.64 shows the differences when  $a$  is varied from 0.0625 to 16 for values of  $b$  equal to 2, 3, and 4. Again, as  $a$  and  $b$  increase the edge-on difference increases for the same reason. The interesting feature of this plot is that the differences for the  $4|x|^b$  taper are very close to each other. A reason for this was not evident. Also, for  $a = 16$ , the plot deviated

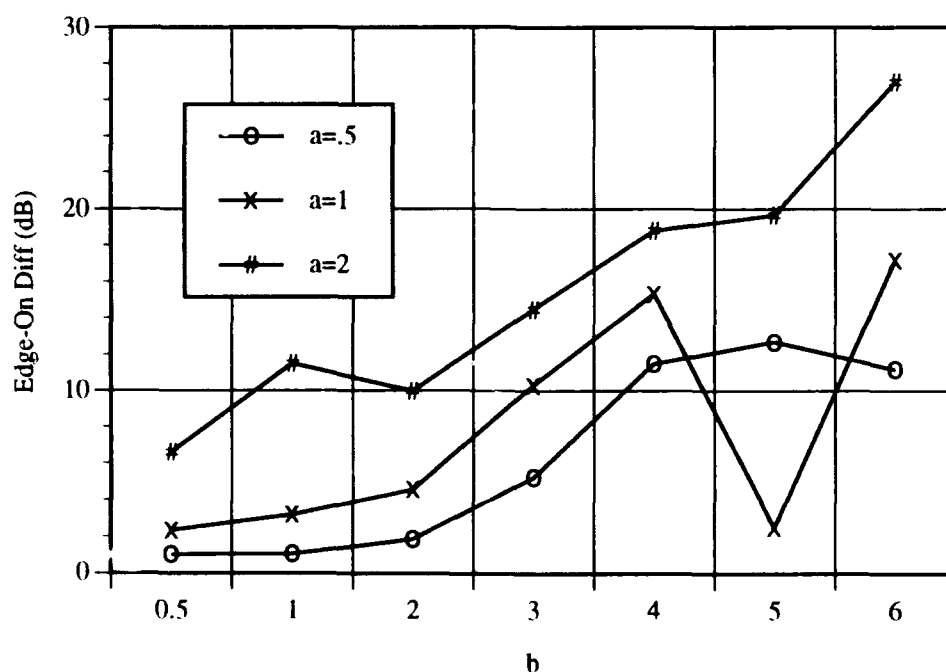


Figure 3.63. Edge-On Scattering Difference Between UTD and MM for an  $ax|b$  Tapered Resistive Strip versus  $b$

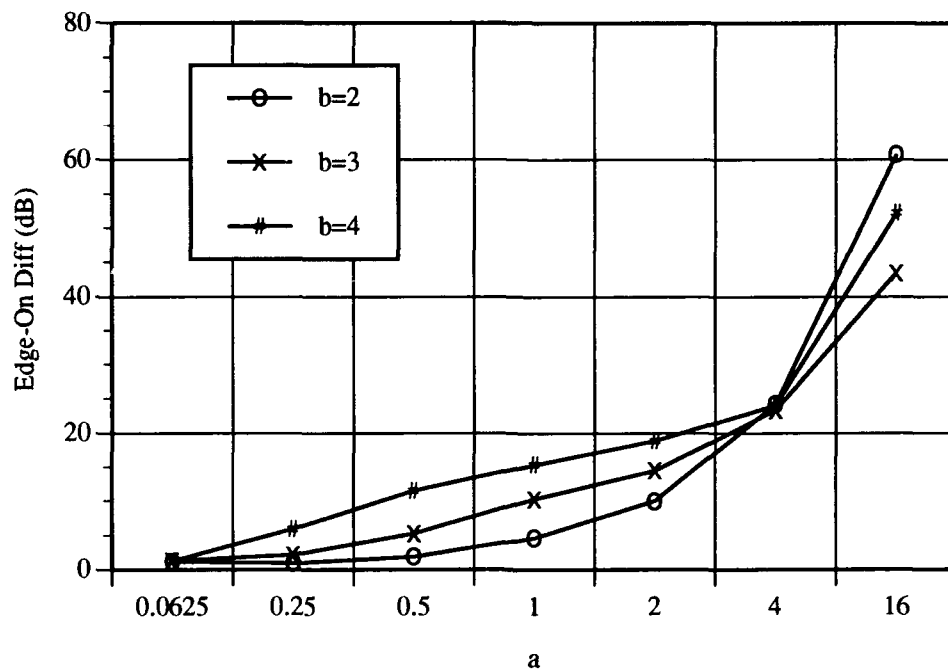


Figure 3.64. Edge-On Scattering Difference Between UTD and MM for an  $|a|b$  Tapered Resistive Strip versus  $a$

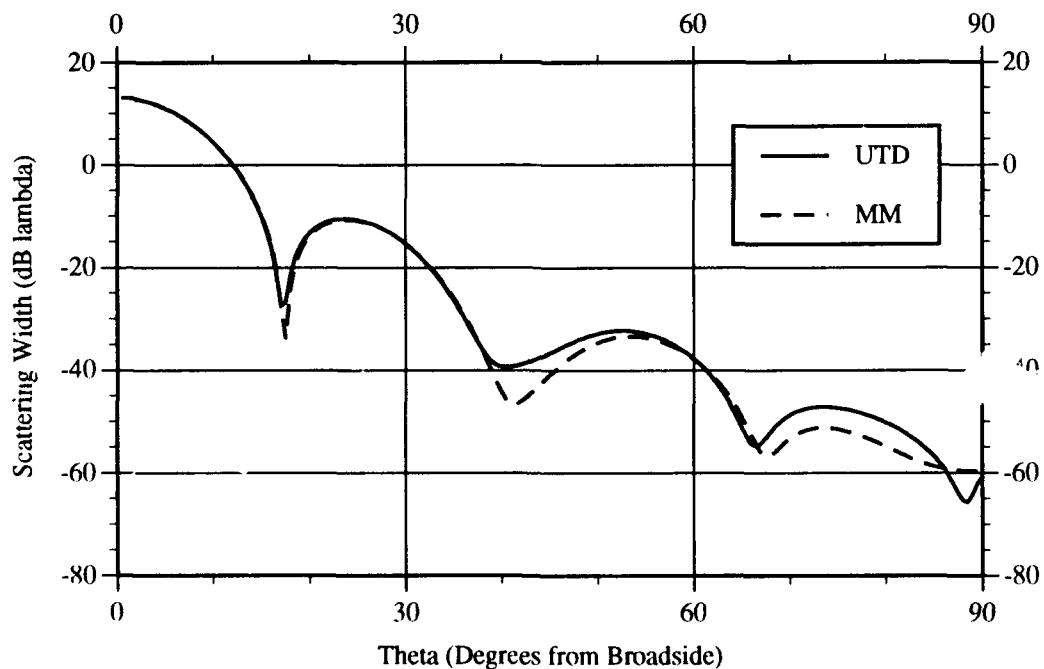


Figure 3.65. Scattering Prediction for a  $4\lambda$  Tapered Resistive Strip,  $\eta = |x|^5$ ,  $TM_z$

from the trend in that the  $16 \times 2$  taper had the largest difference. In any event, the edge-on difference for  $a = 16$  is very high for all three tapers considered.

Tapered Resistive-Loaded Conducting Strip Edge-On Scattering. For tapered resistive-loaded conducting strips the same types of comparisons were made as for tapered resistive strips. Figure 3.66 contains the comparisons where  $b$  is varied from 0.5 to 6 for values of  $a$  equal to 0.5, 1, and 2. The major difference between this plot and the same plot for tapered resistive strips is that the edge-on difference is much less across the board. The reason for the decreased edge-on difference is because only  $1\lambda$  loads were considered; thus, the maximum resistance at the end of the taper is the constant  $a$ . The other difference is that for  $a = 2$  the trace does not follow the general trend. In any case most of the points are within the 4 dB level which shows good comparison. Figure 3.67 shows the comparisons where  $a$  is varied and  $b$  is held constant at 2, 3, and 4.

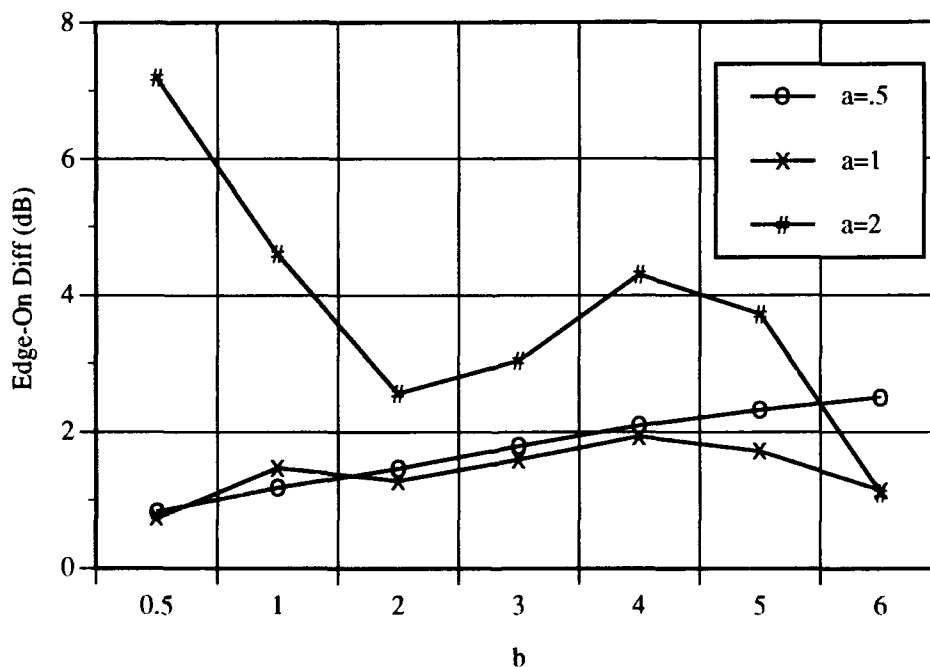


Figure 3.66. Edge-On Scattering Difference Between UTD and MM for an  $a(|x| - 1)^b$  Tapered Resistive-Loaded Conducting Strip versus  $b$

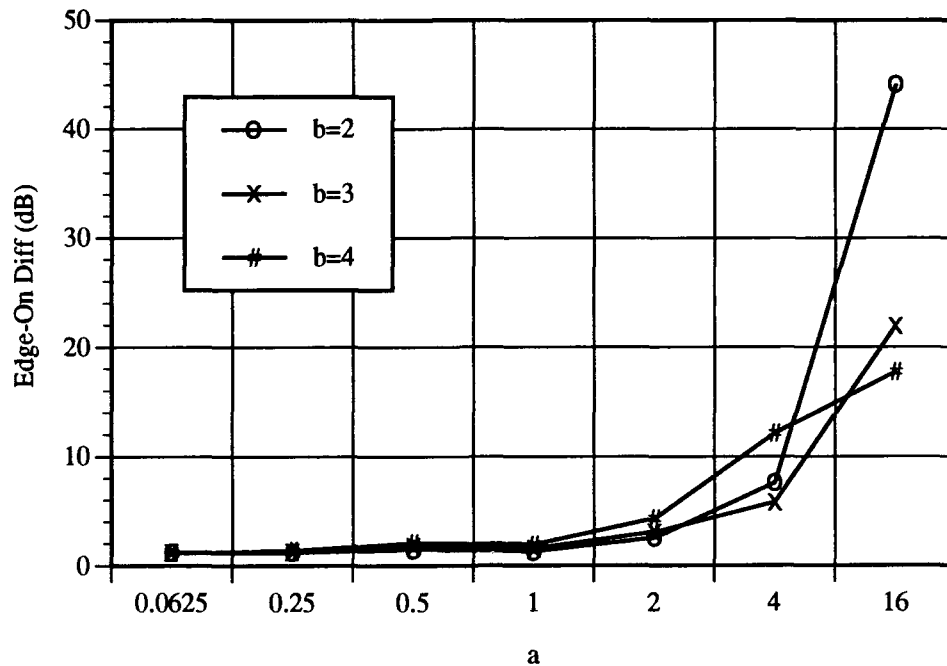


Figure 3.67. Edge-On Scattering Difference Between UTD and MM for an  $a(|x| - 1)^b$  Tapered Resistive-Loaded Conducting Strip versus  $a$

Differences are within 4 dB to 5 dB except for values of  $a$  equal to 4 and 16. A general trend of increasing difference occurs up to  $a = 4$  where a crossover occurs for  $a = 16$ .

Overall, the plots indicate that the differences are much larger for a resistive tapered strip because of the wider variance of resistance over the taper than for the tapered resistive-loaded conducting strip. A general trend applicable to all the plots was not evident. For the tapered resistive-loaded conducting strip, most of the tapers show good agreement with the MM solution for edge-on scattering.

#### IV. Scattering Characteristics of Resistive-Loaded Conducting Strips

This chapter explores the scattering characteristics of constant resistive-loaded conducting strips and tapered resistive-loaded conducting strips with an emphasis on scattering reduction.  $TM_z$  polarization was selected for the investigation because the rigorous UTD formulation compares better to the MM solution. Also, the edge-on scattering level is more significant. All strips are a total of  $4\lambda$  wide with  $2\lambda$  center conductors and  $1\lambda$  loads, as shown in Figures 3.2.b and 3.2.d. Resistive tapers of  $a(|x| - 1)^b$  are modeled with ten segments per wavelength, as presented in Figure 3.5. Limitations in Chapter 3 indicated edge-on difference for tapered resistive-loaded conducting strips increased to over 40 dB for the most extreme taper. Consequently, only those cases where the edge-on difference was less than 5 dB were used in this investigation. UTD predictions are presented in overlay charts with a  $4\lambda$  conducting strip to ascertain the level of scattering reduction.

##### Constant Resistive-Loaded Conducting Strips

Figures 4.1 through 4.3 contain the scattering patterns for constant resistive-loaded conducting strips. The load is varied from  $\eta = 0.5$  to 4 to find its effect on the scattering levels. Each plot has two scattering patterns that are compared to a conducting strip. Successive plots increase  $\eta$ . This approach made it easier to analyze the effect of the edge loading. As Figure 4.1 indicates, an effect of edge-loading with  $\eta = 0.5$  is the main lobe gets broader and its peak decreases by 3 dB compared to the conducting strip. Also, all but sidelobes three and four decrease significantly and edge-on scattering decreases by 8.7 dB. When  $\eta$  is increased to 1.5 the entire pattern gets broader. The main lobe's peak decreases by 4 dB compared to the conducting strip while edge-on scattering decreases by 5 dB. Thus, for increasing  $\eta$  broadside scattering is still going down; but, edge-on scattering is

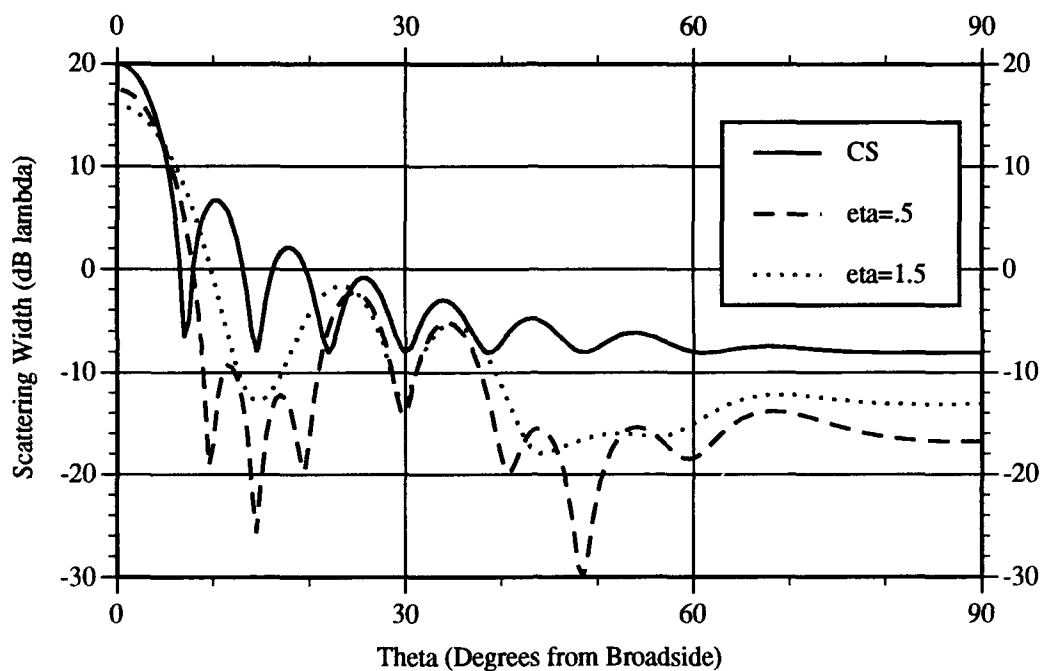


Figure 4.1. Scattering Predictions for  $2\lambda$  Conducting Strips with  $1\lambda$  Constant Resistive Loads and Conducting Strip Reference,  $\eta = 0.5$  and  $1.5$

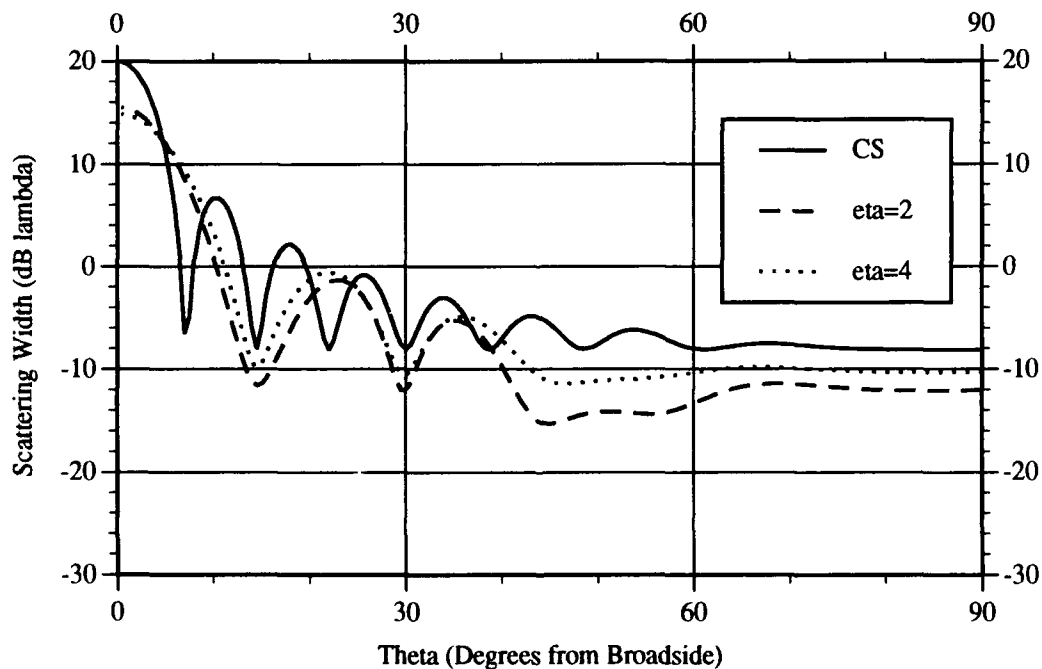


Figure 4.2. Scattering Predictions for  $2\lambda$  Conducting Strips with  $1\lambda$  Constant Resistive Loads and Conducting Strip Reference,  $\eta = 2$  and  $4$

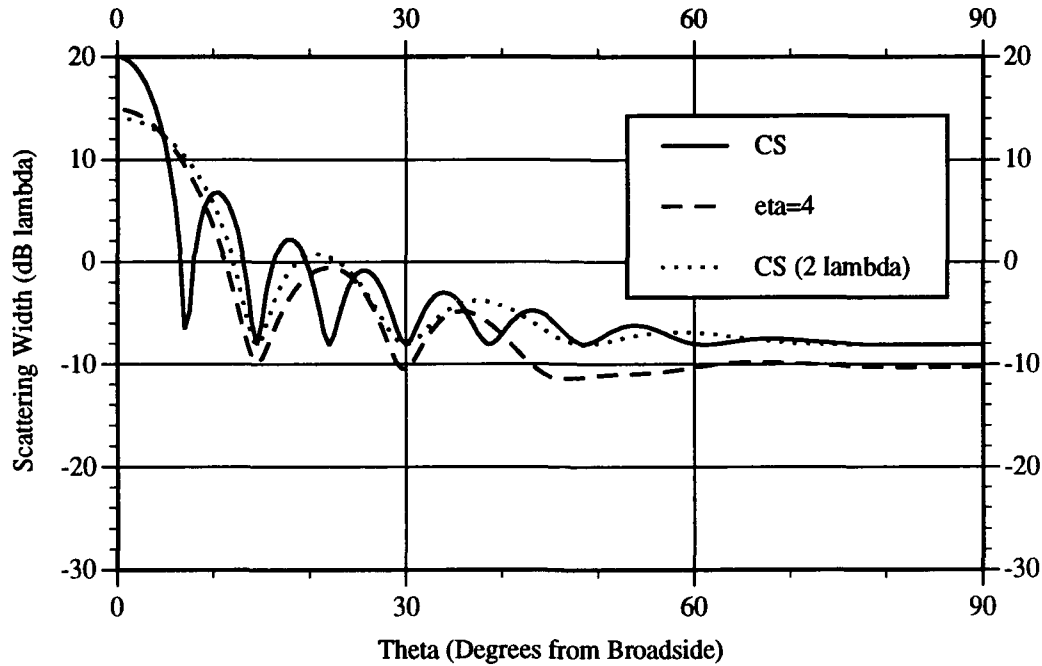


Figure 4.3. Scattering Predictions for  $2\lambda$  Conducting Strips with  $1\lambda$  Constant Resistive Loads and Conducting Strip References,  $\eta = 4$

coming up. Figure 4.2 shows the effect on the scattering by increasing  $\eta$  to 2 and 4. The same trend of broadening continues to occur. The main lobe's peak decreases by 4.4 dB and 5 dB compared to the conducting strip and edge-on scattering decreases by 3.9 dB and 2.2 dB for  $\eta$  equal to 2 and 4, respectively. The change of the scattering pattern with increasing  $\eta$  is reaching the limit of a  $2\lambda$  conducting strip as shown in Figure 4.3. This is because as  $\eta$  increases the resistive loads look more like free space. There seems to be an optimum value of  $\eta$  around 0.5 for decreases in sidelobe and edge-on scattering levels.

#### Tapered Resistive-Loaded Conducting Strips, $\text{Eta} = a(|x| - 1)^b$

Investigating the trends in scattering from an  $a(|x| - 1)^b$  tapered load is more involved than for constant loads, since many combinations of  $a$  and  $b$  can be used to designate the taper. Two different routes were used to investigate trends for the tapered loads. First,  $b$  was held constant and  $a$  was varied; then,  $a$  was held constant and  $b$  was



varied. This resulted in many more plots than for the constant resistive-loaded case. Each individual scattering pattern was repeated, but, in a different comparison. This allowed conclusions to be made about the effects of changing the constants  $a$  and  $b$ .

Constant  $b$ , Varying  $a$ . Figures 4.4 through 4.11 present the changes in scattering predictions when  $b$  was held constant and  $a$  was varied for  $a(|x| - 1)^b$  tapered resistive-loaded conducting strips. The constant  $a$  varied from  $1/4$  to  $2$  for each pair of scattering prediction plots. Two plots were used for each case to facilitate the analysis. Figures 4.4 and 4.5 present the case for  $b$  equal to  $1$ . As Figure 4.4 indicates, for smaller values of  $a$ , the scattering patterns have the general shape of the reference conducting strip, but with a reduced level for the sidelobes. Even though the main lobe has not been reduced significantly, the sidelobes are increasingly lower as  $\theta$  increases. The edge-on scattering is reduced by  $6.6$  dB and  $10.2$  dB as compared to the conducting strip for  $\eta$  equal to  $1/4$  ( $|x| - 1$ ) and  $1/2$  ( $|x| - 1$ ), respectively. As the constant  $a$  increases the scattering patterns start to broaden and decrease further. Figure 4.5 shows how the edge-on scattering levels are reduced even further as compared to the reference. Increasing the constant  $a$  to  $1$  and  $2$  result in edge-on scattering decreases of  $14.4$  dB and  $20.1$  dB, respectively as compared to the conducting strip. Also, the main lobe's scattering level decreases slightly. The overall scattering decrease presented in Figures 4.4 and 4.5 is much different from that presented previously for the constant resistive-loaded conducting strips. This is because the resistive taper has a smoother transition from the conductor to free space. The main lobe's scattering level doesn't decrease as much as it does for constant resistive loads. But, as the constant  $a$  increases, a greater decrease of the sidelobes and edge-on scattering levels exist. The remaining Figures 4.6 through 4.11 exhibit the same general trend. As  $a$  increases, the main lobe is affected slightly; but, the sidelobes and edge-on scattering levels decrease significantly as compared to the conducting strip reference. As much as a  $23.2$  dB decrease in edge-on scattering is encountered for the  $2(|x| - 1)^4$  resistive taper.

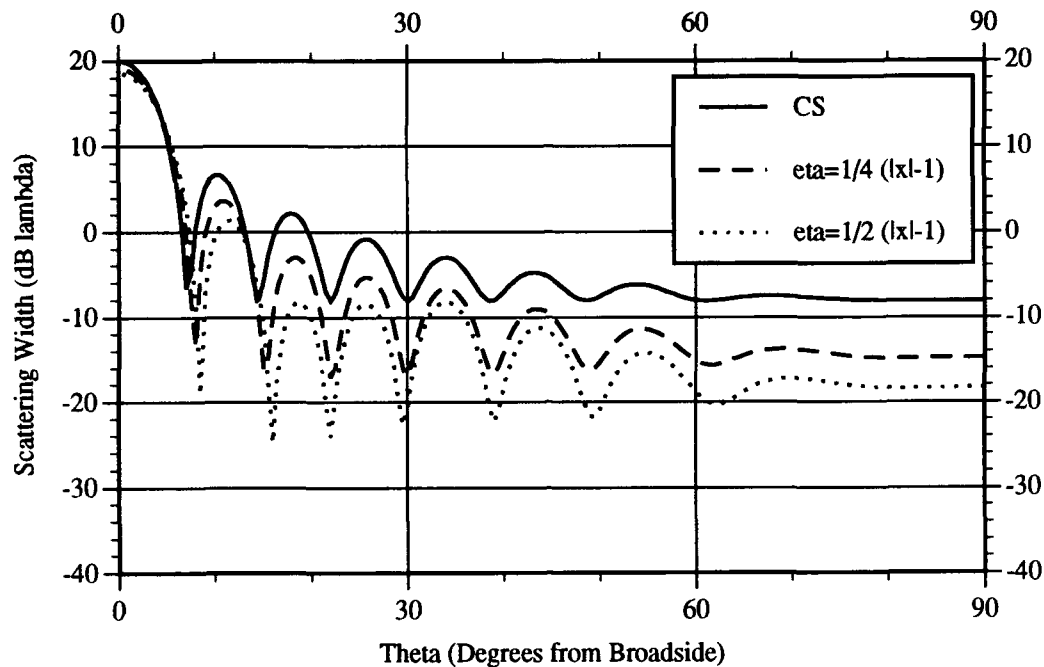


Figure 4.4. Scattering Predictions for  $2\lambda$  Conducting Strips with  $1\lambda$  Tapered Resistive Loads and Conducting Strip Reference,  $\eta = 1/4 (|x| - 1)$  and  $1/2 (|x| - 1)$

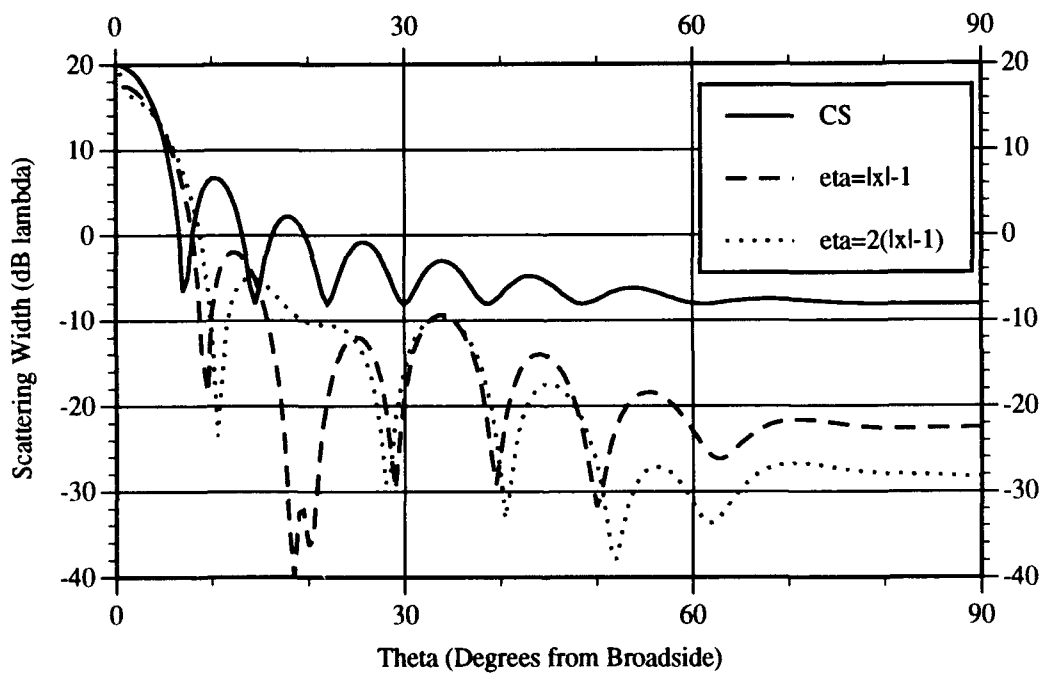


Figure 4.5. Scattering Predictions for  $2\lambda$  Conducting Strips with  $1\lambda$  Tapered Resistive Loads and Conducting Strip Reference,  $\eta = |x| - 1$  and  $2(|x| - 1)$

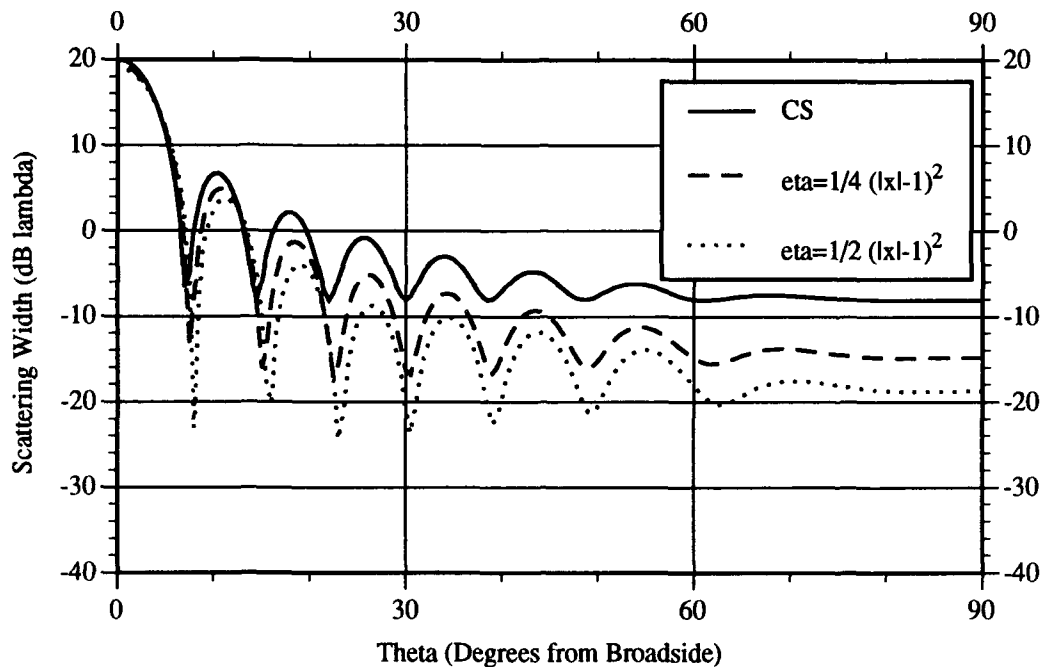


Figure 4.6. Scattering Predictions for  $2\lambda$  Conducting Strips with  $1\lambda$  Tapered Resistive Loads and Conducting Strip Reference,  $\eta = 1/4 (|x| - 1)^2$  and  $1/2 (|x| - 1)^2$

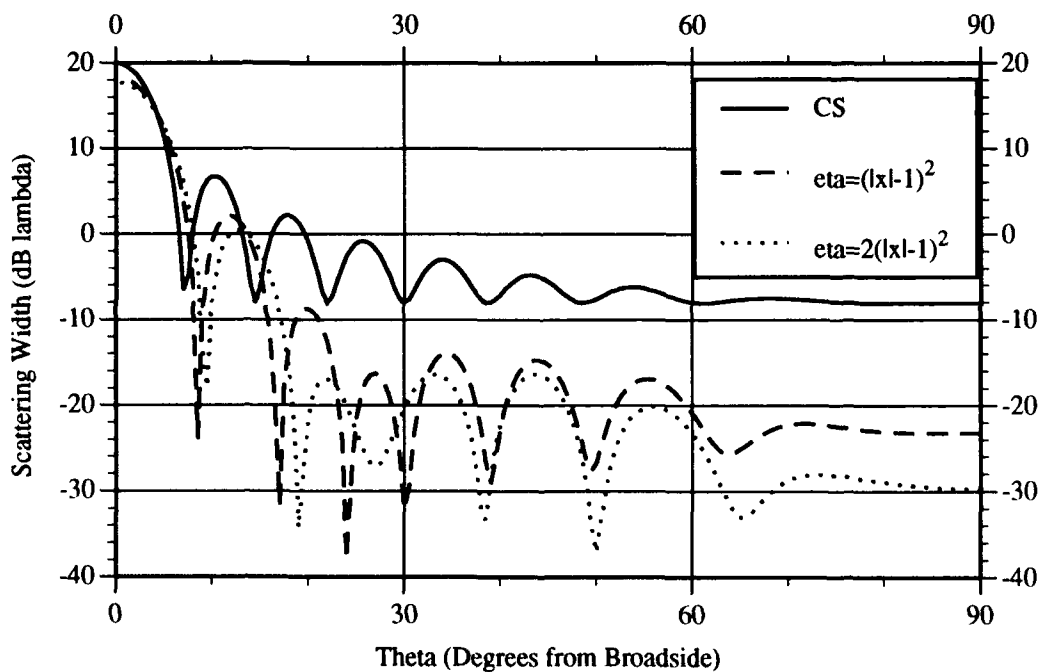


Figure 4.7. Scattering Predictions for  $2\lambda$  Conducting Strips with  $1\lambda$  Tapered Resistive Loads and Conducting Strip Reference,  $\eta = (|x| - 1)^2$  and  $2(|x| - 1)^2$

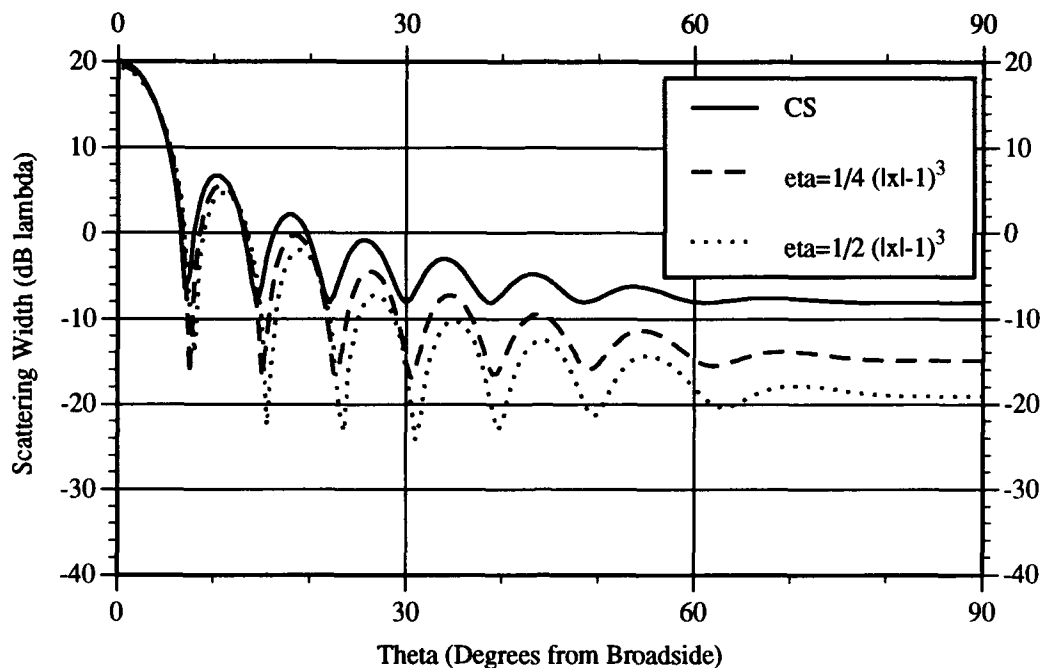


Figure 4.8. Scattering Predictions for  $2\lambda$  Conducting Strips with  $1\lambda$  Tapered Resistive Loads and Conducting Strip Reference,  $\eta = 1/4 (|x| - 1)^3$  and  $1/2 (|x| - 1)^3$

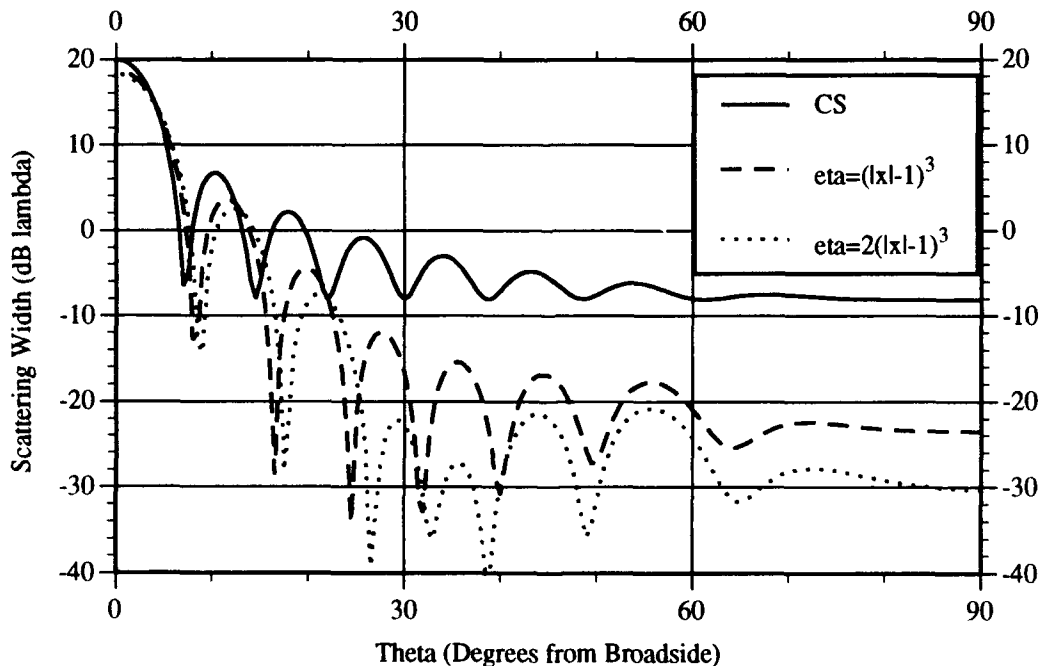


Figure 4.9. Scattering Predictions for  $2\lambda$  Conducting Strips with  $1\lambda$  Tapered Resistive Loads and Conducting Strip Reference,  $\eta = (|x| - 1)^3$  and  $2(|x| - 1)^3$

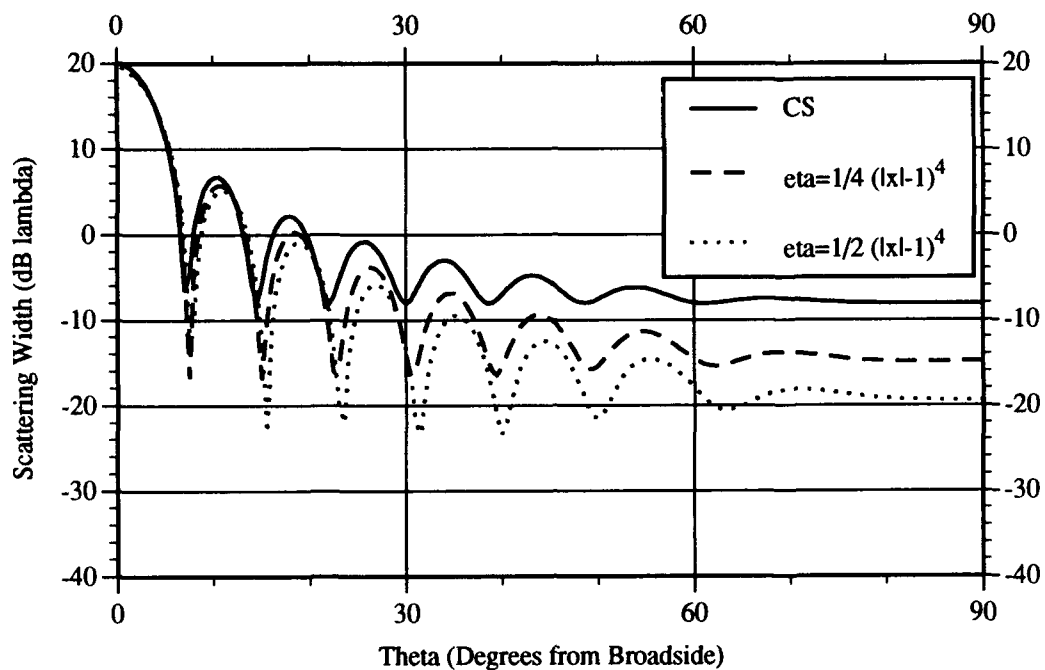


Figure 4.10. Scattering Predictions for  $2\lambda$  Conducting Strips with  $1\lambda$  Tapered Resistive Loads and Conducting Strip Reference,  $\eta = 1/4 (|x| - 1)^4$  and  $1/2 (|x| - 1)^4$

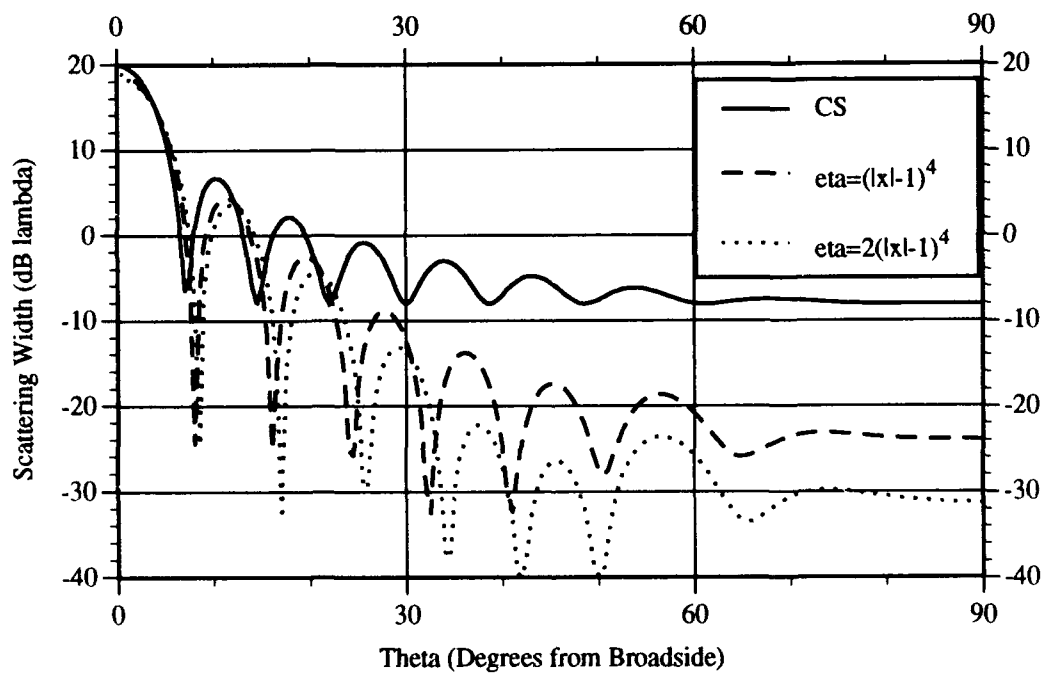


Figure 4.11. Scattering Predictions for  $2\lambda$  Conducting Strips with  $1\lambda$  Tapered Resistive Loads and Conducting Strip Reference,  $\eta = (|x| - 1)^4$  and  $2(|x| - 1)^4$

Constant a, Varying b. Figures 4.12 through 4.19 present the scattering patterns when  $a$  is held constant and  $b$  is varied from 1 to 4. Generally, increasing the degree of the taper for constant  $a$  didn't change the scattering patterns significantly. Typically, edge-on scattering levels remained close to each other for each value of  $b$ . This is because with  $1\lambda$  wide loads, variation in the resistance over the taper is not as great as for the tapered resistive strips. For larger values of the constant  $a$ , there were some noticeable changes in the scattering patterns. What's interesting is that starting in Figures 4.16 and 4.17, it becomes apparent that comparison of the sidelobe levels depends on the sector of the scan considered. Figure 4.19 shows that the  $2(|x| - 1)^3$  taper has lower sidelobe levels than the  $2(|x| - 1)^4$  taper to about  $40^\circ$ ; then, has higher sidelobes for the rest of the scan.

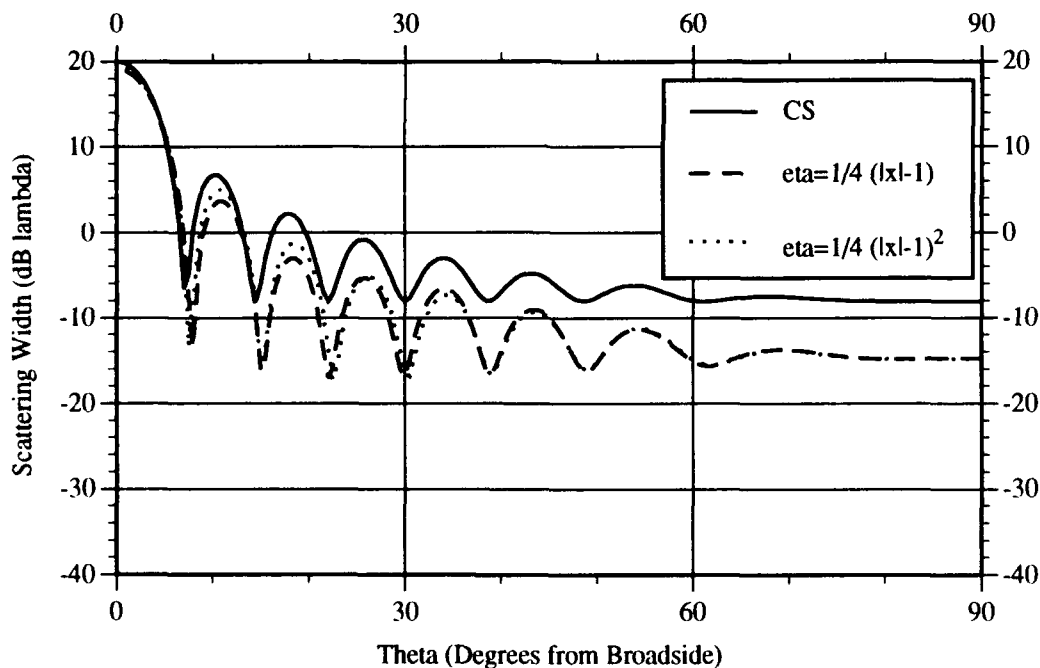


Figure 4.12. Scattering Predictions for  $2\lambda$  Conducting Strips with  $1\lambda$  Tapered Resistive Loads and Conducting Strip Reference,  $\eta = 1/4 (|x| - 1)$  and  $1/4 (|x| - 1)^2$

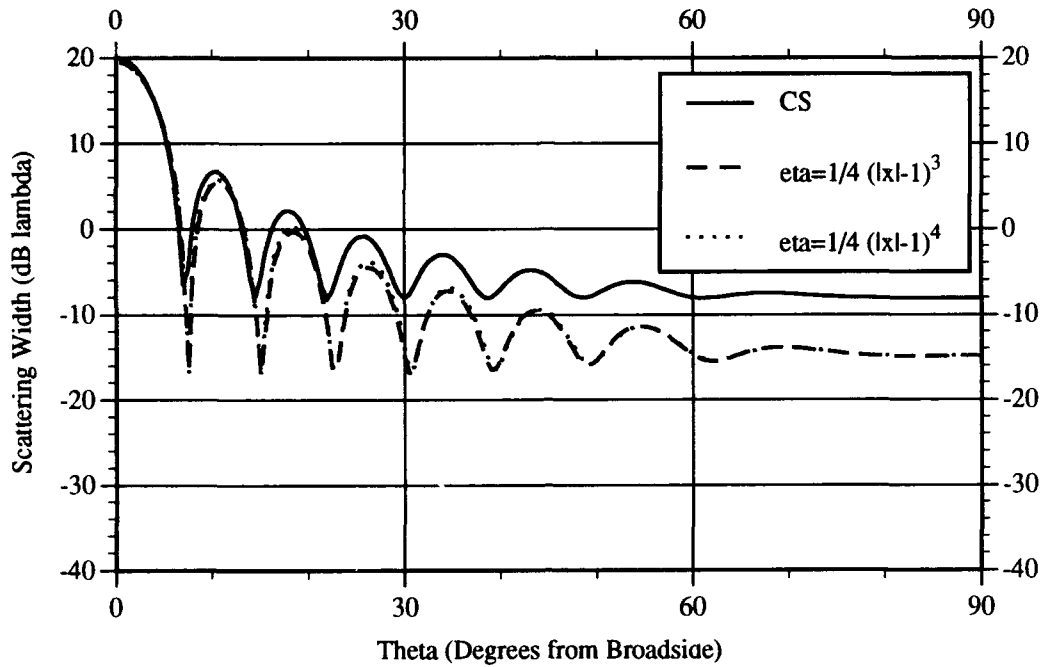


Figure 4.13. Scattering Predictions for  $2\lambda$  Conducting Strips with  $1\lambda$  Tapered Resistive Loads and Conducting Strip Reference,  $\eta = 1/4 (|x| - 1)^3$  and  $1/4 (|x| - 1)^4$

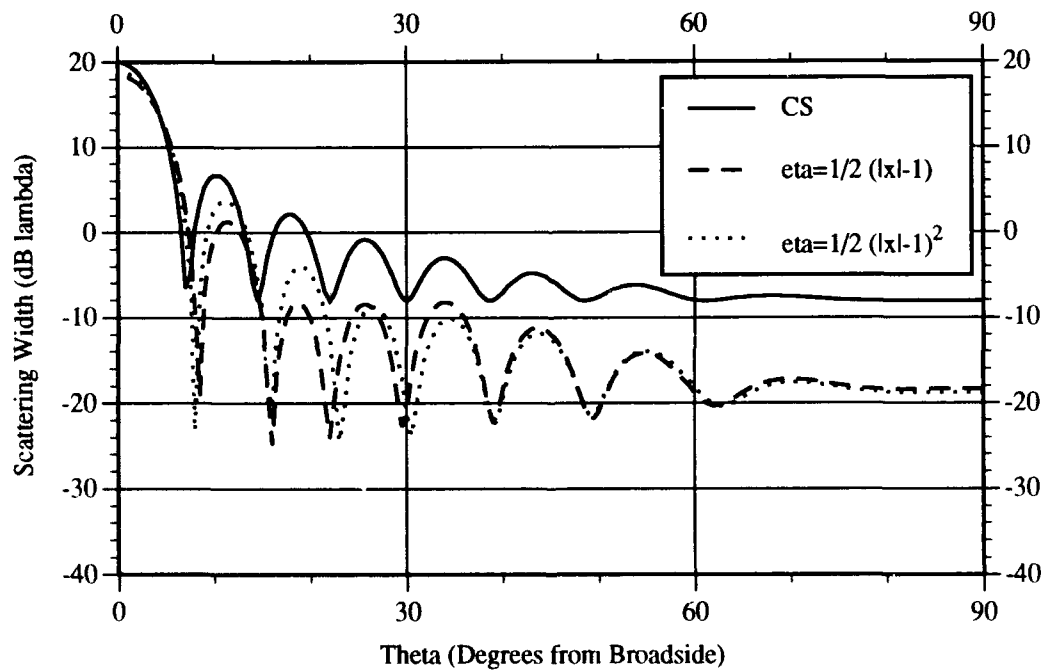


Figure 4.14. Scattering Predictions for  $2\lambda$  Conducting Strips with  $1\lambda$  Tapered Resistive Loads and Conducting Strip Reference,  $\eta = 1/2 (|x| - 1)$  and  $1/2 (|x| - 1)^2$

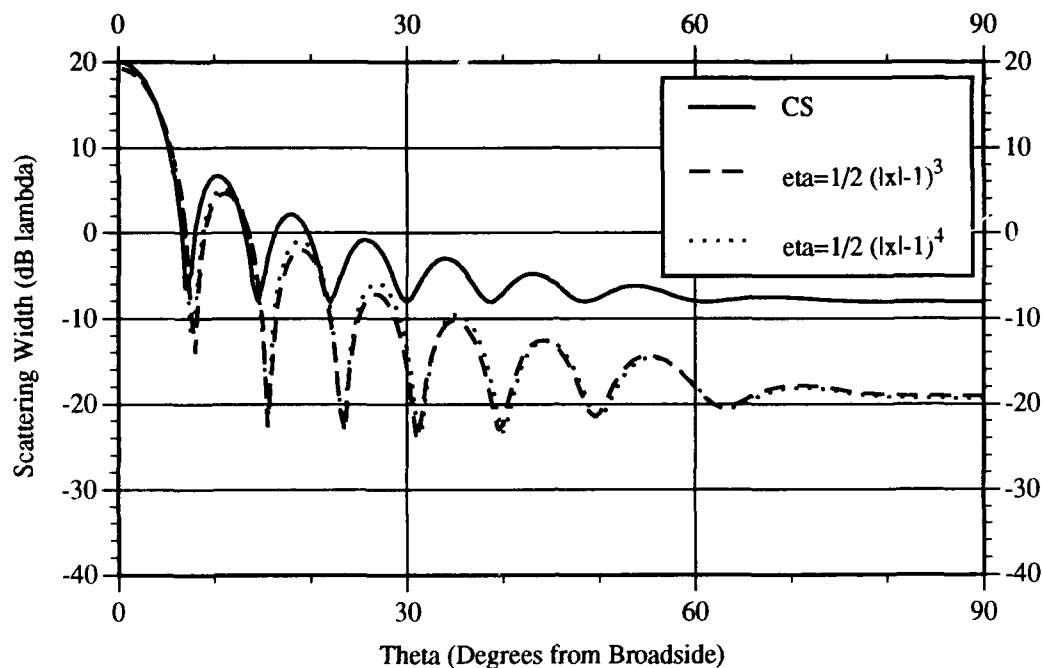


Figure 4.15. Scattering Predictions for  $2\lambda$  Conducting Strips with  $1\lambda$  Tapered Resistive Loads and Conducting Strip Reference,  $\eta = 1/2 (|x| - 1)^3$  and  $1/2 (|x| - 1)^4$

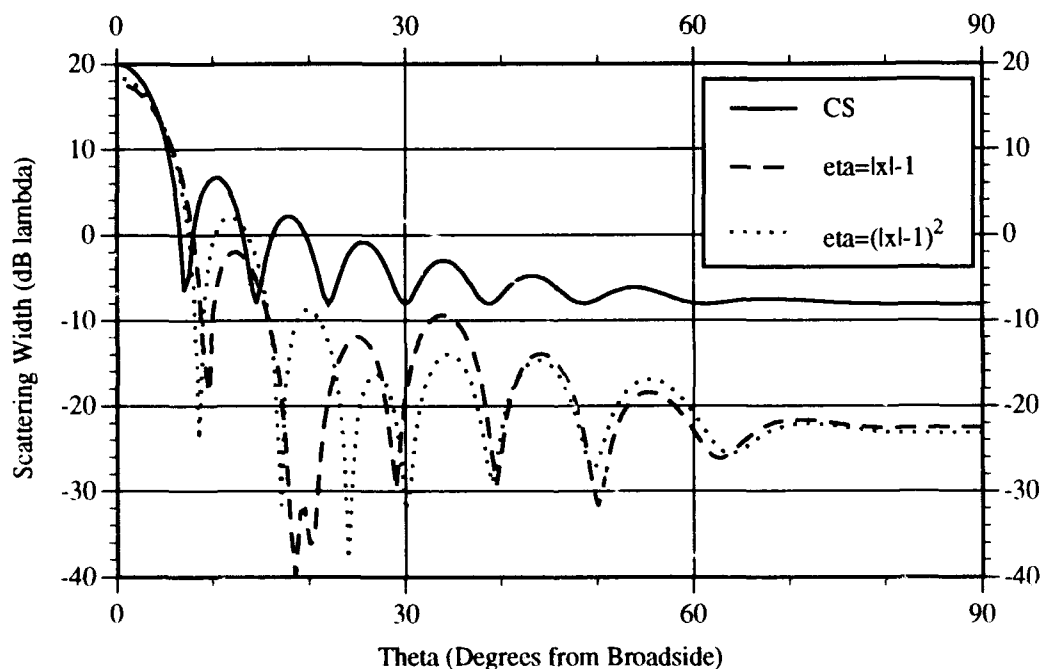


Figure 4.16. Scattering Predictions for  $2\lambda$  Conducting Strips with  $1\lambda$  Tapered Resistive Loads and Conducting Strip Reference,  $\eta = |x| - 1$  and  $(|x| - 1)^2$



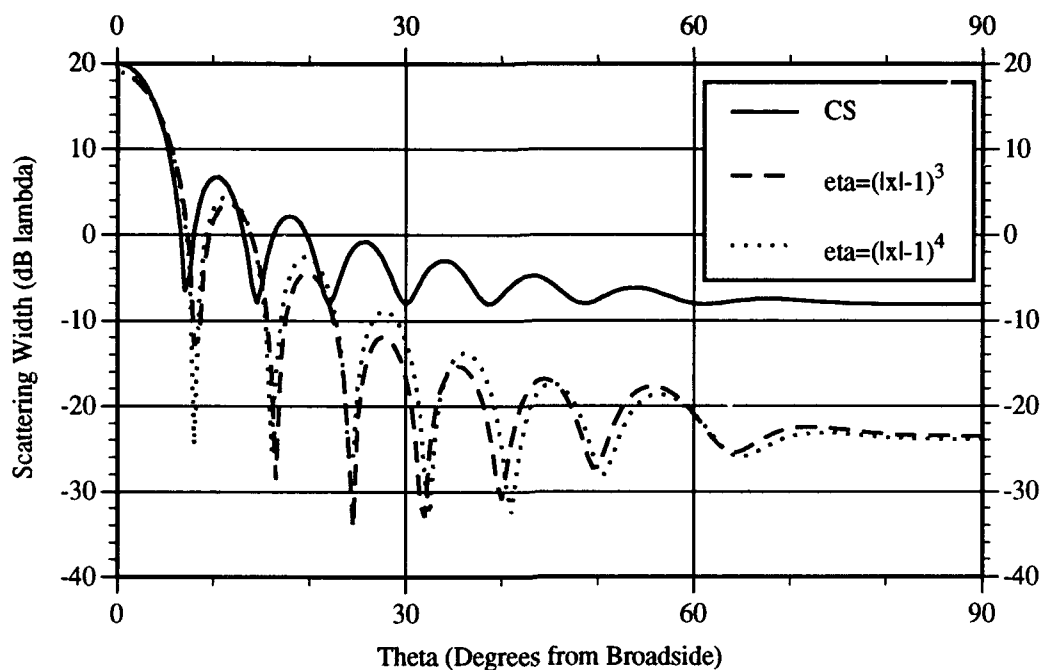


Figure 4.17. Scattering Predictions for  $2\lambda$  Conducting Strips with  $1\lambda$  Tapered Resistive Loads and Conducting Strip Reference,  $\eta = (|x| - 1)^3$  and  $(|x| - 1)^4$

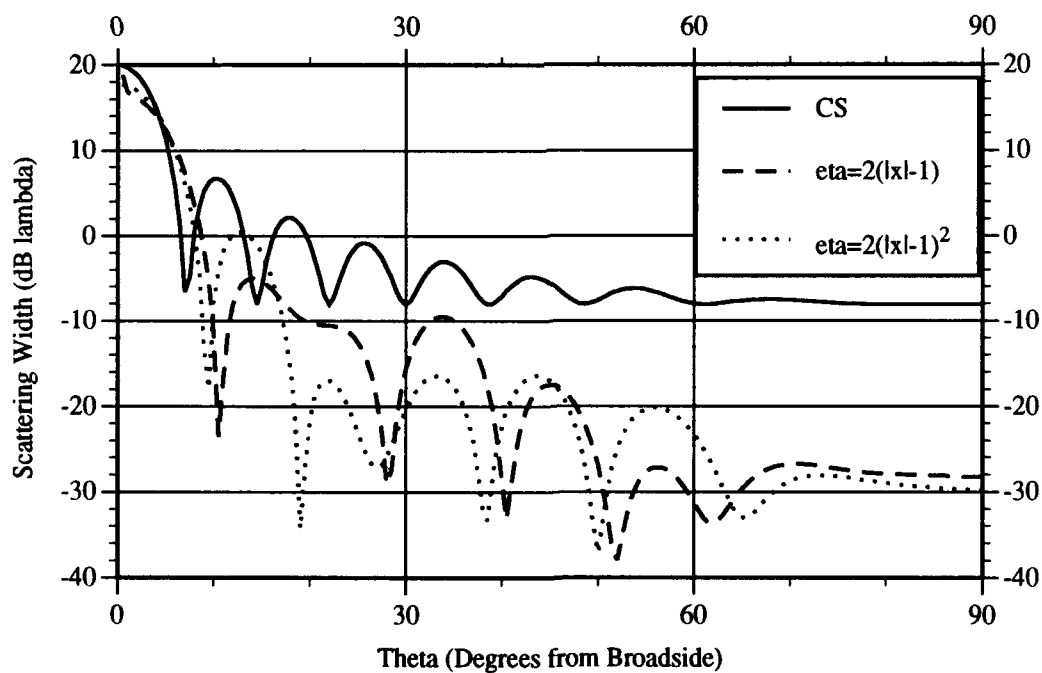


Figure 4.18. Scattering Predictions for  $2\lambda$  Conducting Strips with  $1\lambda$  Tapered Resistive Loads and Conducting Strip Reference,  $\eta = 2(|x| - 1)$  and  $2(|x| - 1)^2$

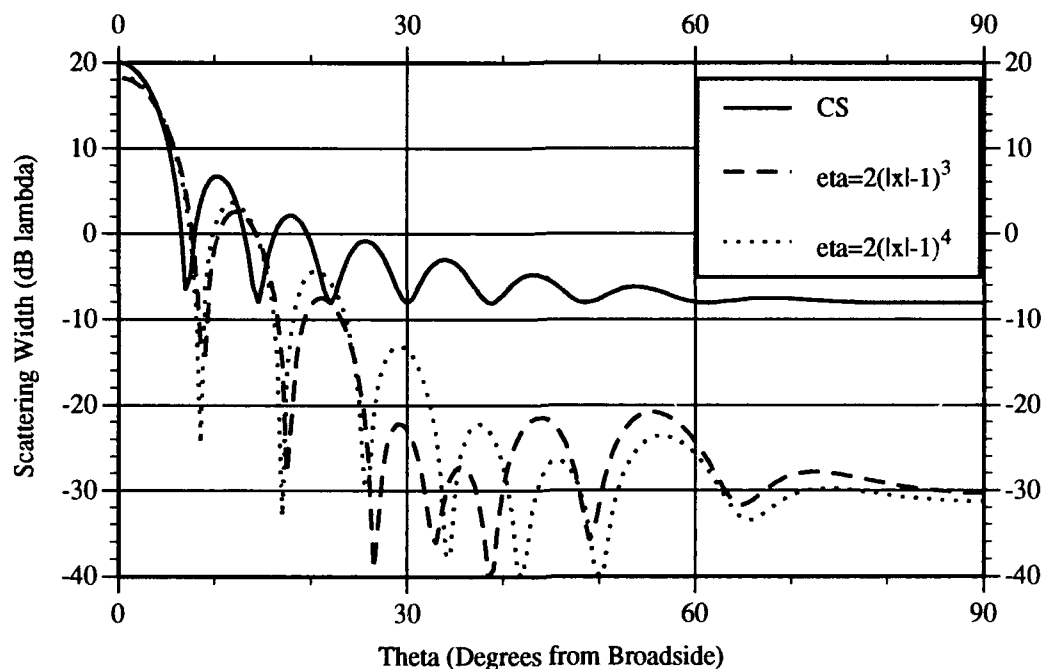


Figure 4.19. Scattering Predictions for  $2\lambda$  Conducting Strips with  $1\lambda$  Tapered Resistive Loads and Conducting Strip Reference,  $\eta = 2(|x| - 1)^3$  and  $2(|x| - 1)^4$

Overall, the tapered resistive-loaded conducting strips affected the level of scattering reduction more than the constant resistive-loaded conducting strips. The constant resistive loads were more effective at just reducing the main lobe's peak. Resistive tapers were especially desirable in reducing sidelobe and edge-on scattering levels. The higher degree tapers had larger decreases in edge-on scattering levels. This did not necessarily mean that the higher degree tapers had the lowest overall sidelobe levels. This will be quantitatively explored further in the next section.

### Tradeoffs

To attempt to quantify these scattering behaviors five figures of merit were defined for the resistive-loaded scattering patterns. These figures of merit were referenced to the  $4\lambda$  conducting strip. The first two figures of merit define what effect the loading has on the main lobe, i.e., the scattering level reduction of the main lobe and the amount of main lobe

broadening. Next, the edge-on scattering levels were referenced to the conducting strip. The last two figures of merit were defined for the sidelobe scattering reductions. Since the sidelobes for the tapered resistive-loaded conducting strips had the same general shape as the conducting strip sidelobes, it was decided to average the peaks of the sidelobes over two sectors. These two sectors were defined to be  $0^\circ$ - $30^\circ$  and  $30^\circ$ - $60^\circ$ . Then, these averages were referenced to the same sectors of a conducting strip. This technique was not applied to the constant resistive-loaded strips because of the broadening that occurs. Also, sidelobe control was already determined to be more effective with the tapered resistive loads. Table 4-1 lists the figures of merit calculated for the predictions presented in the previous section. References for the  $4\lambda$  conducting strip were: 19.9 dB main lobe, -8.1 dB edge-on, 2.7 dB  $0^\circ$ - $30^\circ$  sidelobe average, and -8 dB  $30^\circ$ - $60^\circ$  sidelobe average.

TABLE 4.1  
FIGURES OF MERIT FOR RESISTIVE-LOADED CONDUCTING STRIPS

RESISTIVE LOAD	MAIN LOBE REDUCTION (dB)	MAIN LOBE BROADENING (degrees)	EDGE-ON REDUCTION (dB)	SIDELOBE REDUCTION $0^\circ$ - $30^\circ$ (dB)	SIDELOBE REDUCTION $30^\circ$ - $60^\circ$ (dB)
$\eta=0.5$	2.5	2.5	8.7	N/A	N/A
$\eta=1.5$	4.1	7.5	5.0	N/A	N/A
$\eta=2$	4.4	7.5	3.9	N/A	N/A
$\eta=4$	5.0	7.5	2.2	N/A	N/A
$\eta=1/4 ( x -1)$	0.8	1.0	6.6	4.3	4.3
$\eta=1/2 ( x -1)$	1.4	1.5	10.2	7.9	6.5

$\eta= x -1$	2.2	2.5	14.4	9.7	9.2
$\eta=2( x -1)$	3.0	3.5	20.1	10.5	13.3
$\eta=1/4 ( x -1)^2$	0.5	0.5	6.7	3.2	4.6
$\eta=1/2 ( x -1)^2$	1.0	1.0	10.7	5.7	7.3
$\eta=( x -1)^2$	1.5	1.5	15.1	10.3	10.5
$\eta=2( x -1)^2$	2.2	2.5	21.7	11.0	12.9
$\eta=1/4 ( x -1)^3$	0.4	0.5	6.8	2.5	4.7
$\eta=1/2 ( x -1)^3$	0.7	1.0	11.0	4.2	7.6
$\eta=( x -1)^3$	1.2	1.0	15.4	6.9	11.9
$\eta=2( x -1)^3$	1.7	2.0	22.2	11.7	18.4
$\eta=1/4 ( x -1)^4$	0.3	0.5	6.8	1.9	4.5
$\eta=1/2 ( x -1)^4$	0.6	0.5	11.3	3.2	7.5
$\eta=( x -1)^4$	0.9	1.0	15.8	5.0	11.9
$\eta=2( x -1)^4$	1.4	1.5	23.2	7.3	19.4

What's immediately apparent from Table 4.1 is that the constant loads reduce the main lobe's peak more than the tapered loads. However, this is at the expense of the width of the main lobe. As  $\eta$  increases the width of the main lobe increases also. This is not a desirable response for a scattering reduction design; however, if broadside incidence is avoided reduced sidelobes and edge-on scattering levels become more important. The

tapered loads provide this type of response. Figures 4.20 through 4.24 present the figures of merit in a more visual manner. The constant  $a$  is varied from 0.25 to 2 for values of  $b$  from 1 to 4. As Figure 4.20 shows, the  $2(|x|-1)$  resistive taper causes the most reduction of the main lobe's peak. Again, as in the constant resistive-loaded case, this broadens the main lobe more than the other tapers as shown in Figure 4.21. The  $a(|x|-1)^4$  resistive taper has the overall least broadening as compared to the other degrees of polynomial. Also, Figure 4.22 indicates that the  $2(|x|-1)^4$  taper has the best edge-on scattering reduction. This doesn't necessarily make this taper the best choice for scattering reduction. Figures 4.23 and 4.24 display the changes in sidelobe comparison described earlier. Even though the  $2(|x|-1)^4$  taper is the best choice when considering the sidelobe reduction from  $30^\circ$ - $60^\circ$ , it has the least amount of sidelobe reduction in the  $0^\circ$ - $30^\circ$  sector. Obviously, design constraints must be defined before the optimum taper is selected. The amount and location of scattering reduction ultimately define the optimum taper.

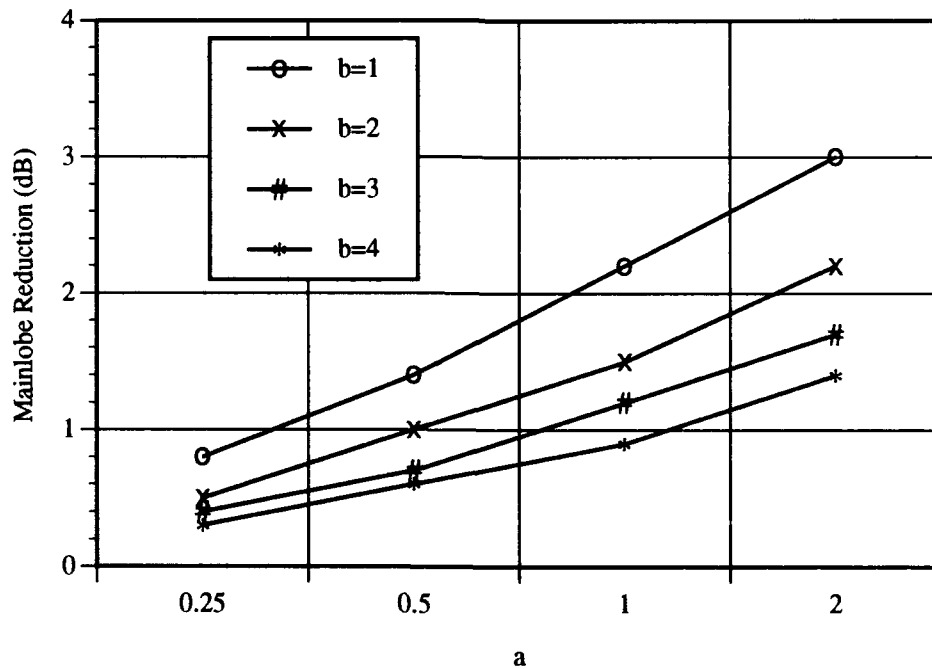


Figure 4.20. Main Lobe Scattering Reduction for  $a(|x|-1)^b$  Taper

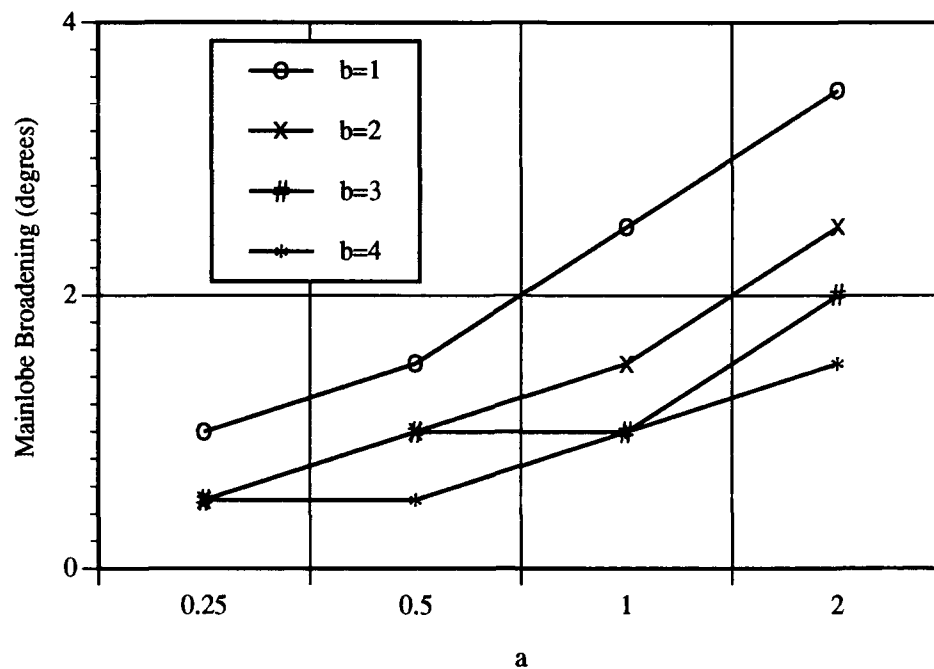


Figure 4.21. Main Lobe Broadening for  $a(|x|-1)^b$  Taper

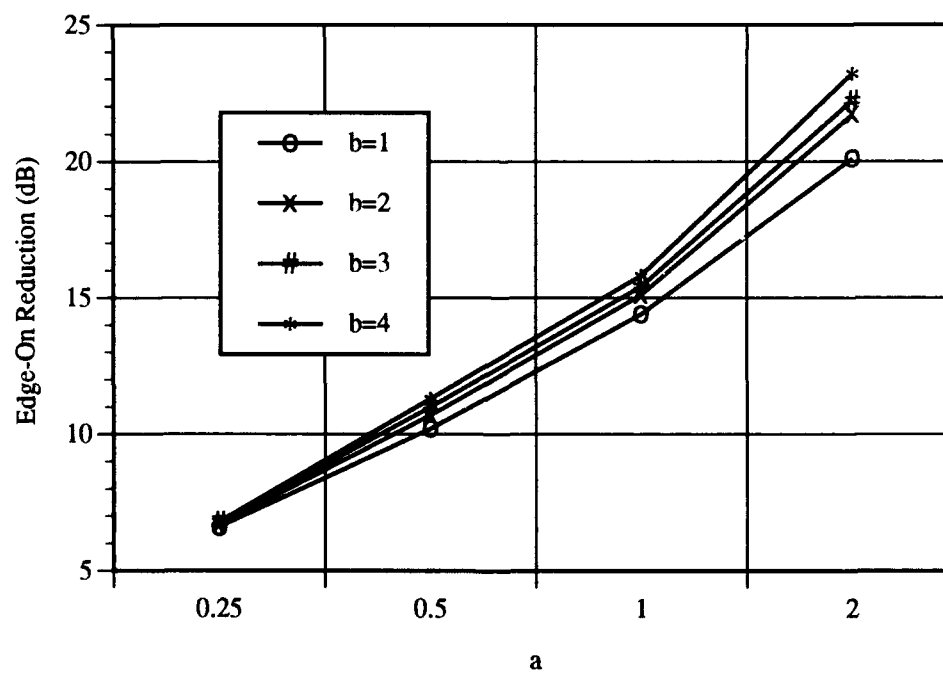


Figure 4.22. Edge-On Reduction for  $a(|x|-1)^b$  Taper

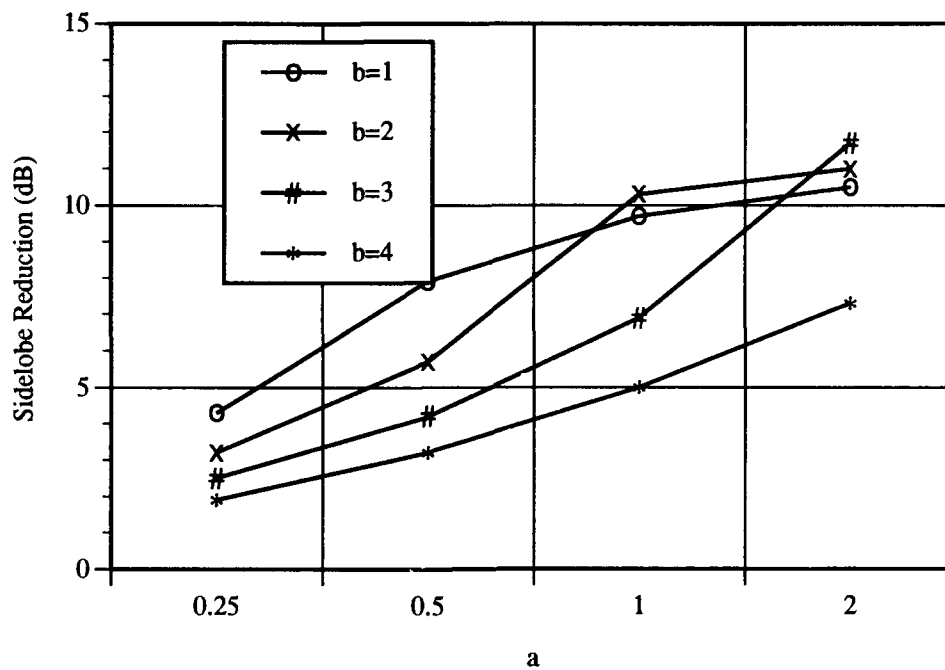


Figure 4.23. Sidelobe Reduction for  $a(|x|-1)^b$  Taper,  $0^\circ$ - $30^\circ$

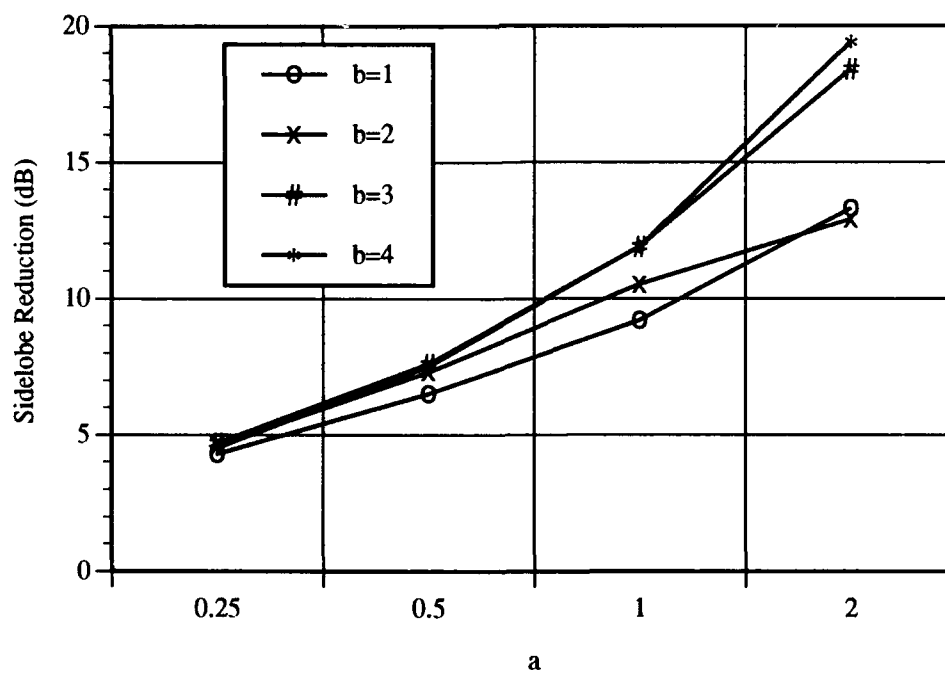


Figure 4.24. Sidelobe Reduction for  $a(|x|-1)^b$  Taper,  $30^\circ$ - $60^\circ$

## V. Conclusions

### Summary and Findings

This thesis investigated electromagnetic scattering from resistive strips and resistive-loaded conducting strips using a rigorous UTD formulation. The UTD diffraction coefficients were derived in (7) using Wiener-Hopf techniques and Jones' Method. Multiple diffractions were incorporated into the formulation using MSRM. Multiple diffractions included double and triple diffractions between adjacent junctions and double and triple diffractions between strip ends and non-adjacent junctions.

Computer code that incorporated these diffractions was developed in (10) for resistive strips attached to a PEC half-plane. This code was modified for the symmetrical strip geometry investigated in this thesis. Scattering predictions were performed for constant resistive strips, constant resistive-loaded conducting strips, tapered resistive strips, and tapered resistive-loaded conducting strips. Predictions were compared to MM and measurements to determine the validity of the UTD formulation.

For UTD predictions with  $TM_z$  polarization, no appreciable deviation from MM existed for a conducting strip, constant resistive strips, and constant resistive-loaded conducting strips.  $TE_z$  polarization showed excellent comparisons for a conducting strip and constant resistive strips. For constant resistive-loaded conducting strips,  $TE_z$  polarization exhibited deviation from the MM solution towards edge-on by rising a few dB and then dropping to zero when the MM solution went smoothly to zero. For both tapered resistive strips and tapered resistive-loaded conducting strips, UTD predictions for  $TM_z$  polarization compared well to MM until close to edge-on. Then, depending on the severity of the taper, edge-on differences between the scattering predictions increased. This was more apparent for the tapered resistive strips.  $TE_z$  polarization introduced the same rise at edge-on when MM went to zero for both the tapered resistive strips and the tapered



resistive-loaded conducting strips. Generally, the scattering predictions for  $TM_z$  polarization compared better than the predictions for  $TE_z$  polarization.

The comparisons between the UTD predictions and measurements for conducting strips and constant resistive strips ranged from good to excellent for both polarizations. For constant resistive-loaded conducting strips the comparisons ranged from fair to good. Generally, for constant resistive-loaded conducting strips, the  $TM_z$  polarization showed better agreement than the  $TE_z$  polarization, especially at edge-on incidence. For tapered resistive strips and tapered resistive-loaded conducting strips, the agreement to measurements ranged from fair to good. Again,  $TM_z$  polarization showed better agreement.

Limitations in the UTD predictions were explored for tapered resistive strips and tapered resistive-loaded conducting strips based on edge-on  $TM_z$  scattering level comparisons with MM. It was discovered that resistive tapers had more of a tendency for edge-on scattering deviation as compared to tapered resistive-loaded conducting strips. This was because both strip geometries were the same length; thus, the tapered resistive strip had more and larger discontinuities between discrete strips than the loaded strip.

From these limitations it was decided to explore the scattering characteristics of  $TM_z$  polarization for constant resistive-loaded conducting strips and tapered resistive-loaded conducting strips. Constant resistive-loaded conducting strips affected the main lobe's scattering level more; but, suffered from main lobe broadening. Tapered loads resulted in smaller broadening of the main lobe and significant reduction of sidelobe and edge-on scattering levels. It was discovered that extreme tapers, i.e.,  $\eta = 2(|x| - 1)^4$ , had better reductions in edge-on scattering and sidelobe scattering from  $30^\circ$ - $60^\circ$ . Less extreme tapers, such as  $\eta = 2(|x| - 1)$ ,  $2(|x| - 1)^2$ , and,  $2(|x| - 1)^3$ , had better reductions in sidelobe scattering from  $0^\circ$ - $30^\circ$ . Design constraints would be needed to select the optimum taper.

### Recommendations

Considering the deviations from MM for several cases of edge-on incidence, the rigorous UTD formulation could be modified to include more multiple diffractions. This would improve the edge-on predictions for  $TE_z$  polarization with tapered and loaded geometries. Also, the edge-on predictions for  $TM_z$  polarization with more extreme tapers would improve.

Another area to extend the research in this area would be to develop an optimization routine for synthesis of discrete resistive loads for a symmetrical strip geometry. The scattered field would be minimized at the desired points on a frequency response; then, after setting the number of discrete strips desired, the optimization routine would synthesize the required resistance values. Research has already been accomplished in this area for discrete resistive loads attached to a PEC half-plane.

Last, the rigorous UTD formulation could be extended to a more complicated geometry. A starting geometry might be a curved strip with a goal of modelling a parabolic antenna. Resistive loading could be used to modify the antenna's scattering pattern.

### Bibliography

1. Balanis, Constantine A. Advanced Engineering Electromagnetics. New York: John Wiley & Sons, 1989.
2. Haupt, Randy L. and Valdis V. Liepa. Synthesis of Resistive Tapers to Control Scattering Patterns of Strips. PhD thesis. University of Michigan, Ann Arbor MI, 1988.
3. Heaton, Capt Mark C. Electromagnetic Scattering from Impedance Strips and Impedance-Loaded Conducting Strips. MS thesis, AFIT/GE/ENG/90D-26. School of Engineering, Air Force Institute of Technology (AU), Wright-Patterson AFB OH, December 1990 (AD-A230526).
4. Jones, D.S. "A Simplifying Technique in the Solution of a Class of Diffraction Problems," Quarterly Journal of Mathematics, III: 189-196 (1952).
5. Knott, Eugene F. and others. Radar Cross Section. Norwood MA: Artech House, 1985.
6. Kouyoumjian, Robert G. and Prabhakar H. Pathak. "A Uniform Geometrical Theory of Diffraction for an Edge in a Perfectly Conducting Surface," Proceedings of the IEEE, 62: 1448-1461 (November 1974).
7. Ly, Hung C. A UTD Analysis of the Diffraction by Planar Two and Three Part Configurations Consisting of Thin Dielectric/Ferrite Materials. MS thesis. Ohio State University, Columbus OH, 1989.
8. Noble, B. Methods Based on the Wiener-Hopf Technique. New York: Pergamon Press, 1958.
9. Rojas, Roberto G. "Wiener-Hopf Analysis of the EM Diffraction by an Impedance Discontinuity in a Planar Surface and by an Impedance Half-Plane," IEEE Transactions on Antennas and Propagation, 36: 71-83 (January 1988).
10. Rojas, Roberto G. and Michael F. Otero. Synthesis of the Frequency Response of an Inhomogeneous Resistive Strip. Grant NSG 1613. Columbus OH: ElectroScience Laboratory, Ohio State University, August 1990.
11. Tiberio, R. and Robert G. Kouyoumjian. "A Uniform GTD Solution for the Diffraction by Strips Illuminated at Grazing Incidence," Radio Science, 14: 933-941 (November-December 1979).
12. Weinstein, Lev A. The Theory of Diffraction and the Factorization Method. Colorado: The Golem Press, 1969.